THE NATURE OF SUPERNOVAE PROGENITORS AND INTERSTELLAR DUST: LIGHT ECHOES AROUND TYPE IA SUPERNOVE

A Dissertation

by

YI YANG

Submitted to the Office of Graduate and Professional Studies of
Texas A&M University
in partial fulfillment of the requirements for the degree of

DOCTOR OF PHILOSOPHY

Chair of Committee,	Lifan Wang
Committee Members,	Kevin Krisciunas
	James Long
	Nicholas Suntzeff
Head of Department,	Peter McIntyre

August 2017

Major Subject: Physics

ABSTRACT

Incomprehensive knowledge on dust is hindering our study of the universe. For example, the type Ia supernovae (SNe) cosmology requires better estimation of interstellar extinction to reduce systematic uncertainties. The extinction properties measured towards type Ia SNe suggest the properties of extragalactic dust may be incompatible with the Galactic dust, resulting in a systematic uncertainty in the intrinsic luminosity and distances to the type Ia SNe. Additionally, the exact progenitor systems of type Ia SNe and explosions remain unknown.

We present the results of our multi-band polarimetric monitoring of SN 2014J at five epochs between 277 days and 983 days after the B-band maximum light. The polarization measured at day 277 shows conspicuous deviations from other epochs and this can be identified as due to at least $\sim 10^{-6} M_\odot$ of dust located at a distance of $\sim 5\times10^{17}$ cm away from the SN. The presence of this circumstellar dust may set strong constraints on the progenitor system that led to the explosion of SN 2014J. We also detected different wavelength-dependencies of scattering in different ISM components through the resolved interstellar light echoes around SN 2014J. We found a steeper extinction law in a dense dust layer and a Milky Way-like extinction law in a diffuse cloud. This reveals the extinction law fluctuation of the extragalactic dust on parsec scales, and we consider systematically steeper extinction laws towards type Ia SNe do not have to represent the average behavior of the extinction law in the host galaxy. We also preformed high-precision photometry with *HST* for SN 2014J from 277 days to 985 days past the $B-$band maximum light. We found the reprocessing of electrons and X-rays emitted by the radioactive decay chain ^{57}Co$\rightarrow^{57}$Fe are needed to explain the significant flattening of both the $F606W$-band and the pseudo-bolometric light curves. The flattening confirms previous predictions that

the late-time evolution of type Ia supernova luminosities requires additional energy imput from the decay of ^{57}Co (Seitenzahl et al., 2009).

Antarctic sites appear to be excellent sites for optical, NIR, and THz astronomical observations. To understand and make the use of the long ‘winter night’ as well as other remarkable observation conditions is one of the essential topics for future astronomy. Related to my PhD thesis, taking advantages of the long “winter night” as well as characterizing other remarkable observation conditions are specifically important to carry out future SN and other time-domain surveys at Dome A. We present here the measurements of sky brightness with the Gattini ultra-large field of view ($90^\circ \times 90^\circ$) in the photometric B-, V-, and R-bands, cloud cover statistics measured during the 2009 winter season, and an estimate of the sky transparency. These values were obtained around the year 2009 with minimum aurora, and they are comparable to the faintest sky brightness at Mauna Kea and the best sites of northern Chile.

ACKNOWLEDGMENTS

Foremost, I would like to extend my sincere gratitude to my wonderful graduate advisor, Lifan Wang, for establishing fantastic projects with the Hubble Space Telescope (*HST*) for me to start working on, for teaching me innumerous invaluable lessons, and for providing guidance, support, and resources to my research and life. I also want to express my sincere appreciation to my mentors, Dietrich Baade and J. Craig Wheeler for their tremendous and continuous support on my research and life.

I would like to give a big thank-you to Peter J. Brown for providing me generous help on aspects of science, technical details, and stress relexing. He is the person who was always willing to read my very first drafts. I also want to thank the other members in my conmmittee, Kevin Krisciunas, James Long, and Nicholas Suntzeff for their insightful guidance on each discussions and every weekly group meetings we had throughout my life as a graduate student. Special thanks to Anna Moore for supervising me on the Antarctica site-testing projects and hosting me for two summers to work at Caltech. Thanks to Kevin Krisciunas for spending months to revise my first draft of the Gattini Antarctica site-testing paper.

I thank George P.Mitchell and the Mitchell family for starting a world-class physics and astronomy department. I thank Lifan Wang, Dietrich Baade, Peter J. Brown, Nicholas Suntzeff, and J. Craig Wheeler for being my referees throughout my postdoc application process. I acknowledge all my collaborators throughout my graduate school as well as our Explosion PolarIzation Collaboration (EPIC) for their generous support and insightful discussions, speciall thanks to Lifan Wang, Dietrich Baade, Peter. J. Brown, Aleksandar Cikota, Misty Cracraft, Peter A. Höflich, Justyn Maund, Ferdinando Patat, William B.

Sparks, Jason Spyromilio, Heloise F. Stevance, Xiaofeng Wang, and J. Craig Wheeler for being my co-authors in my SN 2014J papers.

I would like to thank Xiaofeng Wang and the Tsinghua Center for Astrophysics for the very kind hosting when I was working in China. I thank my undergraduate advisors and mentors, Jianning Fu, Yanping Zhang, and Xiaojun Jiang for their help and patience during the first years of my astronomy career. I would also thank all the graduate students at the Mitchell Institute, Texas A&M University for their friendship and help. Special thanks to our Aggienova graduate student Michael T. Smitka and Andrew Quick for their help and staying with me during our group meetings. Thanks to Ting Li and Wei Zhao for their valuable advice on my career.

Finally, I would like to express my deepest gratitude to my family – my mom and dad for bringing me to the world, for raising me up, and for supporting my decision to pursue a Ph.D on the other side of the earth.

CONTRIBUTORS AND FUNDING SOURCES

Contributors

This work was supported by a dissertation committee consisting of Professor Lifan Wang, Nicholas Suntzeff, Kevin Krisciunas of the George P. and Cynthia Woods Mitchell Institute for Fundamental Physics & Astronomy, Texas A. & M. University, Department of Physics and Astronomy, and Professor James Long of the Department of Statistics.

The spectropolarimetry and imaging polarimetry data analyzed for Chapter 3 was provided by Dr Kouji Kawabata of the Hiroshima Astrophysical Science Center, Hiroshima University and Dr. Ferdinando Patat of the European Southern Observatory, respectively. Some of the data in Chapter 2, Chapter 3, and Chapter 4 used in this dissertation were obtained from the Mikulski Archive for Space Telescopes (MAST). All other work conducted for the dissertation was completed by the student independently. Published content and contributions including:

1. Yang, Y. et al. (2016). “Optical Sky Brightness and Transparency During the Winter Season at Dome A Antarctica From the Gattini-Allsky Camera”. In: 2016arXiv161010094Y.
Y.Y. reduced the Gattini data, performed the data analysis, and prepared the manuscript.
©AAS. Reproduced with permission

2. Yang, Y. et al. (2017). “Interstellar-medium Mapping in M82 through Light Echoes around Supernova 2014J”. In: The Astrophysical Journal, Volume 834, Issue 1, article id. 60, 15 pp.
Y.Y. participated in the designation of observation, reduced the *HST* data, performed the data analysis, and prepared the manuscript.

3. Yang, Y. et al. (2017). “Late-time flattening of Type Ia Supernova light curves: Constraints from SN 2014J in M82”. In: 2017arXiv170401431Y.

Y.Y. participated in the designation of observation, reduced the *HST* data, performed the data analysis, and prepared the manuscript.

Funding Sources

The supernova research by Y. Yang, is supported by NSF grant AST-0708873. Y. Yang also acknowledge support from NASA/STScI through grant HST-GO-13717.001-A, grant HST-GO-13717.001-A, HST-GO-14139.001-A, and HST-GO-14663.001-A. The study was also supported by the Strategic Priority Research Program at The Emergence of Cosmo-logical Structures of the Chinese Academy of Sciences, Grant No. XDB09000000. The Antarctica site-testing project was funded by the following awards from the National Science Foundation Office of Polar Programs: ANT 0836571, ANT 0909664 and ANT 1043282.

NOMENCLATURE

ACS	Advanced Camera for Surveys
CSM	Circumstellar Matter
HST	Hubble Space Telescope
ISM	Interstellar Medium
mag	Apparent Magnitude
SED	Spectral Energy Distribution
SN	Supernova
SNe	Supernovae (plural)
WFC	Wide Field Channel
WFC3	Wide Field Camera 3 (WFC3)
WFC3/UVIS	Wide Field Camera 3 Ultraviolet-Visible Channel
z	Redshift

TABLE OF CONTENTS

LIST OF FIGURES

FIGURE Page

LIST OF TABLES

TABLE Page

1. INTRODUCTION

Studying cosmic dust has important consequence on understanding a wide range of astronomical process, i.e., ranging from star formation to galaxy evolution. Probably the most direct effect of dust is the extinction. Incomprehensive knowledge on dust is hindering our study of the universe. For example, The Type Ia supernova (SN) cosmology, which uses Type Ia SNe as the most accurate distance indicators. It has been widely agreed that the explosion of luminous hydrogen-poor Type Ia SNe are driven by the thermonuclear runaway of ($\geqslant 1M_{\odot}$) carbon/oxygen white dwarfs (WDs Hoyle & Fowler, 1960) About $\sim$0.1-1.0$M_{\odot}$ amount of radioactive ^{56}Ni fused during the accretion-induced explosion, and the luminousity evolution can be explained by the combination of radioactive decay channels, together with the time-evolution of ejecta opacity. Type Ia SNe cosmology, which uses these ‘standard candels’ as the most accurate distance indicators at redshifts out to z $\sim$2 (Riess et al., 1998; Perlmutter et al., 1999; Riess et al., 2016). Amazingly, this accuracy is achieved without knowing exactly the nature of various progenitors.

Study the progenitor system and probe the optical properties of dust in nearby extragalactic environments are both important to reduce systematic uncertainties. The characterization of dust in the diffuse ISM relies heavily on the observed wavelength dependencies of extinction and polarization (Patat et al., 2015; Voshchinnikov et al., 2012). The observed wavelength dependence of interstellar extinction R_V contains information on both the size and composition of the grains. The value of $R_V = 3.1$ (Cardelli et al., 1989) has been often considered the Galactic standard, but with a range from 2.2 to 5.8 (Fitzpatrick, 1999) for different lines of sight. There is increasing evidence that extinction curves towards Type Ia SNe systematically favor a steeper law (R_V <3, see Nobili & Goobar, 2008; Cikota et al., 2016). This discrepancy has remained unexplained. These steeper extinction laws derived from the extragalactic environments resulting in a systematic uncertainty in the intrinsic luminosity and distances to the Type Ia SNe. Additionally, the exact progenitor systems of Type Ia SNe and explosions remain unknown. Comprehensive understanding of (1) the extinction and optical properties of the extragalactic dust grains, and (2) the mechanism and the progenitor for Type Ia SN explosions, are both essential.

1.1 Interstellar Light Echoes

Light echoes are from scattered light of a transient event arise from dust clouds. They are known as ‘astronomical time machines’ by preserving the information of the original explosion. (Rest et al., 2008; Davidson & Humphreys, 2012; Rest et al., 2012). However, they also reveal the optical properties of the scattering dust since photons scattered by the dust reach the observer in a slightly different path. Considering the transient event as a radiation flash, photons that directly traverse the dust lane reach the observer first, while other photons travel a slightly different path and are scattered back to reach the observer later. The extra path length of the two-segment trajectory results in significant time-delay and hence produces light echoes. The trajectories followed by the scattered photons are confined in an ellipsoid. This iso-delay ellipsoid expands over time, mapping out the dust traversed, and preserves the explosion information.

Such events have already provided substantial and exciting scientific opportunities. Examples are probing the progenitor properties of historical transients (Rest et al., 2008; Davidson & Humphreys, 2012) and in some cases the three-dimensional structure of the explosion, see the examples of η Carinae (Rest et al., 2012), SN 1987A (Sinnott et al., 2013) and Cassiopeia A (Grefenstette et al., 2014). Additionally, polarized light echoes provide a unique opportunity to derive an independent geometric distance, i.e., as for the galactic star V838 Monocerotis (Sparks et al., 2008).

Interstellar extinction caused by dust affects most astronomical observations. Currently a widely-used approach in determining the extinction is the ‘pair method’ - comparing spectrophotometry of two sources with the same spectral energy distribution, one of which has negligible foreground extinction. However, information acquired through this pair method is limited to single sightlines. The scattering nature of the extragalactic dust grains is poorly understood. Resolved light echoes provide additional information on interstellar dust extinction because they literally reflect light-scattering properties and reach the observer through multiple different paths. Therefore, observations of the SN and resolved light echoes provide a unique opportunity to measure the extinction properties of the dust along the line of sight and the scattering properties independently. This opportunity, however, can be raredly offered by a second, nearby object of suitable brightness.

1.2 Dust Around Type Ia Supernovae

The mass-loss history of the type Ia SNe progenitor before the final explosion can be revealed by the scattered light from ejecta close to the SN. No direct evidence of circumstellar dust has ever been found previously around type Ia SNe, although several authors have proposed that circumstellar dust scattering may be a solution to the surprisingly low R_V values towards type Ia SNe (Wang, 2005; Patat et al., 2006; Goobar, 2008). For example, recent observations of the highly reddened SN 2014J in M82 have found no convincing evidence of the presence of circumstellar dust (Patat et al., 2015; Brown et al., 2015; Johansson et al., 2017; see, however, Foley et al., 2014; Hoang, 2017). The detection of CSM is of critical importance for understanding the progenitor systems of type Ia SNe and for the extinction correction of type Ia SNe used as standard candles.

Observations of the polarized scattered light and its time evolution can be an effective way of studying the CSM. Type Ia SNe are intrinsically very little polarized in broad-band observations ($\lesssim 0.2\%$, Wang & Wheeler, 2008), but the scattered light from CSM can be highly polarized. As a SN fades, the portion of the scattered light coming from CSM increases and can contribute significantly to the total flux observed from the SN. Light scattered at large angles can be polarized at $\sim 50\%$. For a spatially unresolved source, the scattered light can contribute significantly to the total integrated light. When the geometric distribution of the dust particles is asymmetric, the integrated polarization can be large and can evolve rapidly with time and the polarization of the integrated light can evolve rapidly with time after the supernova evolves past optical maximum (Wang & Wheeler, 1996).

1.3 Late-time Light Curves of Type Ia SN to Constrain the Progenitor System

Different effects of nucleosynthesis can be testable through the late photometric evolution of Type Ia SNe and may be used to discriminate between different explosion models. Two of the most favorable explosion channels: a delayed detonation in a Chandrasekhar-mass white dwarf (Khokhlov, 1991) and a violent merger of two carbon-oxygen white dwarfs (Pakmor et al., 2011, 2012), will result in late-time light curves behaving differently due to different amounts of ejecta heating from ^{57}Co and ^{55}Fe (Röpke et al., 2012).

At around two year after the maximum light, the radioactive decay chain which dominates the SN light curve at earlier phase: $^{56}\text{Ni}\rightarrow^{56}\text{Co}\rightarrow^{56}\text{Fe}$, is no longer be able to solely explain the light curve flattening (Graur et al., 2016; Shappee et al., 2016; Dimitriadis et al., 2017). Additional radioactive decay channels, i.e., $^{57}\text{Co}\rightarrow^{57}\text{Fe}$ and $^{55}\text{Fe}\rightarrow^{55}\text{Mn}$ are required (Seitenzahl et al., 2014). Different theoretical models predict different amount of isotopes produced during the explosion process (i.e., Röpke et al., 2012; Seitenzahl et al., 2013). Therefore, fitting the decline rate of the light curve at late times provides a unique opportunity to determine the mass of these other nuclides, distinguish between different explosion mechanisms, and in turn, test the enigmatic progenitor scenarios of Type Ia SNe. Therefore, the nearby Type Ia SNe offers a rare opportunity to study the physics of thermonuclear SNe with high-precision photometry at extremely late phases ($\gtrsim$ 800 days).

1.4 Antarctic Site Testing As Pathfinders For Further Astronomical Studies

Antarctic sites appear to be excellent sites for optical, NIR, and THz astronomical observations. To understanding and make the use of the long ‘winter night’ as well as other remarkable observation conditions is one of the essential topics for future astronomy. Taking the advantages of the long ‘winter night’ as well as characterizing other remarkable observation conditions are specifically important to carry out future SN and other time-domain surveys at Dome A.

1.5 Outline of the Dissertation

This dissertation is aiming to explore the properties of Type Ia SN progenitors and the dust properties in the host galaxy.

In Section 2, we discribe the interstellar-medium mapping in M82 through resolved interstellar light echoes around SN 2014J. We carry out multiple-epoch measurements of the size and surface brightness of the light echoes from SN 2014J in the nearby starburst galaxy M82. The images reveal the temporal evolution of at least two major light-echo components. The first one exhibits a filled ring structure with position-angle-dependent intensity, and the second echo component appears as an unresolved luminous quarter-circle arc centered on the SN. The wavelength dependence of scattering measured in different dust components suggests that the dust producing the luminous arc favors smaller grain sizes, while that causing the diffuse light echo may have sizes similar to the Milky Way dust. This reveals the total-to-selective extinction R_V fluctuation of the extragalactic dust on parsec scales, and we consider systematically steeper extinction laws towards Type Ia SNe do not have to represent the average behavior of the extinction law in the host galaxy.

In Section 3, we proposes the constraints from a polarized, unresolved light echo on the circumstellar dust around SN 2014J. We tested the circumstellar environment of SN 2014J by monitoring its late-time polarization with the imaging polarimetry mode of the Hubble Space Telescope (*HST*) ACS/WFC. We found the polarization of Type Ia SN 2014J shows conspicuous deviation at day 277 from other epochs (Kawabata et al., 2014; Patat et al., 2015). The observed time-deviation of polarization can result from light scattered by silicate dust ejecta of $10^{-6}M_{\odot}$ located 0.6 light years from the SN. The location of this matter constrains the time history of the mass ejection and is consistent with an episode of nova-like ejection about 160 years before the SN explosion for a typical speed of 1,000 km/sec.

In Section 4, we report the progenitor constrains from the late-time flattening of type Ia SN 2014j light curves. We obtained five epochs of high precision photometry with HST for SN 2014J from 277 days to 985 days past the B-band maximum light. The reprocessing of electrons and X-rays emitted by the radioactive decay chain ^{57}Co→^{57}Fe are needed to explain the significant flattening of both the $F606W$-(broad V) band and the pseudo-bolometric light curves. The flattening confirms previous predictions that the late-time evolution of type Ia SN luminosities requires additional energy imput from the decay of ^{57}Co (Seitenzahl et al., 2009). Astrometric tests based on the multi-epoch *HST* ACS/WFC images reveal no significant circumstellar light echoes in between 0.3 pc and 100 pc (Yang et al., 2017a) from the SN 2014J. We concluded that the high $M(^{57}\mathrm{N}i)/M(^{56}\mathrm{N}i)$ ratio estimated from the late-time luminosity evolution of SN 2014J favors a near-Chandrasekhar mass explosion model: W7 of Iwamoto et al. (1999).

In Section 5, we demonstrates our efforts in Antarctic site-testing for future large-scale astronomical observatories and transient surveys. From continuous monitoring data at the highest point on the Antarctic plateau in a $90^{\circ} \times 90^{\circ}$ Field-of-View with the Gattini-Dome A All-Sky Camera (Moore et al., 2008). We built a data reduction pipeline and measured the BVR sky brightness, the cloud coverage, and estimated the aurorae statistics from 60,000 raw frames. Light curves of ∼2600 stars brighter than 7.5 in V for a consecutive 120 days have also been obtained.

2. INTERSTELLAR-MEDIUM MAPPING IN M82 THROUGH LIGHT ECHOES AROUND SUPERNOVA 2014J

2.1 Introduction

Interstellar extinction caused by dust affects most astronomical observations. Light traversing a certain distribution of interstellar medium (ISM) produces an integrated effect on extinction. Extinction traces the dust grains, but also diminishes the starlight and limits our ability to interpret the local and distant universe. The study of interstellar dust provides insight into the properties of the extinction. Since dust is a strong coolant, it also plays a critical role in controlling galaxy evolution and star formation.

Observations of interstellar extinction require a beacon shining through interstellar material. In the Milky Way, a very large number of sightlines are available for this purpose, while in external galaxies there are few point source beacons bright enough to study the local ISM. Supernovae (SNe) are the best, and often only, choice. Light echoes provide additional information because they literally reflect light-scattering properties and do not reach the observer along exactly the same path. If SNe are nearby, even resolved light echoes may be observable.

The extinction (in magnitudes) at a certain wavelength or bandpass, λ, is often expressed as $A_\lambda = R_\lambda \times E(B-V)$. The 'total-to-selective' extinction $R_V = A_V/E(B-V)$ depends on the properties of the dust along the line of sight and can be derived by comparing the observed $E(\lambda - V)$ with the extinction curves given by Cardelli et al. (1989). The observed wavelength dependence of interstellar extinction contains information on both the size and composition of the grains. The value of $R_V = 3.1$ (Cardelli et al., 1989) has

---

Reprinted with permission from Yang et al. 2017a, ApJ, 834, 60 been often considered the Galactic standard, but with a range from 2.2 to 5.8 (Fitzpatrick, 1999) for different lines of sight. There is increasing evidence that extinction curves towards Type Ia SNe exhibit a steeper wavelength dependence ($R_V < 3$, see Cikota et al., 2016 for a summary on R_V results of earlier studies). Patat et al. (2007) reported the detection of circumstellar material (CSM) in the local environment surrounding the Type Ia supernova SN 2006X in the nearby galaxy M100. Wang (2005), Patat et al. (2006), and Goobar (2008), show that the scattered light from CSM tends to reduce the value of R_λ in the optical. The effect on R_V and the light curve shape, however, also depends on the geometrical configuration and dust-grain properties (Amanullah & Goobar, 2011; Brown et al., 2015). It is of critical importance to understand whether the low R_V values are caused by (1) systematic differences from extragalactic environments, or (2) inhomogeneities in the vicinity of the SN-Earth direct line of sight (DLOS), or (3) modifications by CSM scattering.

The most reliable approach in determining the extinction is the ‘pair method’ — comparing spectrophotometry of two sources with the same spectral energy distribution, one of which has negligible foreground extinction. Extragalactic reddening can be measured by comparing observed Type Ia SNe to a zero-reddening locus (e.g., Riess et al., 1996; Phillips et al., 1999). However, information acquired through this pair method is limited to single sightlines. Photons scattered by dust travel a slightly different path compared to the directly transmitted light. Therefore, scattered photons provide chances to test the scattering properties of the dust in a bi-dimensional space.

2.1.1 Light echoes

Light echoes are from scattered light of a transient event arise from dust clouds. Here we consider the case of a SN and CSM/ISM. Because of the high initial brightness of SNe, searches for late-time off-source flux excesses have been the main approaches to detect light echoes residing close to the SNe, i.e., the slowly fading light curves of SN 1991T (Schmidt et al., 1994; Sparks et al., 1999), SN 1998bu (Cappellaro et al., 2001), and SN 2006X (Wang et al., 2008). Outside the solar system, spatially resolved light echoes have been rare events. The first one reported arose around Nova Persei 1901 (Kapteyn, 1901; Ritchey, 1901), followed by Nova Sagittarii 1936 (Swope, 1940). Echoes were also found from the Galactic Cepheid RS Puppis (Havlen, 1972) and, with *HST* angular sampling, from the eruptive star V838 Monocerotis (Bond et al., 2003). Vogt et al. (2012) reported the detection of an infrared echo near the Galactic supernova remnant Cassiopeia A. Additionally, spectroscopic observations of nearby light echoes provide unique opportunities to probe the progenitor properties of historical transients (Rest et al., 2008; Davidson & Humphreys, 2012) and in some cases the three-dimenisonal structure of the explosion. For instance, an ancient eruption from η Carinae (Rest et al., 2012), asymmetry in the outburst of SN 1987A (Sinnott et al., 2013) and Cassiopeia A (Grefenstette et al., 2014). In recent years, the number of light echoes from extragalactic SNe has grown rapidly, mostly thanks to *HST*. Table 2.1 provides an overview of the events recorded to date, updated from Table 1 of Van Dyk et al. (2015).

Photons from spatially-resolved light echoes travel a slightly different path compared to the DLOS from the SN to Earth. Therefore, observations of a resolved light echo around a nearby SN provide a unique opportunity to measure the extinction properties of the dust along the DLOS and the scattering properties of the echo-producing dust independently and simultaneously. As the SN fades, outer echoes (echoes with larger angular diameter) associated with ISM at large distances to the SN will become less contaminated by its bright light, and any inner echoes associated with ISM at small distances to the SN, and even the CSM, will become detectable. The expansion with time of the light echoes maps out the 3D structure of ISM along and close to the line of sight.

Detailed introductions to the relation between 2-dimensional light echoes and 3-

Table 2.1. Spatially resolved supernova light echoes

SN	Type	Host Galaxy	Distance (Mpc)	References [a]
1987A	II-Peculiar	LMC	0.05	1, 3, 16, 17, 23
1991T	Ia 91T-like	NGC 4527	15.2	11, 12
1993J	IIb	M81	3.6	6, 13
1995E	Ia	NGC 2441	49.6	10
1998bu	Ia	M96	9.9	2
1999ev	II-P	NGC 4274	9.9	7
2002hh	II-P	NGC 6946	5.5	8, 22
2003gd	II-P	M74	9.5	14, 18
2004et	II-P	NGC 6946	5.5	9
2006X	Ia	M100	15.9	21
2007af	Ia	NGC 5584	22.5	5
2008bk	II-P	NGC 7793	3.7	19
2012aw	II-P	M95	10.0	20
2014J	Ia	M82	3.5	4
2016adj	IIb	NGC 5128	3.7	15

[a] (1) Bond et al. (1990), (2) Cappellaro et al. (2001) (3) Crotts (1988) (4) Crotts (2015) (5) Drozdov et al. (2015) (6) Liu et al. (2003a) (7) Maund & Smartt (2005) (8) Meikle et al. (2006) (9) Otsuka et al. (2012) (10) Quinn et al. (2006) (11) Schmidt et al. (1994) (12) Sparks et al. (1999) (13) Sugerman & Crotts (2002) (14) Sugerman (2005) (15) Sugerman & Lawrence (2016) (16) Suntzeff et al. (1988) (17) Spyromilio et al. (1995) (18) Van Dyk et al. (2006) (19) Van Dyk (2013) (20) Van Dyk et al. (2015) (21) Wang et al. (2008) (22) Welch et al. (2007) (23) Xu et al. (1994)

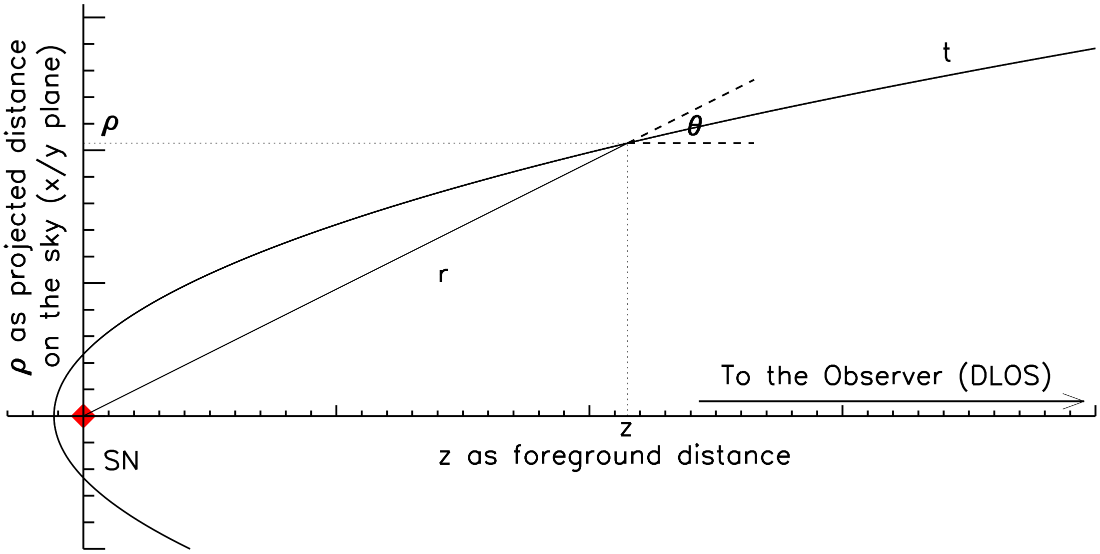

Figure 2.1 Schematic diagram identifying the geometrical parameters used in this paper. The paraboloid represents the iso-delay light surface at some arbitrary epoch after the supernova explosion. The observer located along the z-axis and beyond the right edge of the diagram would see light echoes in the x-y plane (the y is perpendicular to the drawing). The SN is located at the origin and θ denotes the scattering angle.

dimensional scattering dust distributions has been given in various studies (Chevalier, 1986; Sparks, 1994; Sugerman, 2003; Tylenda, 2004; Patat, 2005). Here, we just briefly define the geometry used through this paper, also shown in Figure 2.1, which considers the SN event as an instantaneous flash of radiation. The locus of constant light travel time is an ellipsoid with the supernova at one focus which we refer to as an iso-delay surface. The ellipsoid grows with time as the light propagates in space.

The angular radius of the light echo (α) can be easily measured in two-dimensional images. The SN is centered at the origin of the plane, the x and y give the coordinates of the scattering materials in the plane of the sky. The projected distance ($\rho = \sqrt{x^2 + y^2}$) of scattering material to the SN perpendicular to the DLOS is related to the distance (D) to the SN as $\tan\alpha = \rho/D$, ϕ gives the position angle (PA). Because D is significantly larger compared to other geometric dimensions, the light echo can be very well approximated by a paraboloid, with the SN lying at its focus. ρ can be obtained by

$$\rho = \sqrt{ct(2z + ct)}. \tag{2.1}$$

where t is the time since the radiation burst, z gives the foreground distance of the scattering material along the line of sight, and c denotes the speed of light. The distance r of the scattering material from the SN is:

$$r = \frac{1}{2}\left(\frac{\rho^2}{ct} + ct\right) \tag{2.2}$$

The scattering angle can be obtained from: $\cos\theta(\rho, t) = z/(z + ct)$, or, $\tan\theta = \rho/z$.

2.1.2 Supernova 2014J in M82

The nearby Type Ia SN 2014J in M82 (3.53±0.04 Mpc, Dalcanton et al., 2009) offers the rare opportunity to study the physical properties and spatial distribution of dust particles along *and close to* the DLOS and as well in the vicinity of the SN. SN 2014J suffers from heavy extinction (A_V = 2.07, Foley et al., 2014) and is located behind a large amount of interstellar dust (Amanullah et al., 2014). Additionally, the absorption profiles of Na and K lines from high-resolution spectroscopy exhibit more than ten extragalactic absorption components, indicating the extinction along the DLOS is caused by the combined presence of a large number of distinct interstellar dust clouds along the DLOS (Patat et al., 2015). SN 2014J was discovered on Jan 21.805 UT by Fossey et al. (2014). Later observations constrained the first light of the SN to Jan. 14.75 UT (Zheng et al., 2014; Goobar et al., 2014).

SN 2014J reached its $B-$band maximum on Feb. 2.0 UT (JD 2,456,690.5) at a mgnitude of 11.85±0.02 (Foley et al., 2014). Continuous photometric and spectroscopic observations through late phases have been made by various groups (Johansson et al., 2017; Lundqvist et al., 2015; Bonanos & Boumis, 2016; Srivastav et al., 2016; Porter et al., 2016; Sand et al., 2016).

There is clear evidence that the strong extinction measured from SN 2014J is caused primarily by interstellar dust (Patat et al., 2015; Brown et al., 2015), although a mix of interstellar and circumstellar dust is also possible (Foley et al., 2014; Bulla et al., 2016). Several independent studies, including photometric color fitting from Swift/UVOT and *HST* (Amanullah et al., 2014), near-UV/optical grism spectroscopy from Swift UVOT (Brown et al., 2015), *HST* STIS spectroscopy and WFC3 photometry (Foley et al., 2014), reddening curve fitting near the SN maximum using the silicate-graphite model (Gao et al., 2015), as well as optical spectroscopy from Goobar et al. (2014) found an $R_V \sim 1.4$ towards SN 2014J. Moreover, ground-based broad-band imaging polarimetry (Kawabata et al., 2014; Srivastav et al., 2016) and spectropolarimetry (Patat et al., 2015; Porter et al., 2016) have shown that the polarization peak due to interstellar dust extinction is shortward of $\sim 0.4 \mu m$, which indicates that this line of sight has peculiar Serkowski parameters (see Patat et al., 2015). This polarization wavelength dependence can be interpreted in terms of a significantly enhanced abundance of small grains (Patat et al., 2015). Models considering both interstellar dust and circumstellar dust simultaneously and fitted to observed extinction and polarization (Hoang et al., 2015) find that a significant enhancement (w.r.t. the Milky Way) in the total mass of small grains ($<$ 0.1 μm) is required to reproduce low values of R_V. Multiple time-invariant Na I D and CaII H&K absorption features as well as several diffuse interstellar bands (DIBs) have also been identified (Graham et al., 2015b; Jack et al., 2015). Those are most likely associated with multiple dust components of interstellar material along the DLOS.

The nature (amount and distribution) of circumstellar material is of interest when probing the possible diversity of progenitors of type Ia SNe and for accurately correcting the extinction when using type Ia SNe as standard candles. Johansson et al. (2017) find no evidence for heated dust in the CSM of SN 2014J with r$< 10^{17}$ cm (~ 39 light days). Graham et al. (2015b) reported variable interstellar K I lines in high-resolution spectra, which may form about 10 light years ($\sim 10^{19}$ cm) in front of the SN.

The extremely dusty environment in M82 and its relative proximity to Earth lead to the expectation of complex and evolving light echoes if SN 2014J exploded inside the galactic disk. In fact, Crotts (2015) discovered the first light echoes surrounding SN 2014J in *HST* images from September 5 2014, 215.8 days past B-band maximum light (referred to as +216 d hereafter) on JD = 2456690.5 (Foley et al., 2014). The echo signal tends to be associated with pre-explosion nebular structures in M82 (Crotts, 2015).

In the following, we present the evolution of multiple light echoes of SN 2014J as revealed by new *HST* ACS/WFC multi-band and multi-epoch imaging around $\sim$277 days and $\sim$416 days past B-band maximum (referred to as +277 d and +416 d below). We will also qualitatively discuss similar archival WFC3/UVIS images obtained on +216 d and +365 d.

2.2 Observations and Data Reduction

Late-time observations of the light echoes around SN 2014J discussed in this paper result from a *Hubble Space Telescope (HST)* Wide Field Camera 3 UVIS channel (*HST* WFC3/UVIS) program (#13626; PI:Crotts) to observe properties of the light echoes and progenitor environment around SN 2014J and an Advanced Camera for Surveys/Wide Field Channel (*HST* ACS/WFC) program (#13717; PI: Wang) to probe the dusty environment surrounding SN 2014J in M82. A log of observations is assembled in Table 2.2.

We use bright HII regions to align exposures in different filter combinations and epochs through *Tweakreg* in the *Astrodrizzle* package (Gonzaga et al., 2012). Observations obtained with three polarizers are needed to calculate the Stokes vectors, but the

Table 2.2. Log of observations of SN 2014J with *HST* WFC3/UVIS and ACS/WFC POLV

HST	Filter	polarizer	Date of 1^{st} Obs.	Exp. Time	Epoch[a]	Date of 2^{nd} Obs.	Exp. Time	Epoch[a]
Camera			(UT - 2014)	(s)	(Days)	(UT - 2015)	(s)	(Days)
WFC3/UVIS[b]	F438W	N/A	09-05 19:12:57	8×64	215.8	02-02 05:24:41	12×128	365.2
	F555W	N/A	09-05 19:29:44	4×64	215.8	02-02 05:06:06	12×32	365.2
	F555W	N/A	09-05 22:05:11	8×32	215.9	N/A	N/A	N/A
	F814W	N/A	09-05 20:32:05	8×64	215.9	N/A	N/A	N/A
ACS/WFC[c]	F475W	POL0V	11-06 00:24:42	3×130	276.5	03-25 01:56:17	3×400	415.6
	F475W	POL120V	11-06 00:42:24	3×130	276.5	03-25 03:22:43	3×400	415.6
	F475W	POL60V	11-06 01:00:03	3×130	276.5	03-25 03:53:40	3×400	415.7
	F606W	POL0V	11-06 01:18:11	2×40	276.6	03-27 10:17:38	3×60	417.9
	F606W	POL120V	11-06 01:59:48	2×40	276.6	03-27 11:10:48	3×60	418.0
	F606W	POL60V	11-06 02:13:58	2×40	276.6	03-27 11:30:17	3×60	418.0
	F775W	POL0V	11-06 02:23:28	2×30	276.6	03-27 11:50:26	3×20	418.0
	F775W	POL120V	11-06 02:37:21	1×55	276.6	03-27 12:58:00	3×20	418.0
	F775W	POL60V	11-06 02:41:46	1×55	276.6	03-27 13:02:17	3×20	418.0

[a] Days after B maximum on 2014 Feb. 2.0 (JD 2 456 690.5).

[b] Observations result from *HST* WFC3/UVIS, program (#13626; PI: Crotts)

[c] Observations result from *HST* ACS/WFC, program (#13717; PI: Wang)

intensity maps (Stokes I) are the only input to this analysis.

$$I = \frac{2}{3}[r(POL0) + r(POL60) + r(POL120)],$$

where $r(POL0)$, etc. are the count rates in the images obtained through the three polarizers. Figure 2.2 shows the field around SN 2014J.

We perform background subtraction to better reveal the faint and time-variant light echo signals. For observations on +277 d and +416 d with *HST* ACS/WFC and filters F475W, F606W, and F775W, we found no pre-SN Hubble images of the region through filters consistent with our observations. The most recent *HST* images of SN 2014J obtained on April 8 2016, (+796 d) with the same photometric and polarimetric filter combinations were subtracted from the observations on +277 d and +416 d. For the observations on +216 d and +365 d with *HST* WFC3/UVIS in passbands F438W, F555W, and F814W, pre-SN

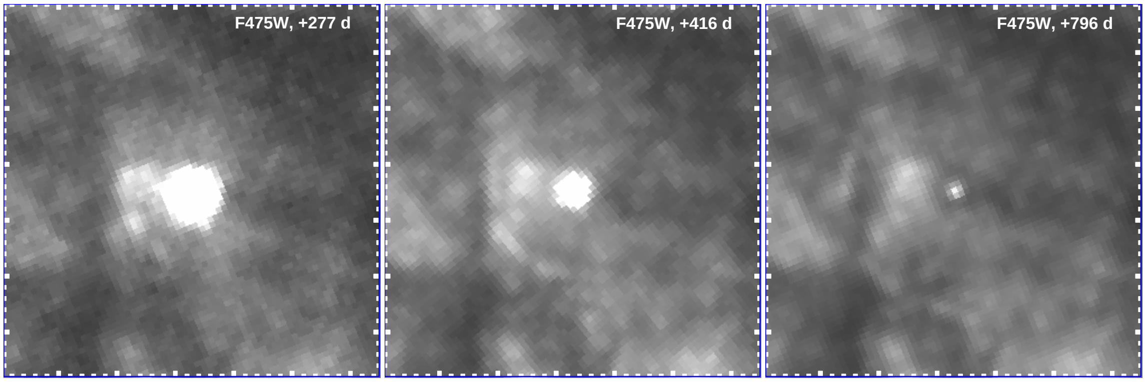

Figure 2.2 *HST* ACS/WFC $F475W$ images of SN 2014J obtained at different epochs as labeled. Each square measures $3''.2$= 54 pc along its sides (North is up, East is left). The distance between little tick marks corresponds to $0''.1$.

images obtained on March 29 2006 (program $\#$10776; PI:Mountain) with *HST* ACS/WFC in the F435W, F555W, and F814W were used as background templates, respectively. For each band, the background templates were scaled and subtracted from the intensity map.

The resulting images (Figure 2.3) clearly reveal the shape of the light echoes around SN 2014J. Negative signals (black in Figure 2.3) represent the light echoes on +796 d while positive (white) signals trace the light echoes on +277d and +416 d, respectively. In each subpanel of Figure 2.3, we show the light echoes with background removed (labeled 'Image' at bottom), the scaled and distortion-corrected PSF (labeled 'PSF' on the left), and the residual around the SN after PSF subtraction (labeled 'Res' on the right). Point-spread functions (PSF) appropriate to the SN position were generated for each bandpass and epoch with TinyTim (Krist, 1993; Krist & Hook, 2008). The upper row displays the observations at earlier epoches (+216 d for $F438W$ and $F555W$, +277 d for $F475W$, $F606W$, and $F775W$), and the lower row depicts the observations at later epochs (+365 d for $F438W$ and $F555W$, +416 d for $F475W$, $F606W$, and $F775W$). For better visibility, Figure 2.4 provides a zoom-in of the PSF-subtracted images ('Res') in each panel of Figure 2.3.

2.3 Analysis and Results

2.3.1 Total flux of the SN

Photometry of SN 2014J at four epochs was performed in the background subtracted images described above, and shown in Table 2.3. Measurements were made with a circular aperture of $0.''4$ (8 pixels in the ACS/WFC FOV and 10 pixels in the WFC3/UVIS FOV) in the WFC3/UVIS F438W, F555W, F814W images from +216 d, and the F438W and F555W images from +365 d. We applied aperture corrections according to Hartig (2009) and Sirianni et al. (2005) to estimate the total flux from SN 2014J. The photometric uncertainties in Table 2.3 include the Poisson noise of the signal, the photon noise of the background, the readout noise contribution (3.75 electrons/pixel for ACS/WFC), and the uncertainties in aperture corrections. These quantities were added in quadrature. The magnitudes are presented in the Vega system with zero points from the CALSPEC archive. The total flux of the source within the aperture equals the product Total Counts × PHOTFLAM, where PHOTFLAM is the inverse sensitivity (in erg cm^{-2} sec^{-1} $\mathrm{angstrom}^{-1}$ and representing a signal of 1 electron per second). For WFC3/UVIS images, we adopted the values of the PHOTFLAM keyword in the image headers. However, for the ACS/WFC polarizer images, which were corrected for the throughputs of the polarizers to generate the intensity maps, we discarded the default PHOTFLAM values. Instead, we adopted the most up-to-date PHOTFLAM values in the ACS filter bands for images obtained without polarizers (Bohlin, 2012). This is required by the mismatch between (i) the polarizer throughput curves used by SYNPHOT for unpolarized sources and (ii) the values found by comparing unpolarized sources in both the polarizing and non-polarizing filters (Cracraft & Sparks, 2007). Therefore, the PHOTFLAM keywords in ACS/WFC polarized images

---

http://www.stsci.edu/hst/observatory/cdbs/calspec.html, or http://www.stsci.edu/hst/acs/analysis/zeropoints/#vega and http://www.stsci.edu/hst/wfc3/phot_zp_lbn

http://www.stsci.edu/institute /software_hardware/stsdas/synphot

Table 2.3. *HST* photometry of SN 2014J and light echoes (total echo profile)

t[a]	F438W$_{SN}$	F555W$_{SN}$	F814W$_{SN}$	F438W$_{LE}$	F555W$_{LE}$
215.8	17.610±0.016	16.446±0.011	15.301±0.011	22.05±0.36	21.12±0.06
365.3	19.735±0.011	18.715±0.013	N/A[b]	21.53±0.13	20.87±0.06
t[a]	F475W$_{SN}$	F606W$_{SN}$	F775W$_{SN}$	F475W$_{LE}$	F606W$_{LE}$
276.5	17.467±0.002	17.343±0.002	16.354±0.005	21.16±0.03	20.73±0.08
415.6[c]	19.568±0.002	19.516±0.004	17.888±0.008	21.37±0.02	20.98±0.05

[a] Days after B maximum, 2014 Feb. 2.0 (JD 245 6690.5).

[b] SN 2014J was not observed in $F814W$ at +365 d.

[c] +417.9 d for $F606W$, +418.0 d for $F775W$.

are not applicable to intensity maps derived from polarized images. Polarization properties of SN 2014J will be discussed in a separate paper (Yang et al., in prep.).

2.3.2 Residual images

Two main echo components are evident. In Figure 2.4 we show a luminous quarter-circle arc and a diffuse ring at angular distance larger than $0''.3$ from the SN. Closer to the SN, uncertainties in the PSF correction prevent reliable detections. On +277 d, the most notable features of the light echoes in F475W are three luminous clumps at angular radius $\alpha = 0''.60$ and PAs 80°, 120°, and 150°, measured from north (0°) through east (90°). These clumpy structures are already present on +216 d at the same PAs but appear smoother and more extended. They eventually evolve into a fairly continuous luminous quarter-circle arc seen on both +365 d and +416 d extending from PA = 60°-170°. Images obtained on +216 d with $F438W$ and $F555W$ show the luminous arc at angular radii $\alpha = 0''.54$ and $\alpha = 0''.69$, over roughly the same range in PA, in agreement with Crotts (2015). However, for the arc we find a foreground distance of the scattering material, which ranges from 226 to 235 pc in the four epochs (Table 2.4) and has a mean value of 228±7 pc. This is different from the foreground distance of $\sim$ 330 pc discussed for

Table 2.4. Geometric properties of (unresolved) luminous-arc light-echo (LE) components

LE #	Epoch[1] (Day)	Angular Radius α ($''$)	Offset ($''$)	Foreground Distance z (pc)	Projected Radius ρ (pc)	Scattering Angle θ (°)
Arc	215.8	0.539±0.020	0.009±0.014	234.6±18.2	9.22±0.36	2.25±0.20
	276.5	0.599±0.014	0.006±0.015	226.3±11.8	10.25±0.27	2.60±0.15
	365.3	0.689±0.020	0.011±0.014	226.4±14.1	11.79±0.37	2.98±0.21
	415.6	0.735±0.012	0.012±0.010	226.6±9.0	12.58±0.25	3.18±0.14

[1] Days after B maximum on 2014 Feb. 2.0 (JD 245 6690.5).

this prominent echo component by Crotts (2015). This discrepancy may be due to the difficulties and uncertainties in subtracting the PSF in earlier epoch when the SN is still bright, or in distinguishing the multiple light echo components identified in our multi-epoch data.

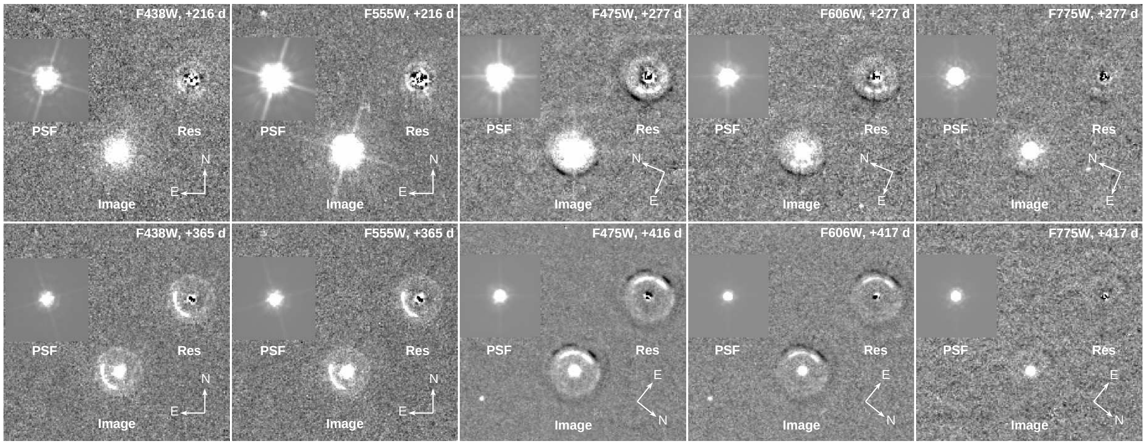

Figure 2.3 Background-subtracted images of the SN (‘Image’), the TinyTim PSF (Krist, 1993; Krist & Hook, 2008), and the residuals around the SN after PSF subtraction (‘Res’). Background structures in F438W and F555W were removed by subtracting scaled pre-SN archival F435W and F555W HST images. Background in $F475W$, $F606W$, and $F775W$ was corrected for by subtracting the respective most recent +796 d image; therefore, the +796 d echoes appear as negative structures. Note the different orientations.

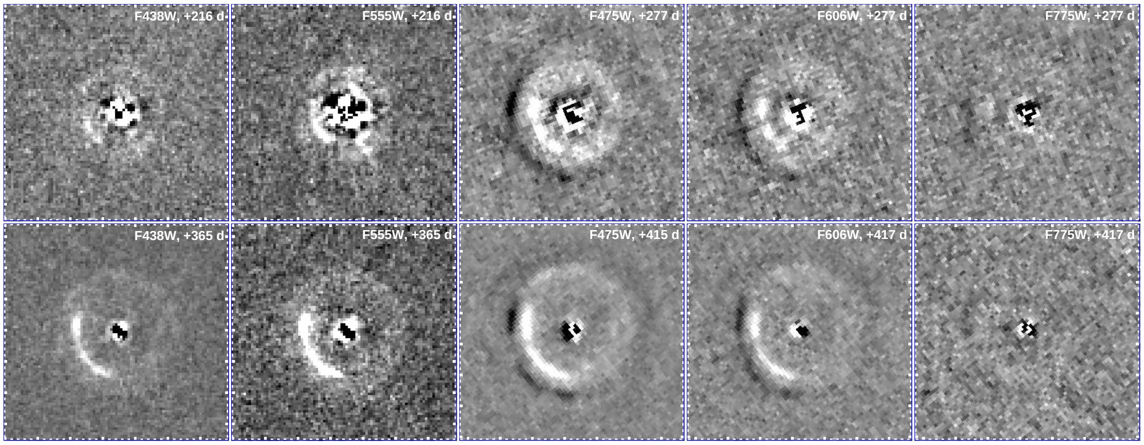

Figure 2.4 A zoom-in view of the background-corrected light echoes shown in Fig. 2.3. North is up and East is left. The distance between each little tickmark is $0''.1$. Each square measures $3''.4$= 58 pc along its sides. The diffuse and radially extended light echo profiles can be clearly identified in all panels except for $F438W$ (+216 d) and $F775W$ (all epochs). Note the uneven signal distribution with position angle in the rings and the consistency of the overall patterns at different epochs. A luminous arc is visible in the lower left quadrant and not resolved in the radial direction. This is at variance with the appearance of the complete, radially diffuse rings.

To enable a more quantitative description of the light echoes and their evolution, we performed photometry on them in backgound-subtracted images (Figure 2.4). We measured the surface brightness of the light echo profile at different radii and over different ranges in PA. Fan-shaped apertures centered on the SN were used to sample the intensity. The width in PA of each aperture is $45°$. Contrary to the luminous arc, the diffuse echo can be seen over the full range in PA from 0° to 360°. But it does not exhibit a common radial profile (Figures 2.5 and 2.6).

In the following subsections, we will use these measurements to investigate the evolving profile of the light echoes, conduct geometric and photometric analyses, and estimate the dust distribution and scattering properties responsible for the observed light echoes along and close to the DLOS. A function characterizing the properties of the scattering

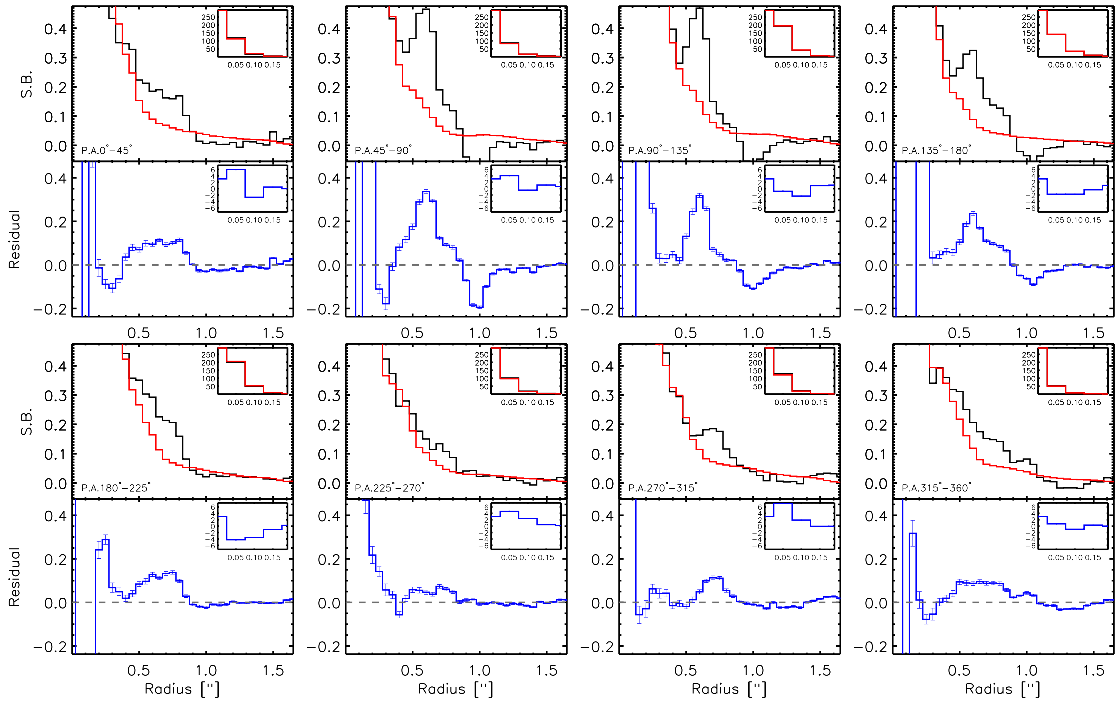

Figure 2.5 $F475W$ band radial surface-brightness profile centered on SN 2014J at 277 days after B-band maximum. Different curves in each panel show the surface brightness of the background-subtracted image (black), the TinyTim PSF (red), and the residual after PSF subtraction (blue). Each panel depicts a different 45° sector in PA as labeled. The lower subpanels of each pair display the residuals after PSF and background subtraction; the luminous arc at $\sim 0''.6$ is prominent in the PA bins from 45° to 180°. The diffuse light echoes can be identified at other PAs, by continuous positive signals from the early epoch of +277 d and continuous negative signals due to the subtraction of the intensity map on +796 d. Surface brightnesses are in units of $10^{-16}\mathrm{erg\ s^{-1} angstrom^{-1} arcsec^{-2}}$. The inserts display the radial run of the functions (identified by their colors) over the innermost 0″.2.

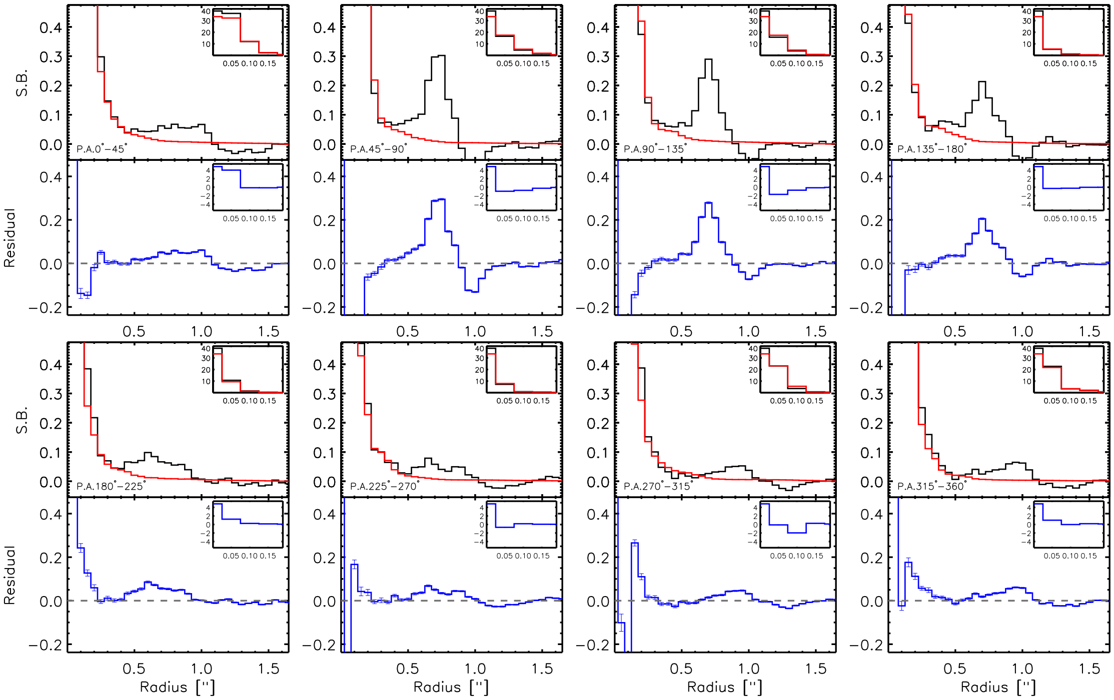

Figure 2.6 Same as Figure 2.5 except for epoch being +416 d.

material is constructed to represent the brightness evolution of the observed light echoes on +277 d and +416 d.

2.3.3 Geometric properties of the light echoes

A comprehensive discussion of the formation of light echo arcs is available from Tylenda (2004). In the context of this paper, it is sufficient to recall that a circular light echo is created from the intersection of the dust slab with the iso-delay parabaloid. Any uneven distribution of material in the slab results in an uneven flux distribution along the circle, and the light echo may be composed of incomplete arcs. A dust slab always produces a (complete or incomplete) circular light echo, irrespective of its inclination with respect to the line of sight. When a dust slab is not perpendicular to the line of sight, the center of the light echo circle will not coincide with the SN position, and it moves with time.

The luminous arc echo is unresolved with a full width at half maximum (FWHM) of the radial profile approximately that of the SN measured in the same images, i.e. $\sim$ $0''.1$ (2 pixels). Therefore, we consider the luminous arc was formed by a thin dust slab intersecting the line of sight. We have fitted circles to the positions of the luminous arc at all available epochs. None of them are significantly decentered from the SN. This implies that the dust slab producing the arc echo is fairly perpendicular to the line of sight. Table 2.4 summarizes the geometric properties measured from the luminous arc.

In addition to the luminous arc, a radially extended and diffuse structure is identified, which on +277 d is present in $F475W$ and $F606W$ and spread over $\alpha = 0''.40$ to $\alpha = 0''.90$. This structure can also be noticed on +365 d in $F438W$ and $F555W$ (from $\alpha = 0''.47$ to $\alpha = 1''.03$). It appears more clearly on +416/417 d in $F475W$ and $F606W$ (from $\alpha = 0''.50$ to $\alpha = 1''.08$) because for these observations longer exposure times were used. The epochs of observation and the exclusion of the inner $0''.3$ limit the foreground distances explored from $z = 100$ pc to $z = 500$ pc. On +216 d, the diffuse component cannot be identified in $F438W$ but is marginally seen in $F555W$. However, the inner and outer radii of the diffuse structure cannot be well determined because of uncertainties in the PSF subtraction. The diffuse light echo observed on +277 d can be produced by a dust cloud intersecting the iso-delay surface over a wide range in foreground distance. The line-of-sight extent of this diffuse dust cloud is indicated by the filled profile of the echoes. Therefore, a continuous dust distribution over a certain range of foreground distances along the line of sight is required.

In each panel of the radial profiles in Figures 2.5 and 2.6, the radially-resolved positive flux excesses (on +277 d and +416 d), and also the radially-extended negative flux due to the subtraction of the light echo on +796 d, suggest the presence of an extended and inhomogeneous foreground dust distribution. Outside the $\sim 0''.3$ region, as discussed earlier, the imperfect PSF subtraction makes the detection of echoes unreliable. The most prominent structure with an intensity peak at the second and third curve near the top in Figure 2.5 can be seen clearly on +277 d with an angular radius of $\sim 0''.60$, which at the distance of M82 (3.53±0.04 Mpc, Dalcanton et al., 2009) is at a radius $\rho = 10.3$ pc from the SN in the plane of the sky. By +416 d, the radius has increased to $\sim 0''.735$ or $\rho = 12.6$ pc from the SN. The scattering angles are $2^\circ.6$ and $3^\circ.2$, respectively.

2.3.4 Light echo mapping of the foreground dust distribution

To our knowledge, and with the exception of SN 1987A in the LMC (Crotts, 1988, Suntzeff et al., 1988), this is the first radially-extended light echo detected from any SN. For epochs discussed in this paper, the diffuse echo component around SN 2014J reveals the SN-backlit ISM over $\sim$ 40 pc $\times$ 40 pc around the DLOS. Standard methods for estimating the optical properties of the ISM towards the supernova only consider the extinction along the DLOS. They include the spectrophotometric comparison between the observed

SN and an unreddened SN or template, and comparing the integrated echo flux with the surface brightness calculated from the scattering properties of various dust models. But the resolved dust echoes of SN 2014J and their temporal evolution in the gas-rich and very nearby galaxy M82 provide an unprecedented opportunity to do better. In the following, we take advantage of this to measure the scattering properties of the ISM at different foreground distances and PAs relative to SN 2014J.

We assume that dust scattering follows the Henyey–Greenstein phase function (Henyey & Greenstein, 1941):

$$\Phi(\theta) = \frac{1 - g^2}{(1 + g^2 - 2gcos\theta)^{3/2}} \tag{2.3}$$

where $g = \overline{cos\theta}$ is a measure of the degree of forward scattering. With $L_\lambda(t)$ as the number of photons emitted per unit time by the SN at a given wavelength, $F_\lambda(t) = L_\lambda(t)/4\pi D^2$ is the number of photons observed at time t. D is the distance to the SN. For the modeling of our observations, t is the time of the light-echo observation, t_e denotes the time when photons emitted by the SN would be directly observed along the DLOS, and $F_\lambda(t - t_e)$ is the brightness of the SN at $(t - t_e)$. At t, the photons emitted at the same time as t_e, but experiencing scattering leading to a light echo, arrive at the observer with a time delay $(t - t_e)$.

For a single short flash of light of duration Δt_e emitted by the SN at t_e, $F_\nu(t-t_e) = 0$ for $t \neq t_e$ and $\int_0^t F_\nu(t - t_e)dt_e = F_\nu(t - t_e)|_{t=t_e}\Delta t_e$. Then, the surface brightness, Σ, of a scattered-light echo at frequency ν and arising from an infinitely short (δ function) light pulse is given by:

$$\Sigma_\nu^\delta(\rho, \phi, t) = n_d Q_s \sigma_d \, \frac{F_\nu(t - t_e)|_{t=t_e}\Delta t_e}{4\pi r^2} \left|\frac{dz}{dt}\right| \Phi(\theta) = n_d Q_s \sigma_d \frac{\int_0^t F_\nu(t - t_e)dt_e}{4\pi r^2}\left|\frac{dz}{dt}\right|\Phi(\theta) \tag{2.4}$$

Where n_d is the volume number density of the scattering material in units of cm^{-3}; Q_s is a dimensionless number describing the scattering efficiency of the dust grains; σ_d is the geometric cross-section of a dust grain, $\Phi(\theta)$ is the unitless scattering phase function. This means that the surface brightness at a certain instance of the light echo at $t = t_e + (t - t_e)$ is determined by the flux emitted from the SN at t_e, together with the local geometric properties of the iso-delay surface at $t - t_e$.

In reality, the SN emission has a finite duration. $F_\nu(t - t_e)$ is no longer a δ function, and the surface brightness of the light echo unit at a certain frequency Σ_ν is the time integral of $F_\nu(t - t_e)$ from 0 to t:

$$\Sigma_\nu(\rho, \phi, t) = \frac{Q_s \sigma_d}{4\pi} \int_0^t \frac{n_d F_\nu(t - t_e) dt_e}{r^2} \left| \frac{dz}{dt} \right| \Phi(\theta) \tag{2.5}$$

Recalling that

$$z = \frac{\rho^2}{2ct} - \frac{ct}{2} \tag{2.6}$$

one can easily find:

$$\frac{dz}{dt} = -\frac{c}{2}\left(\frac{\rho^2}{c^2 t^2} + 1\right),\ r = z + ct = \frac{ct}{2}\left(\frac{\rho^2}{c^2 t^2} + 1\right) \tag{2.7}$$

Therefore,

$$\Sigma_\nu(\rho, \phi, t) = \frac{Q_s \sigma_d c}{2\pi} \int_0^t \frac{n_d(\rho, \phi, t)}{c^2 t^2 + \rho^2} \Phi(\theta)\ F_\nu(t - t_e) dt_e \tag{2.8}$$

Because of the relative proximity of M82, some light echoes around SN 2014J are resolved by *HST* at late phases, and each pixel represents the surface brightness of the light echo multiplied by the physical area covered by the pixel in the sky.

Therefore, in order to compare the model flux distribution with the flux in a 2-dimensional image, one needs to integrate the model flux over the physical depth covered by the pixel. Since each pixel has size $\Delta x \Delta y$, and $\Delta x = \Delta y$, this implies:

$$Im_\nu(x, y, t) = \int_{x-\frac{\Delta x}{2}}^{x+\frac{\Delta x}{2}} \int_{y-\frac{\Delta y}{2}}^{y+\frac{\Delta y}{2}} \Sigma(x, y, t) dx dy \tag{2.9}$$

The geometric factor is determined by the radial distance to the SN, $\rho = \sqrt{x^2 + y^2}$. Therefore, in the tangential direction inside each pixel, we approximate the integration by assuming that $n_d(x, y, t)$ is invariant over the angle $\Delta\phi$ subtended by a single pixel. Furthermore, the angular size of each ACS/WFC pixel is $0''.05$. At the distance of $D = 3.53 \pm 0.04$ Mpc, the corresponding physical pixel size in the sky is:

$$pixscale = (3.53 \pm 0.04)\ \mathrm{Mpc} \times tan(0''.05) = (0.86 \pm 0.01)\ pc = \Delta x = \Delta y \tag{2.10}$$

Recall the geometric configuration of the iso-delay light surface at +277 d presented by Figure 2.1. In Figure 2.7, we modify this schematic diagram to demonstrate how we use a 2-dimensional image to map the ISM in 3D. The gray-shaded fields on the vertical axis show the pixelation of the sky view by the camera, with each pixel measuring 0.86 pc on both sides. Δz is the position-dependent line-of-sight extent of the foreground column covered by each pixel. Gray-shaded rectangles superimposed to the iso-delay light surface mark columns of ISM which would be responsible for respective light echoes as projected onto the sky. The fixed size of the sky pixels leads to varied lengths of the foreground columns of ISM. If the ISM is homogeneously distributed in the x/y plane, the total per-sky-pixel extinction of the scattering materials as revealed by the light echo can be estimated by summing up the extinction along each rectangular column of ISM intersecting the iso-delay light paraboloid. Comparison of the extinction by the scattering materials to the extinction along the DLOS (marked by the gray line on the z axis in Figure 2.7) may reveal if they are caused by the same dust mixture and perhaps even the same

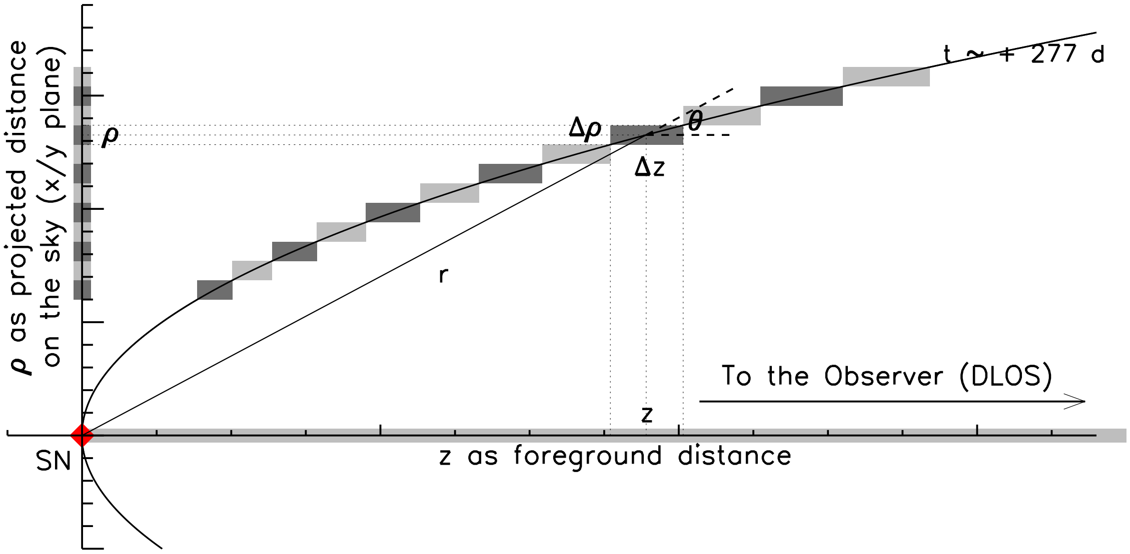

Figure 2.7 Schematic diagram from Figure 2.1 adapted to real scale. The paraboloid represents the iso-delay light surface at $\sim$ 277 d. The gray-shaded squares on the vertical axis indicate the pixelation of echo signals measured from images of this epoch. Rectangles at the same observed angular distance delineate the range in z, over which dust can produce an unresolved light echo. Different gray levels only serve to distinguish immediately neighboring pixels.

dust cloud.

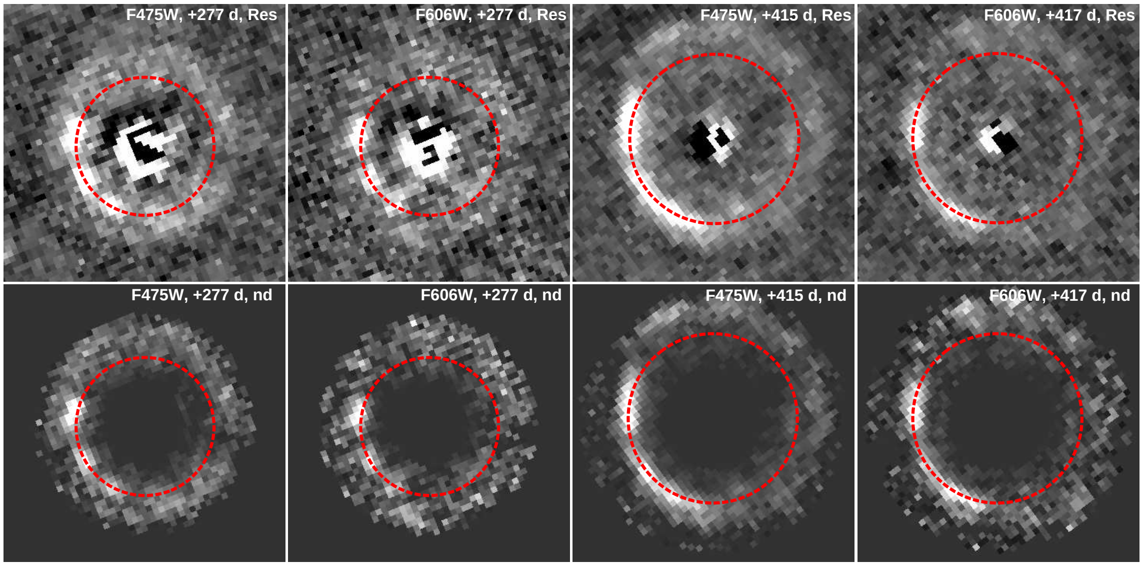

Figure 2.8 Intensity maps of the backgound- and PSF-subtracted images (labeled ‘Res’) and scaled volume number-density maps (‘nd’) showing the relative column density calculated from the flux and location in space of each pixel. North is up and east is left. Epoch and passband of the observations are labeled. Dashed circles trace the dust slab at $z \sim$228 pc, which is responsible for the luminous echo arc appearing with different diameter at different epochs. Overdensities can be identified at PAs 60° – 180° along the lunimous arc and also at PAs 0° – 60° and larger radii in $F475W$ and $F606W$ +416/+417 d.

Now we can compare the intensity map obtained from the observations with the light echo modeled at each physical position for a given time t of the observation as follows:

$$Im_{\nu}(x,y,t) = \frac{\omega C_{ext} c}{2\pi} \Delta x \int_{x-\frac{\Delta x}{2}}^{x+\frac{\Delta x}{2}} dx \int_{0}^{t} \frac{n_d(x,y,t)}{c^2t^2+\rho^2} \Phi(\theta) F_{\nu}(t-t_e) dt_e \tag{2.11}$$

2.3.5 Extinction of the scattering materials

The optical properties of the dust grains responsible for the light echoes around SN 2014J can be deduced within each observed pixel. We estimate the extinction properties of the scattering materials based on a single-scattering-plus-attenuation approach (see Section 5 of Patat, 2005 for more details). *Conversions from the intensity map to the number-density map ('nd') are presented by Figure 2.8 based on Equation 12.* We follow the sampling in Figures 2.5 and 2.6 and present the deduced optical properties of the dust grains for the PA sector 45° - 90°, which includes the brightest part of the luminous arc, and PA sector 315° - 360°, which covers the diffuse echo ring observed with the highest S/N. They are shown in Figure 2.9 for $F475W$ and Figure 2.10 for $F606W$, both on +277 d. In these diagrams, rectangular coordinates x and y are replaced with polar coordinates ρ and ϕ, and the abscissa corresponds to the physical distances in the plane of the sky. The left ordinate represents the quantity $\omega C_{ext} n_d(\rho, \phi, t)$, which is determined by the optical properties of the dust grains. The right ordinate shows $\omega C_{ext} n_d dz = \omega\tau$, where τ is the optical depth of the dust mapped onto a single pixel. By looking at the entire echo profile, we found that a major part of the luminous-arc echo spreads over 45° - 180° in PA, and the diffuse echo ring attained the highest S/N over 270°-360° in PA. For completeness, on-line Figures 2.14 and 2.15 present the same diagrams over the entire eight bins in PA.

We applied a Galactic extinction model with R_V=3.1 to the scattering materials and compare the reproduced extinction properties with the extinction along the DLOS. Discrepancies between the derived quantities and the assumed model will indicate that the extinction properties of the scattering dust are different from the Milky Way dust with R_V=3.1. For each photometric bandpass its pivot wavelength was used in interpreting the parameters from dust models. The extinction curve is obtained from Weingartner & Draine (2001) and Draine (2003a,b) . For C_{ext}, the extinction cross section per hydrogen nucleon H, we adopted 5.8×10^{-22} cm^2/H for $F475W$, and 4.4×10^{-22} cm^2/H for $F606W$; for the scattering phase function, we adopted $g = 0.555$ for $F475W$, and $g = 0.522$ for $F606W$, and n_d is the H volume number density in units of cm^{-3}.

---

ftp://ftp.astro.princeton.edu/draine/dust/ mix/kext_albedo_WD_MW_3.1_60_D03.all

For a uniform dust distribution in the x/y direction (in the plane of the sky), integrating $\omega\tau$ over each position angle will provide a rough estimate of the product of the total optical depth and the scattering albedo, which is the main value added by the separate analysis of light echoes. We applied the same extinction measured along the DLOS to the scattered light echoes and calculated the optical depth of the materials from scattering. This is labeled by the red text in the upper right of each panel of Figures 2.9 and 2.10. The inhomogeneity of the ISM in M82 has small scales as is indicated by the rapid variability of the strength of the echo with PA along the rings as well as with time. The optical depth along the DLOS has been measured by Foley et al. (2014) around maximum light as τ_B = 3.11(0.18) and τ_V = 1.91(0.17) based on A_B = 3.38(20), A_V = 2.07(18) and using the relation $A_\lambda = -2.5log_{10}(e)\tau_\lambda^{ext} = 1.086\tau_\lambda^{ext}$.

The hydrogen column number density along the line of sight is $n_H = \int_{LOS} n_d(z)dz$. Therefore, n_H can be obtained by dividing the total optical depth per bin in position angle by ωC_{ext} (Figure 2.9 for $F475W$ and Figure 2.10 for $F606W$). For example, for $F475W$ and +277 d, the maximum value of $\omega\tau(\rho, \phi, t)$ in the luminous arc was observed to be around 0.58. Using $\omega \sim 0.65$ for the Milky-Way dust model with R_V = 3.1 given by Weingartner & Draine (2001), n_H can be estimated to be $n_H = 0.58/\omega C_{ext} = 0.58/(0.65 \times 5.8 \times 10^{-22}$ cm^2/H) $\sim 1.5 \times 10^{21}$ H cm^{-2} in the bin which shows the densest part of the dust slab producing the luminous arc echo. This is ~15 times denser than the scattering material in the foreground of the Type-II plateau SN 2008bk (Van Dyk, 2013), for which the visual extinction of the dust responsible for the echo is $A_V \approx$ 0.05. It is also ~ 4 times denser than the ISM in the foreground of the Type II-plateau SN 2012aw (Van Dyk et al., 2015), for which the dust extinction in the SN environment responsible for the echo is consistent with the value that was estimated from observations of the SN itself at early times, i.e., A_V=0.24.

Figure 2.12 presents the three-dimensional dust distribution estimated for SN 2014J.

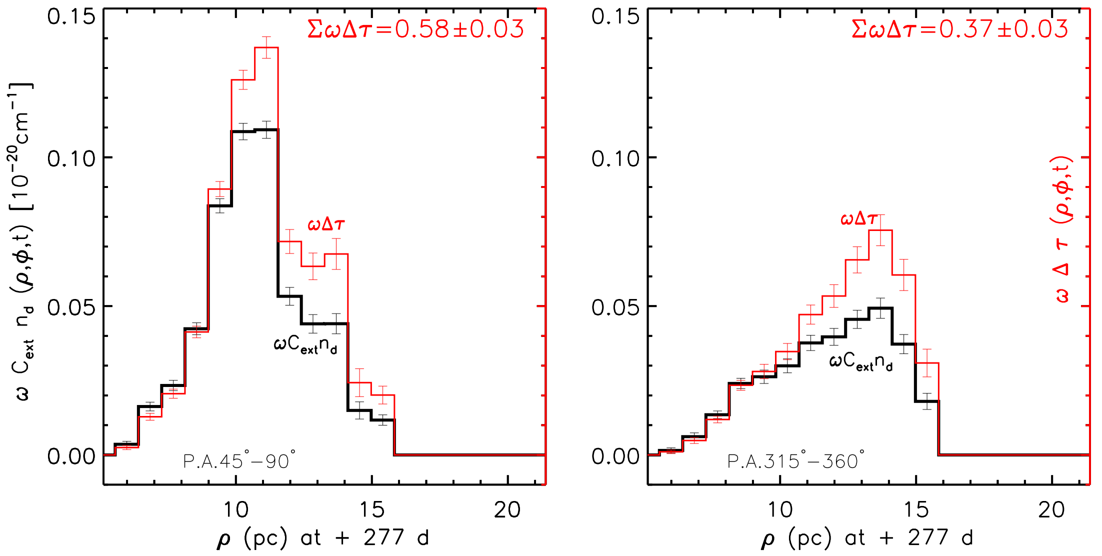

Figure 2.9 Radial profiles at different PAs (as labeled) of optical properties of the scattering material. The calculations are based on the density map (transformed from the residual image) in passband $F475W$ on +277 d. The left panel shows the luminous arc echo, and the right panel presents the diffuse ring echo. The x-axis shows the physical distances in the plane of the sky (ρ-direction). Black histograms represent $\omega C_{ext} n_d(\rho, \phi, t)$ in units of $10^{-20} cm^{-1}$ as shown on the left ordinate and can be used to infer the volume densities. Red histograms represent the dimensonless $\omega C_{ext} n_d dz = \omega\tau$ and share the tick marks of the left ordinate, from which column number densities can be deduced. The optical depth of the dust mapped onto a single pixel gives τ.

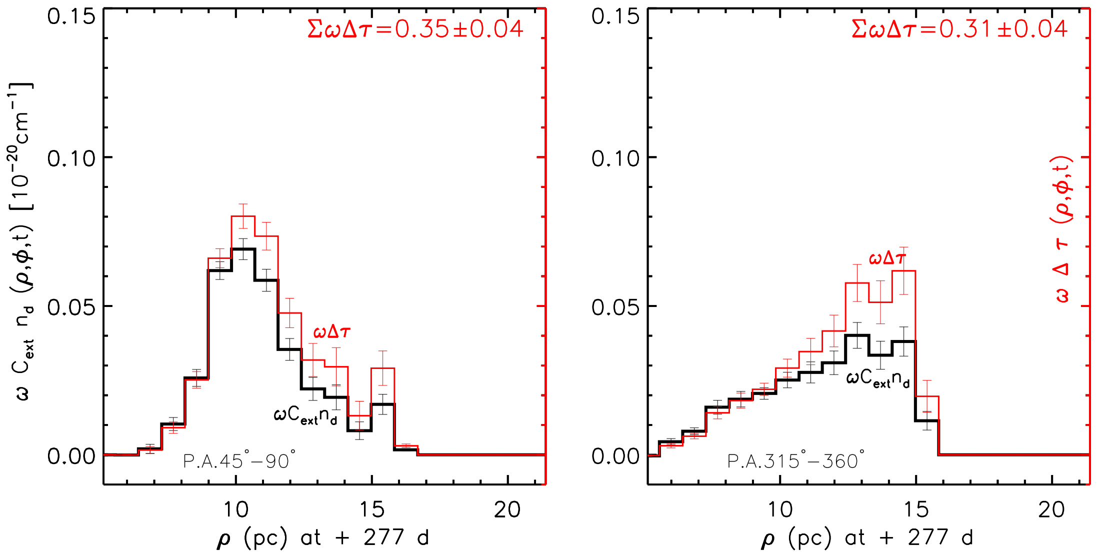

Figure 2.10 Same as Figure 2.9 except for $F606W$.

Data-points show the number densities as derived from two iso-delay paraboloids. Scattering materials producing the luminous arc and the diffuse echo, respectively were mapped out at epochs +277 d (inner layer) and +416 d (outer layer).

2.3.6 Scattering wavelength dependence of the ISM

From the scattering properties of the dust, its optical properties can be estimated by comparing the quantity $\omega C_{ext} n_d$ derived for $F475W$ and $F606W$. Figure 2.11 presents the division of the profiles of Figure 2.9 by Figure 2.10. This yields the wavelength dependence of the extinction cross-section. As the ordinate of Figure 2.11 we use $\omega\tau_{F475W}/\omega\tau_{F606W}$. Overplotted histograms show (in red) the number density of the scattering material derived from the strength of the echoes in $F475W$. The horizontal gray dashed lines mark the value of $\tau_{F475W}/\tau_{F606W} = A_{F475W}/A_{F606W} =$1.66, 1.30, and 1.19 for Milky Way-like dust with $R_V =$1.4, 3.1, and 5.5, respectively, according to the algorithm determined by Cardelli et al. (1989). Similar diagrams over the entire eight bins of PA are shown by Figure 2.16 in the electronic version.

Plausible estimates of $\omega\tau_{F475W}/\omega\tau_{F606W}$ can only be made in high-S/N regions of the echoes. In the left panel of Figure 2.11, the luminous arc at ρ = 10$\sim$11 pc has an average value $\omega\tau_{F475W}/\omega\tau_{F606W}$ $\sim$1.7 (dimensionless), shown by the black histograms. For the diffuse structure, the right panel indicates an average value $\sim$1.3. This difference in the wavelength dependence measured from the scattering optical depth indicates that the size of the grains in the thin dust slab producing the luminous arc are different from the grains in the foreground extended dust cloud producing the diffuse echo. While this difference is significant, one should be cautious about the inferred absolute values of R_V in this approach, considering the low signal-to-noise ratio and the large uncertainties.

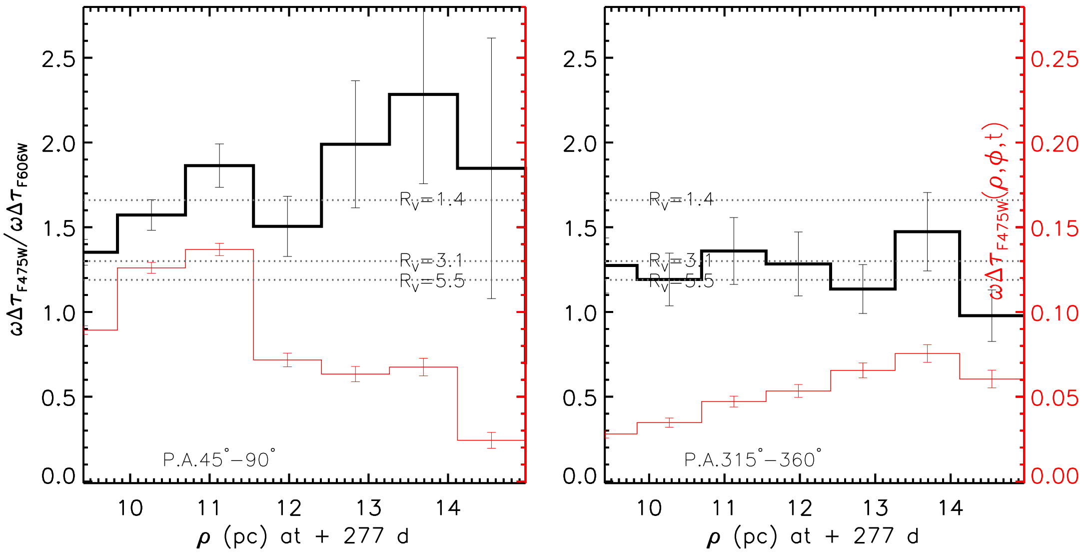

Figure 2.11 Radial run of the wavelength dependence of the scattering material characterized by $\omega\tau_{F475W}/\omega\tau_{F606W}$ on +277 d, shown by the black histograms. Red histograms represent the dimensionless quantity $\omega C_{ext} n_d dz = \omega\tau$, which is a measure of the strength of the echoes. The abscissa measures the physical distances (in pc) in the plane of the sky. The upper, middle, and lower horizontal dashed lines represent the values calculated for Milky Way extinction laws with R_V = 1.4, 3.1, and 5.5, respectively. The left panel includes the luminous arc echo at ρ = 10∼11 pc and $\omega\tau_{F475W}/\omega\tau_{F606W}$ ∼1.7. The right panel presents the diffuse ring echo, exposing a different wavelength dependence of scattering with $\omega\tau_{F475W}/\omega\tau_{F606W} \sim 1.3$.

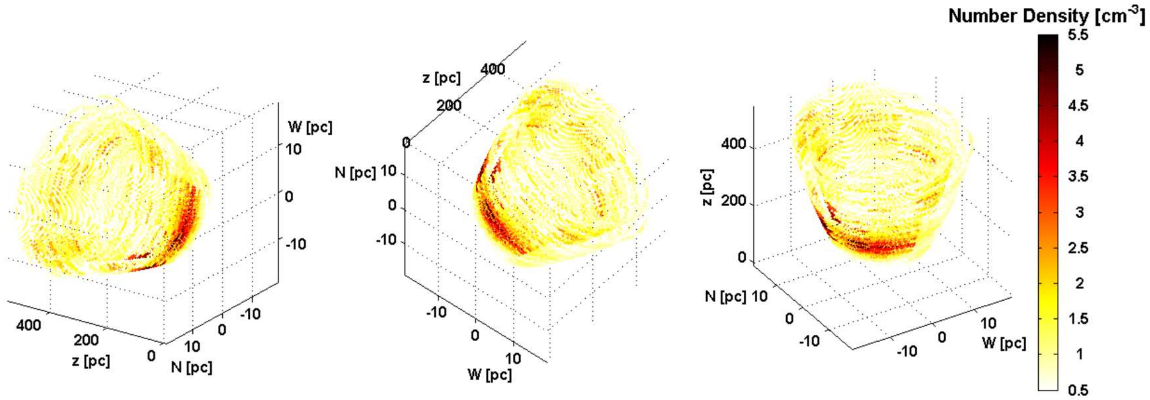

Figure 2.12 The three-dimensional dust distribution derived from the light echoes around SN 2014J. From left to right, the vertical axis corresponds to the directions East-West, North-South, and the DLOS (z). The color encoding of the number density of the dust is indicated by the vertical bar. The measurements map out density along iso-delay paraboloids as schematically depicted in Figure 2.1. They correspond to epochs +277 d and +416 d and are too close to one another to appear separately.

2.4 Discussion

The diffuse echo component favors a higher R_V than the luminous arc, corresponding to a less steep wavelength dependence of the extinction in the diffuse echo compared to the luminous arc. In general terms, this implies that the grains in the dust slab producing the luminous arc are smaller than those in the extended, diffuse ISM. The R_V value measured from the diffuse echo at $\rho \sim 10 - 14$ pc to the position of SN 2014J, i.e., $R_V \sim 3$, is close to that found by Hutton et al. (2015) by modelling the attenuation law based on near-ultraviolet and optical photometry of M82 at large. Accordingly, the dust grains in the extended foreground ISM producing the diffuse echo ring are similar in size to those in the Milky Way. Extinction in the luminous arc, however, favors a smaller R_V value, similar to the extinction law deduced from the SN itself, represented by $R_V \sim 1.4$. This similarity indicates that the grain size distribution in the slab of ISM producing the luminous arc is similar to the ISM responsible for the extinction measured towards the SN at early epochs.

The optical depth due to light scattered by the ISM can be estimated as follows. If they have similar properties as Milky Way-like dust with R_V = 3.1, τ_{F475W} ranges from 0.3 at PA 225° - 270°, covering part of the diffuse ring, to 0.9 at PA 45° - 90°, where the luminous arc is brightest. These optical depths are smaller than that along the DLOS. One possible explanation for the discrepancy can be an overestimate of the degree of forward scattering. At +277 d, the scattering angle is $\sim 2.6°$ for the luminous arc-producing dust. A dramatic increase in forward scattering occurs with increasing grain size while smaller grains scatter light more isotropically, leading to a smaller value of the phase function, see Chapter 5 of van de Hulst (1957). Therefore, to produce a light echo of the same strength, smaller dust grains in the ISM responsible for the luminous arc require a higher optical depth than larger Milky Way-like dust grains do.

To illustrate the dependence of the degree of forward scattering on the optical depth, we investigate the Heyney-Greenstein phase function characterizing the angular distribution of scattered light intensity as shown by Equation 2.3. Figure 2.13 demonstrates the fraction of scattered light at small scattering angle, i.e., $2°.6$ as a function of scattering asymmetry factor, g. In this figure, values of $g = 0.439$ and $g = 0.345$ are indicated for astronomical silicate and graphite grains with radius of 0.1 micron according to calculations based on Draine & Lee (1984) and Laor & Draine (1993).

When the grains are significantly smaller than the wavelength of light, the classical Rayleigh scattering limit is reached. The asymmetry factor for Rayleigh scattering is $g = 0$, and the phase function becomes unity, indicating no directional preference of scattering. This is the case for the luminous arc while the phase function has a value of 7.8 for Milky-Way dust with R_V = 3.1. This means that the optical depth calculated for the case of Rayleigh scattering is 7.8 times larger than for Milky-Way dust with R_V = 3.1. The densest part of the scattering material will attain a value of $\sim$ 7.0 in $F475W$, significantly larger than the optical depth measured along the DLOS. On the other hand,

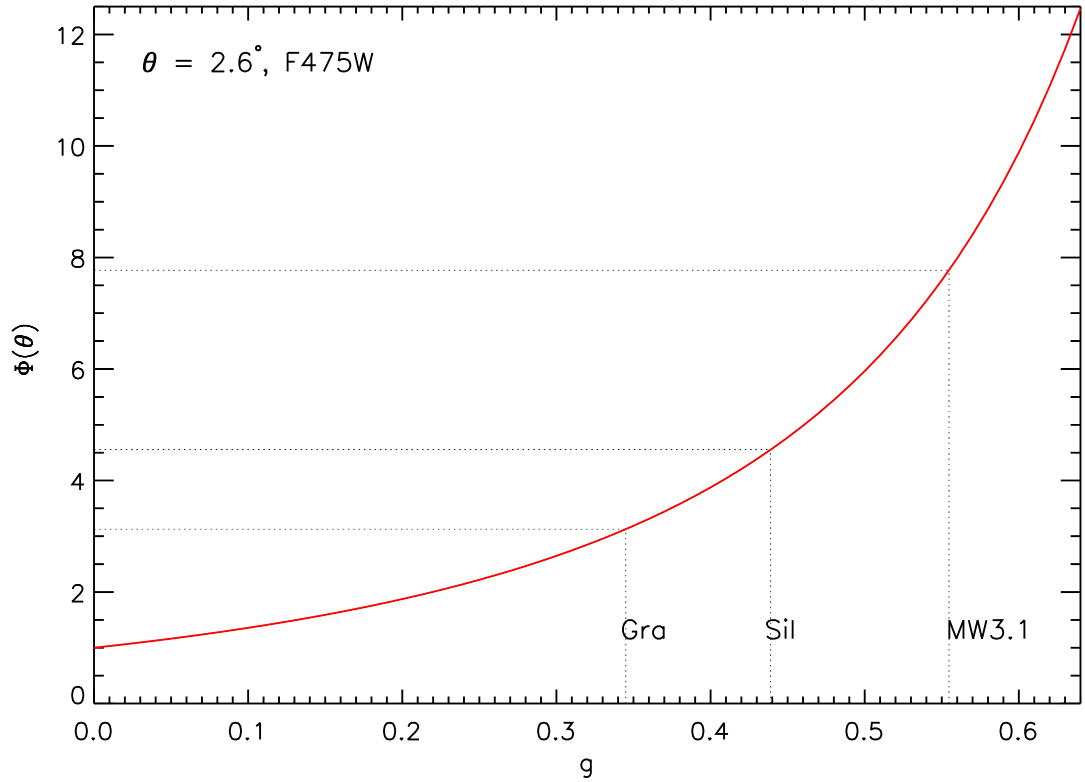

Figure 2.13 Fraction of light scattered at the small angle of $2.6°$ as a function of the value of the phase scattering function, g, as calculated from Equation 2.3. MW3.1, Gra, and Sil represent the g factors for Milky-Way dust with $R_V = 3.1$, graphite spheres with radius 0.1 μm, and "astronomical silicate" spheres with radius 0.1 μm.

for larger grains the asymmetry factor g approaches unity, and the efficiency of forward scattering increases substantially.

The grain size distribution in the extinction-producing material towards SN 2014J itself is similar to that of the luminous arc-producing material, as inferred from the similarity of R_V found in both of the two ISM components. Considering this low R_V and the lower optical depth found in the scattering material responsible for the luminous arc, we infer that these scattering materials are also responsible for the extinction towards SN 2014J. Our result is consistent with the relationship between the host galaxy extinction A_V and their measured R_V (Mandel et al., 2011), which for SNe with low extinction, $A_V \lesssim 0.4$, $R_V \approx 2.5 - 2.9$ is favored, while at high extinction, $A_V \gtrsim 1$, low values of $R_V < 2$ are favored. Due to the lack of knowledge about the detailed distribution and optical properties of the dust in M82, we cannot rule out the possibility that the different extinctions along the scattering line of sight of the materials and the DLOS may partly also be caused by a denser ISM along the DLOS. The extinction along the DLOS may also be due to dust at small foreground distances which would produce light echoes too close to the SN to be detected. Additionally, it is possible that the extinction can be generated by interstellar dust clouds placed too far in front of the SN. Recall Equations 2.7 and 2.8, the luminosity of the light echo resulting from a dust slab intersecting the DLOS decreases as $1/r$ (where r is the distance between the SN and the dust slab). Considering numerous Na, Ca, and K features have been seen along the DLOS (Patat et al., 2015), we cannot rule out the possibility that there are dust clouds placed more than 500 pc away from the SN and can hardly be detected in current images.

The smaller grains found in the dense dust slab seem to be inconsistent with the grain size distribution in dense regions inferred by Cardelli et al. (1989) and Whittet et al. (1992), who offered the qualitative explanation that coagulation inside the dense interstellar dust clouds removes the smaller particles and results in higher R_V. It is possible that the dense dust slab and the porous diffuse dust cloud belong to different components of the ISM, which are formed by different mechanisms and at significantly different episodes of the history of M82. For instance, considering the possibility that the dense dust slab that produced the luminous arc echo was formed more recently, i.e., around an episode of intense star formation at $\sim$60 Myr ago (Gallagher & Smith, 1999), the size growth may not be significant in the dense dust slab considering the relatively long time of the grain growth, i.e., see Figure 8 of Mattsson (2016).

The presented light-echo model is necessarily only a simplified approximation of reality. Our model attempts to reproduce the optical depth of the scattering material over a projected area of $\sim$ 40 pc $\times$ 40 pc in the plane of the sky, and compares it to the optical depth measured for the DLOS. One major source of uncertainty is the assumption of single scattering (Wood et al., 1996; Patat, 2005). In view of the large extinction measured towards SN 2014J, a Monte Carlo simulation with various grain size distributions should give a better representation of the real scattering process. Another uncertainty results from the usage of the extinction measured along the DLOS around maximum light also for the echo-producing material. Additionally, the assumption of Galactic R_V values may not be realistic for M82.

2.5 Summary

The geometric and photometric evolution of resolved light echoes around SN 2014J was monitored with *HST*. Two main constituents were found. From a luminous arc, a discrete slab of dust was inferred at a foreground distance of 228$\pm$7pc. In addition, a resolved, diffuse ring-like light echo implies that another foreground ISM component is widely distributed over distances of $\sim$ 100-500 pc. If the scattering material suffers the same extinction as along the DLOS, the densest part has a number density of $\sim$ 1.5 $\times 10^{21}$ cm^{-2}, based on a single-scattering-plus-attenuation approach. The scattering material is unevenly distributed with PA. The wavelength dependence of the scattering optical depth is steeper in the luminous arc than in the diffuse ring. The former favors a small $R_V \sim 1.4$ as also measured along the DLOS, and the latter is more consistent with a ’normal’ $R_V \sim 3$. This suggests that the average grain size is smaller in the ISM responsible for the luminous arc, and the more widely distributed scattering materials have average properties similar to Milky Way-like dust. This study reveals the R_V fluctuation of the extragalatic dust on parsec scales. We deduce that systematically steeper extinction laws towards Type Ia SNe do not have to represent the average behaviour of the extinction law in the host galaxy.

The optical depth of the scattering material estimated from the scattering properties of Milky-Way-like dust with $R_V = 3.1$ is smaller than the optical depth measured along the DLOS. The optical depth along the DLOS is better reproduced with smaller grains as also indicated for the dust slab responsible for the luminous arc. This suggests that an extension of this dust slab, or a separate cloud with similar properties, is also responsible for the extinction towards SN 2014J. More data will be collected in future observing campaigns that will help additionally characterize the extinction laws measured within different light echo components. Further constraints on the amount and properties of the circumstellar and interstellar material from polarimetry and very late-time photometry will be discussed in future work.

Acknowledgement

We are grateful to Peter Lundqvist and Anders Nyholm for providing the late-time spectrum of SN 2014J. We also thank Jian Gao, Bi-wei Jiang, Kevin Krisciunas, Armin Rest, and Nicholas Suntzeff for helpful discussions. The supernova research by Y. Yang, P. J. Brown, and L. Wang is supported by NSF grant AST-0708873. P. J. Brown was partially supported by a Mitchell Postdoctoral Fellowship. Y. Yang and M. Cracraft also acknowledge support from NASA/STScI through grant HST-GO-13717.001-A. L. Wang is supported by the Strategic Priority Research Program "The Emergence of Cosmological Structures" of the Chinese Academy of Sciences, Grant No. XDB09000000. L. Wang and X. Wang are supported by the Major State Basic Research Development Program (2013CB834903), and X. Wang is also supported by the National Natural Science Foundation of China (NSFC grants 11178003 and 11325313).

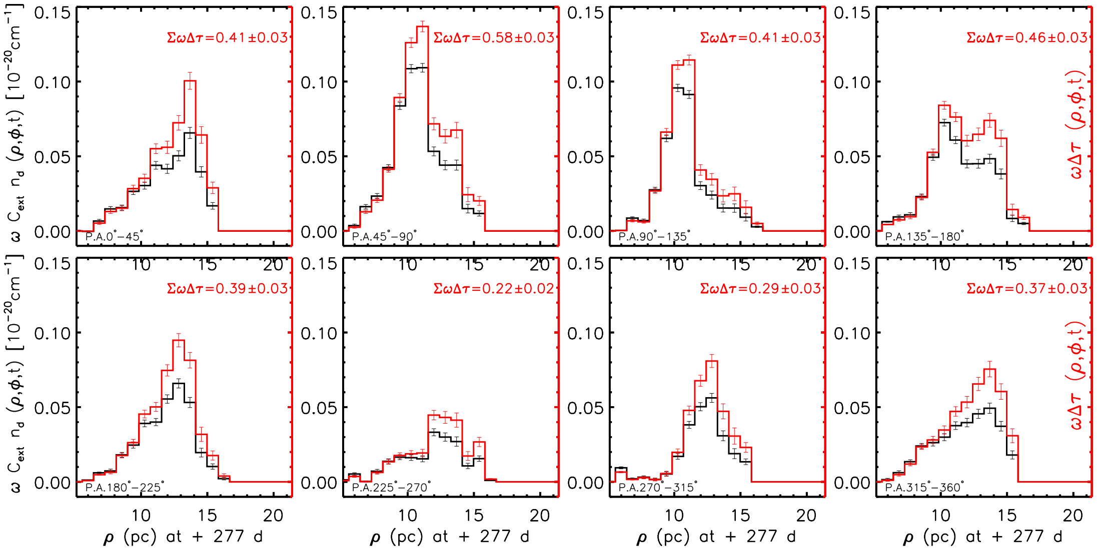

Figure 2.14 Radial profiles at all eight PAs (as labeled) of optical properties of the scattering material. The calculations are based on the density map (transformed from the residual image) in passband $F475W$ on +277 d. Black histograms represent $\omega C_{ext} n_d(\rho, \phi, t)$ in units of $10^{-20} cm^{-1}$ as shown on the left ordinate and can be used to infer the volume densities. Red histograms represent the unitless $\omega C_{ext} n_d dz = \omega\tau$ and share the same tick marks as the left ordinate, which can be used to infer the column number densities. τ is the optical depth of the dust mapped onto a single pixel.

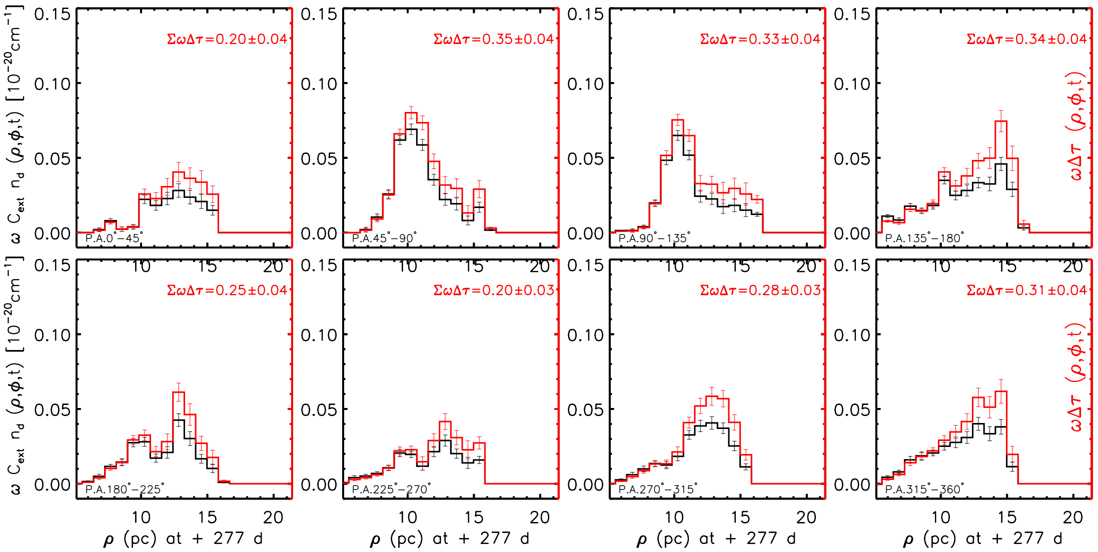

Figure 2.15 Same as Figure 2.14 except for $F606W$.

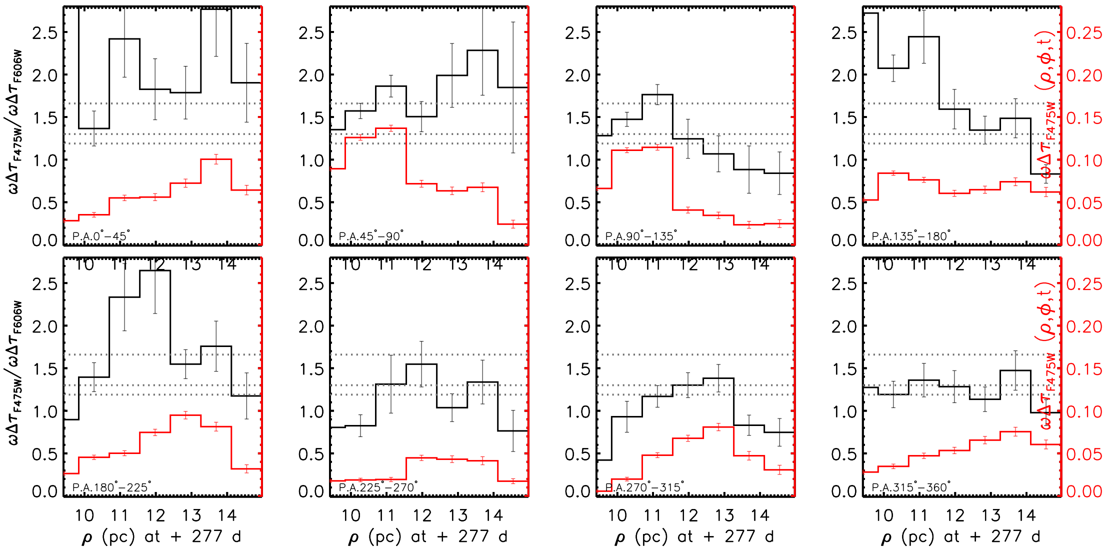

Figure 2.16 Radial run of the wavelength dependence of the scattering material characterized by τ_{F606W} on +277 d. The abscissa measures the physical distances (in pc) in the plane of the sky. Each panel shows a different bin in position angle of width $45°$ (as labeled). The upper, middle, and lower horizontal dashed lines represent the values calculated for Milky-Way dust with R_V = 1.4, 3.1, and 5.5, respectively. The luminous arc in PA bins from 45° to 180° appear at ρ = 10∼11 pc and $\omega\tau_{F475W}/\omega\tau_{F606W}$ ∼1.7. Diffuse structures at large PAs expose a different wavelength dependence on scattering because $\omega\tau_{F475W}/\omega\tau_{F606W} \sim 1.3$.

3. MAPPING CIRCUMSTELLAR MATTER WITH POLARIZED LIGHT – THE CASE OF SUPERNOVA 2014J

3.1 Introduction

The explosion of type Ia supernovae (SNe) is powered by the thermonuclear runaway of ($\sim 1 M_{\odot}$) carbon/oxygen white dwarfs (C/O WDs, Hoyle & Fowler, 1960). The homogeneity of type Ia SNe lightcurves (i.e., Barbon et al., 1973; Elias et al., 1981), and the correlation between the decline rate of the light curve and the luminosity at peak (Phillips, 1993) allows people using type Ia SNe as the most accurate distance indicators at redshifts out to $\sim$2 (Riess et al., 1998; Perlmutter et al., 1999; Riess et al., 2016). However, the exact progenitor systems of type Ia SN explosions remain unknown.

A few pieces of evidence suggest a non-degenerate companion scenario in which a compact WD accretes matters from a subgiant or a main sequence star. Examples include the time evolution of Na D_2 features after the $B-$band maximum light of SN 2006X (Patat et al., 2007) and the UV flash within $\sim$5 days after the explosion of iPTF14atg (Cao et al., 2015). However, other observations favors a double degenerate scenario featuring the merger of two WDs (Iben & Tutukov, 1984; Webbink, 1984), see, for example, SN 2011fe Bloom et al., 2012). For the first few days after the explosion, collision between material ejected by the SN and a non-degenrate companion star would produce longer lasting excess in optical/UV emission than the luminosity solely powered by the radioactive decay (Kasen, 2010). In particular, Kepler satellite monitoring of three normal type Ia SNe during their entire rising phase (Olling et al., 2015) shows no evidence of interaction between SN ejecta and circumstellar matter (CSM) or companion stars. The absence of CSM around type Ia SNe supports double degenerate progenitor models; however, searches for CSM around type Ia SNe has been difficult and is in most cases inconclusive.

The merger of two compact stars is a very asymmetric process, which should lead to a strong polarimetric signature. By contrast, observations consistently find a lack of intrinsic polarization before optical maximum (Wang & Wheeler, 2008; Maund et al., 2013), which seems to cast doubts on the double degenerate scenario (Wang & Wheeler, 2008; Rimoldi et al., 2016). Quantifying the amount of CSM is of critical importance for understanding the progenitor system of type Ia SNe and for the extinction correction in using type Ia SNe as standard candles.

Another major uncertainty in type Ia SN cosmology is the correction for interstellar extinction. Better estimation of interstellar extinction reduces systematic uncertainties. Characterization of dust in the diffuse interstellar medium (ISM) relies heavily on the observed wavelength dependence of extinction and polarization (Patat et al., 2015; Voshchinnikov et al., 2012). The observed wavelength dependence of interstellar extinction R_V contains information on both the size and composition of the grains. The value of $R_V = 3.1$ (Cardelli et al., 1989) has often been considered the Galactic standard, but with a range from 2.2 to 5.8 (Fitzpatrick, 1999) for different lines of sight. There is increasing evidence that extinction curves towards type Ia SNe systematically favor a steeper law ($R_V < 3$, see, i.e., Nobili & Goobar, 2008, and Cikota et al., 2016 for a summary of R_V results of earlier studies). This discrepancy has remained unexplained. It is of critical importance to understand whether the systematically low R_V values towards type Ia SNe are caused by (1) systematic differences from the optical properties of Galactic dust grains, or (2) modifications by CSM scattering.

Several authors have proposed that circumstellar dust scattering may be a solution to the surprisingly low R_V values towards type Ia SNe (Goobar, 2008; Patat et al., 2006; Wang, 2005). The effect on R_V and the light curve shape, however, also depends on the geometrical configuration and dust grain properties (Amanullah & Goobar, 2011; Brown et al., 2015). For example, recent observations of the highly reddened SN 2014J in M82 have found no convincing evidence of the presence of circumstellar dust (Patat et al., 2015; Brown et al., 2015; Johansson et al., 2017, see, however, Foley et al., 2014; Hoang, 2017).

Observations of polarized light and its time evolution can be an effective way of studying the CSM. Type Ia SNe have low polarization in broad-band observations ($\lesssim 0.2\%$, Wang & Wheeler, 2008), whereas the scattered light from CSM can be highly polarized. Light scattered at large angles can be polarized at $\sim 50\%$. For a spatially unresolved source, the scattered light can contribute significantly to the total integrated light and the polarization of the integrated light can evolve rapidly with time after the SN evolves past optical maximum (Wang & Wheeler, 1996). The fraction of polarized flux from any not axisymmetric circumstellar dust increases substantially as the SN dims and scattered photons (often from light at optical maximum) dominate the SN light curve at late phases. The actual situation may be more complicated as the dust distribution can be more uniform around the SN than the often assumed single clump. Then, the effect on the polarization and the light curve may be less dramatic. In general, the effect is qualitatively stronger in the blue than in the red due to the higher scattering opacity in the blue. For instance, at about 200-400 days past optical maximum, right-angle scattering of SN light by circumstellar dust located on the plane of the sky at distances of around 200 - 400 light days (5.2×10^{17} - 1.0×10^{18} cm) from the SN becomes observable.

SN 2014J was discovered on Jan. 21.805 UT (Fossey et al., 2014; Ma et al., 2014), and the first light has been constrained to be Jan. 14.75 UT (Zheng et al., 2014; Goobar et al., 2015). SN 2014J reached its B-band maximum at Feb. 2.0 UT (JD 2,456,690.5) at a magnitude of 11.85 ± 0.02 (Foley et al., 2014). Exploding in the nearby starburst galaxy M82 at a distance of 3.53 ± 0.04 Mpc (Dalcanton et al., 2009), SN 2014J was the nearest SN since SN 1987A. The relative proximity of SN 2014J allows continuous photometric and spectroscopic observations through late phases (Lundqvist et al., 2015; Bonanos & Boumis, 2016; Porter et al., 2016; Sand et al., 2016; Srivastav et al., 2016; Johansson et al., 2017; Yang et al., 2017b). SN 2014J suffers from heavy extinction and is located behind a large amount of interstellar dust (Amanullah et al., 2014). So far, there is ample evidence that the strong extinction is caused primarily by interstellar dust (Patat et al., 2015; Brown et al., 2015). However, high resolution spectroscopy does show strong evidence of time evolving KI lines that can be understood as due to photo ionization of materials located at a distance of about 10^{19} cm from the SN (Graham et al., 2015b). No positive detection of any material at distances within 10^{19} cm has been reported for SN 2014J, despite a controversial claim of possible contributions of circumstellar dust to the total extinction based on UV data (Foley et al., 2014; Brown et al., 2015; Bulla et al., 2016). In this paper, we present our late-time *HST* imaging polarimetry of SN 2014J and derive from it the amount of circumstellar dust around SN 2014J.

3.2 Observations and Data Reduction

The *HST* WFC/ACS camera has a polarimetry mode which allows for accurate imaging polarimetry. The filter-polarizer combinations selected by us have recently been calibrated (Avila, 2017). We used the Advanced Camera for Surveys/Wide Field Channel (ACS/WFC) on board the *HST* to observe SN 2014J in imaging polarization mode on six epochs (V1-V6) under multiple *HST* programs: GO-13717 (PI: Wang), GO-14139 (PI: Wang), and GO-14663 (PI: Wang). The observations were taken with three different filters: $F475W$ (SDSS g), $F606W$ (broad V), and $F775W$ (SDSS i), each combined with one of the three polarizing filters (POL*V): POL0V, POL60V, and POL120V. These polarizers are oriented at relative position angles of $0°$, $60°$, and $120°$. A log of observations is presented in Table 3.1. Multiple dithered exposures were taken at each observing configuration to allow for drizzling of the images. Except for the first epoch with filter $F775W$, the observations were taken with two 30s exposures in POLV0V, and only single 55s exposures for POL60V and POL120V.

Table 3.1 Log of polarimetric observations of SN 2014J with *HST* ACS/WFC POLV

Filter	Polarizer	Date (UT)	Exp (s)	Phase^a Days	Date (UT)	Exp (s)	Phase^a (Days)	Date (UT)	Exp (s)	Phase^a (Days)
F475W	POL0V	2014-11-06	3×130	276.5	2015-03-25	3×400	415.6	2015-11-12	4×1040	648.5
F475W	POL120V	2014-11-06	3×130	276.5	2015-03-25	3×400	415.6	2015-11-12	4×1040	648.7
F475W	POL60V	2014-11-06	3×130	276.5	2015-03-25	3×400	415.7	2015-11-12	4×1040	648.8
F606W	POL0V	2014-11-06	2×40	276.6	2015-03-27	3×60	417.9	2015-11-12	4×311	649.0
F606W	POL120V	2014-11-06	2×40	276.6	2015-03-27	3×60	418.0	2015-11-13	4×311	649.0
F606W	POL60V	2014-11-06	2×40	276.6	2015-03-27	3×60	418.0	2015-11-13	4×311	649.1
F775W	POL0V	2014-11-06	2×30	276.6	2015-03-27	3×20	418.0	2015-11-12	4×100	648.5
F775W	POL120V	2014-11-06	1×55	276.6	2015-03-27	3×20	418.0	2015-11-12	4×100	648.7
F775W	POL60V	2014-11-06	1×55	276.6	2015-03-27	3×20	418.0	2015-11-12	4×100	648.9
F475W	POL0V	2016-04-08	4×1040	796.2	2016-10-12	4×1040	983.1	2017-04-28	4×1040	1181.3
F475W	POL120V	2016-04-08	4×1040	796.4	2016-10-12	4×1040	983.3	2017-04-28	4×1040	1181.4
F475W	POL60V	2016-04-08	4×1040	796.6	2016-10-12	4×1040	983.4	2017-04-28	4×1040	1181.5
F606W	POL0V	2016-04-08	4×311	796.8	2016-10-14	3×360	985.1	2017-04-28	3×360	1181.7
F606W	POL120V	2016-04-08	4×311	796.8	2016-10-14	3×360	985.1	2017-04-28	3×360	1181.7
F606W	POL60V	2016-04-08	4×311	796.9	2016-10-14	3×360	985.1	2017-04-28	3×360	1181.7
F775W	POL0V	2016-04-08	4×100	796.2	2016-10-12	4×202	983.1	2017-04-28	4×202	1181.3
F775W	POL120V	2016-04-08	4×100	796.4	2016-10-12	4×202	983.3	2017-04-28	4×202	1181.4
F775W	POL60V	2016-04-08	4×100	796.6	2016-10-12	4×202	983.4	2017-04-28	4×202	1181.5

[a] Days since B maximum on 2014 Feb. 2.0 (JD 245 6690.5).

The *HST* data were reduced following the usual routine of drizzling whenever possible to remove sensitivity to artifacts and cosmic rays. For each bandpass, one image at each polarizer has been obtained. Bright HII regions in the field-of-view (FOV) were used to align exposures in different bandpass+polarizer combinations and epochs through *Tweakreg* in the *Astrodrizzle* package (Gonzaga et al., 2012). Large scale distortions caused by a weak lens which corrects the optical focus of the polarizing filters have been removed by the *Astrodrizzle* software. All images were aligned to better than 0.25 pixels in both x and y directions. This is in agreement with the small scale distortion (±0.3 pixel) in the images caused by slight ripples in the polarizing material (see the ACS Data Handbook, Lucas, 2016).

The absolute throughput values of bandpass+polarizer combinations listed in the *Synphot* software does not match those found in on-orbit calibrations. Correction factors by Cracraft & Sparks (2007) based on on-orbit calibration programs were used to remove the instrumental polarization. The scaling factors (C_{POL*V}) have been applied to images

---

http://www.stsci.edu/institute/software_hardware/stsdas/synphot obtained with each polarizer: $r(POL*V) = C_{POL*V} * Im(obs)_{POLV}$. The remaining instrumental polarization can still be as much as ~1%, and discrepant instrumental polarization has been observed at different roll angles (i.e., see Cracraft & Sparks, 2007 and Lucas, 2016). To improve the measuring precision, we use for observations from V1 and V2 bright sources in the FOV to monitor the stability of the instrumental polarization. The roll angles in the subsequent observing epochs were set to be equal or to 180° different from the roll angles in V1 and V2. We discuss this further in Section 3.3.

3.2.1 Measuring the degree of polarization

We deduced the Stokes vectors (I,Q,U) from the observations as follows:

$$\begin{aligned} I &= \frac{2}{3}[r(POL0) + r(POL60) + r(POL120)], \\ Q &= \frac{2}{3}[2r(POL0) - r(POL60) - r(POL120)], \\ U &= \frac{2}{\sqrt{3}}[r(POL60) - r(POL120)], \end{aligned} \tag{3.1}$$

Flux measurements were made with a circular aperture of 0″.15 (3 pixels in the ACS/WFC FOV) to reduce the contamination from the extremely non-uniform background. Aperture corrections were calculated with the ACS/WFC encircled energy profile for each bandpass according to Sirianni et al. (2005). We perform the measurements of the SN on the images obtained by each polarizer $r(POL*V)$. We also deduce the Stokes I, Q, U maps using Equation 3.1, integrating within the aperture centered at the SN on the deduced Stokes I, Q, U maps. In both cases, the background has been estimated by choosing the same inner and outer radii as Yang et al. (2017b). The two approaches agree within the uncertainties when the signal-to-noise (S/N) ratio on each $r(POL*V)$ of the SN >50. Figure 3.1 presents a color composite image of SN 2014J consisting of the Stokes I data for each bandpass and epoch. The images show resolved light echoes expanding over time, which

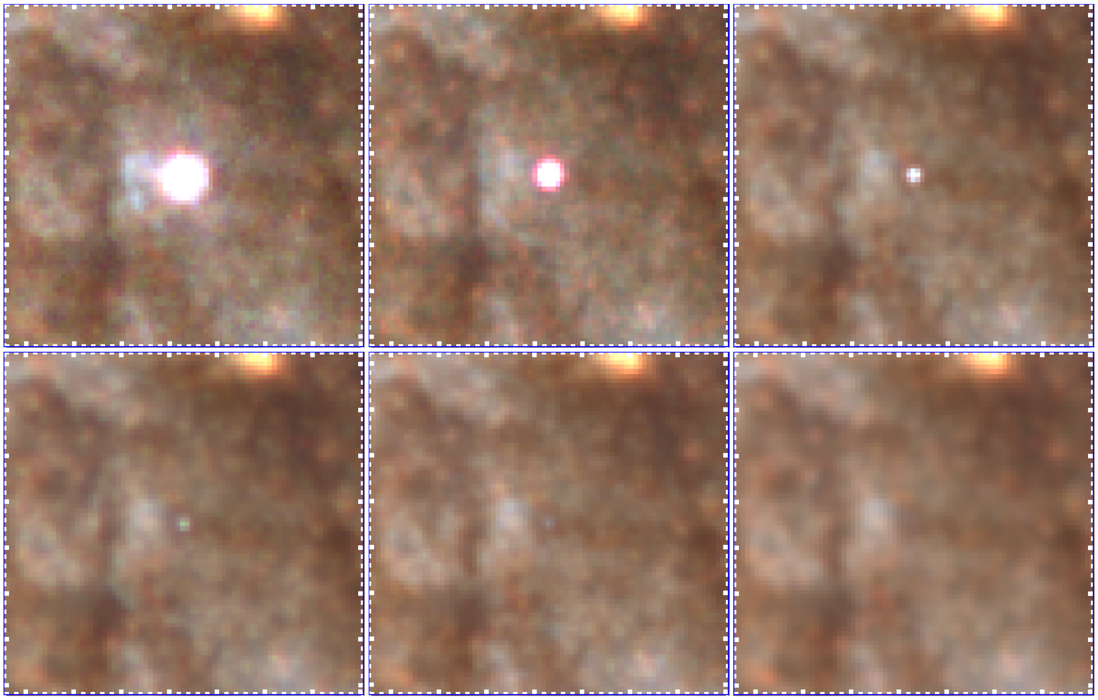

Figure 3.1 Color images of SN 2014J from *HST* ACS/WFC $F475W$, $F606W$, and $F775W$ observations on days 277 (upper left), 416 (upper middle), 649 (upper right), 796 (lower left), 985 (lower middle), and 1181 (lower right) after maximum light. North is up, east is left, and the distance between big tick marks corresponds to $0''.5$ and 8.6 pc projected on the plane of the sky. Reflection of SN light by the dust between the SN and the observer creates arcs of light echoes which are propagating with time. There may also be unresolved light echoes at distances so close to the central SN that even the *HST* cannot resolve. But imaging polarimetry can still detect their presence.

have been first identified by Crotts (2015). We only remark here that these multiple light echoes are produced by dust clouds at a distance about 100 pc to 500 pc away from the SN 2014J. The dust is unlikely to be related to the SN progenitor evolution. Detailed studies of these resolved light echoes were performed in the same *HST* data as those used for the study and can be found in Yang et al. (2017a).

The degree of polarization and the polarization position angle can be derived as:

$$p\% = \frac{\sqrt{Q^2+U^2}}{I} \times \frac{T_{par}+T_{perp}}{T_{par}-T_{perp}} \times 100\% \qquad (3.2)$$

$$P.A. = \frac{1}{2}\tan^{-1}\left(\frac{U}{Q}\right) + PA\_V3 + \chi \tag{3.3}$$

The SN fluxes measured in the different 'bandpass+polarizer' combinations were then converted to polarization measurements following the *HST* ACS manual (Avila, 2017) and earlier work (Sparks & Axon, 1999). The cross-polarization leakage is insignificant for visual polarizers (Biretta et al., 2004). The factor containing the parallel and perpendicular transmission coefficients $(T_{par} + T_{perp})/(T_{par} - T_{perp})$ is about unity and has been corrected in our data reduction. The degree of polarization (p$\%$) is calculated using the Stokes vectors. These corrections together with the calibration of the source count rates vectorially remove the instrumental polarization of the WFC ($\sim 1\%$). The polarization position angle (PA) is calculated using the Stokes vectors and the roll angle of the *HST* spacecraft (PA_V3 in the data headers) as shown in Equation 3.3. Another parameter, called χ, containing information about the camera geometry which is derived from the design specification, has been considered when solving the matrix to deduce the Stokes vectors. For the WFC, $\chi = -38^{\circ}.3$ (Lucas, 2016).

3.2.2 Errors in polarimetry

The classical method proposed by Serkowski (1958, 1962) is often used for the determination of the polarization and associated uncertainties. Montier et al. (2015) investigated the statistical behavior of basic polarization fraction and angle measurements. We use Equation 3.4 and 3.5 to describe the uncertainty of $p\%$ and P.A. The detailed derivation is available in Appendix F of Montier et al. (2015).

$$\sigma_p^2 \;=\; \frac{1}{p^2 I^4} \times \left(Q^2\sigma_Q^2 + U^2\sigma_U^2 + p^4 I^2 \sigma_I^2 + 2QU\sigma_{QU} - 2IQp^2\sigma_{IQ} - 2IUp^2\sigma_{IU}^2\right) \tag{3.4}$$

$$\sigma_{P.A} \;=\; \sqrt{\frac{Q^2\sigma_U^2 + U^2\sigma_Q^2 - 2QU\sigma_{QU}}{Q^2\sigma_Q^2 + U^2\sigma_U^2 + 2QU\sigma_{QU}}} \times \frac{\sigma_p}{2p}\, rad \tag{3.5}$$

Table 3.2 The polarization Degree of SN 2014J

Filter	Phase	p	PA	mag	Phase	p	PA	mag
	Days	%	degrees		Days	%	degrees	
$F475W$	276.5	3.82±0.12	40.3±0.9	17.363±0.001	415.6	4.56±0.21	37.7±1.2	19.464±0.002
$F606W$	276.6	2.65±0.21	46.9±2.3	17.429±0.002	417.9	3.27±0.48	43.4±3.5	19.594±0.003
$F775W$	276.6	1.19±0.24	41.7±7.5	16.742±0.002	418.0	1.55±0.58	17.1±6.2	18.268±0.004
$F475W$	648.5	4.68±0.44	33.3±2.6	22.363±0.003	796.2	3.50±0.81	33.0±6.6	23.266±0.006
$F606W$	649.0	4.57±0.58	47.7±3.7	21.962±0.005	796.8	0.78±1.19	73.2±43.6	22.917±0.009
$F775W$	648.5	4.49±0.75	39.9±4.8	21.427±0.006	796.2	2.40±1.48	54.1±17.5	22.492±0.011
$F475W$	983.1	2.27±1.84	48.3±23.6	24.169±0.014	1181.4	5.61±2.76	59.2±16.0	24.765±0.023
$F606W$	985.1	6.58±3.09	53.5±13.9	23.934±0.024	1181.7	3.12±5.88	37.4±53.2	24.695±0.049
$F775W$	983.1	8.43±1.99	68.3±6.8	23.294±0.015	1181.4	7.61±4.19	104.6±15.5	24.234±0.032

The Stokes I vector gives the total intensity of the source. The AB magnitudes of the SN were obtained by applying the ACS/WFC zeropoints.

The degree of polarization and the magnitudes of the SN in different filter bands are shown in Table 3.2. The other sources of data used in this paper include three epochs of observations using the Calar Alto Faint Object Spectrograph (CAFOS, Patat et al., 2015), mounted at the 2.2 m telescope in Calar Alto, Spain (Patat & Taubenberger, 2011). The spectropolarimetry used the low-resolution B200 grism coupled with a $1''.5$ slit, giving a spectral range 3300-8900 angstrom, a dispersion of $\sim$ 4.7 angstrom/pix, and a full width half maximum (FWHM) resolution of 21.0 angstrom. Spectropolarimetry on Jan 28 (day -6) and Mar 08 (day 33) 2014 have been obtained through private communication. The data from Feb 03 (day 0) 2014 were already used by Patat et al. (2015). We also used broad-band polarimetry taken with the Hiroshima One-shot Wide-field Polarimeter (HOWPol, Kawabata et al., 2008) around optical maximum as published by Kawabata et al. (2014).

3.3 Analysis

Figure 3.2 presents the wavelength dependence and time evolution of the new *HST* data points together with ground-based polarimetry. The *HST* data can be compared to ground-based polarimetry acquired around optical maximum to study the temporal evolution of the polarization. Broad-band polarimetric observations of SN 2014J taken on Jan

22.4 (-11 days relative to B-band maximum), Jan 27.7 (-6 days), Feb 16.5 (+14 days), Feb. 25.6 (+23 days) and Mar 7.8 (+33 days) detected no variability (Kawabata et al., 2014). Spectropolarimetry on Jan 28 (-6 days), Feb 03 (+0 day), and Mar 08, 2014 (+33 days) indicates no temporal evolution either (Patat et al., 2015). The variability in ground-based data was less than 0.2%, except at the bluest end where the data were noisy but are still consistent with constancy. At the 0.2% level, the intrinsic polarization of the SN becomes significant (Wang & Wheeler, 2008). This makes it difficult to determine the contribution from circumstellar dust. We conclude that the overall high level of polarization at early times is due to interstellar dust, and that there is no detectable variability at early times down to the 0.2% level.

3.3.1 Interstellar polarizaion

So-called "Serkowski Law" provides an empirical wavelength dependence of optical/near infrared (NIR) interstellar polarization (Serkowski et al., 1975). It can be written as:

$$p(\lambda)/p_{\max} = \exp[-K \ln^2(\lambda_{\max}/\lambda)], \tag{3.6}$$

where $\lambda_{\max}$ is the wavelength of the maximum polarizarion $p(\lambda_{\max})$ and K is a parameter describing the width of the polarization peak. We fitted this relation to optical spectropolarimetry at maximum light obtained by CAFOS (Patat et al., 2015). The interstellar polarization wavelength dependence towards SN 2014J exhibits a very steep increase in the blue (Kawabata et al., 2014; Patat et al., 2015). Hence the position of the polarization peak cannot be determined due to the lack of UV data. Therefore, we employ the canonical value $K = 1.15$ according to Serkowski et al. (1975) and obtain a reasonable fit with $\lambda_{\max}$ =0.25 μm and $p(\lambda_{\max})$ =8.1%. Extrapolation of the interstellar polarization to the effective wavelengths of the $F475W$, $F606W$, and $F775W$ filters yields 4.9%, 3.3%, 1.8%, respectively.

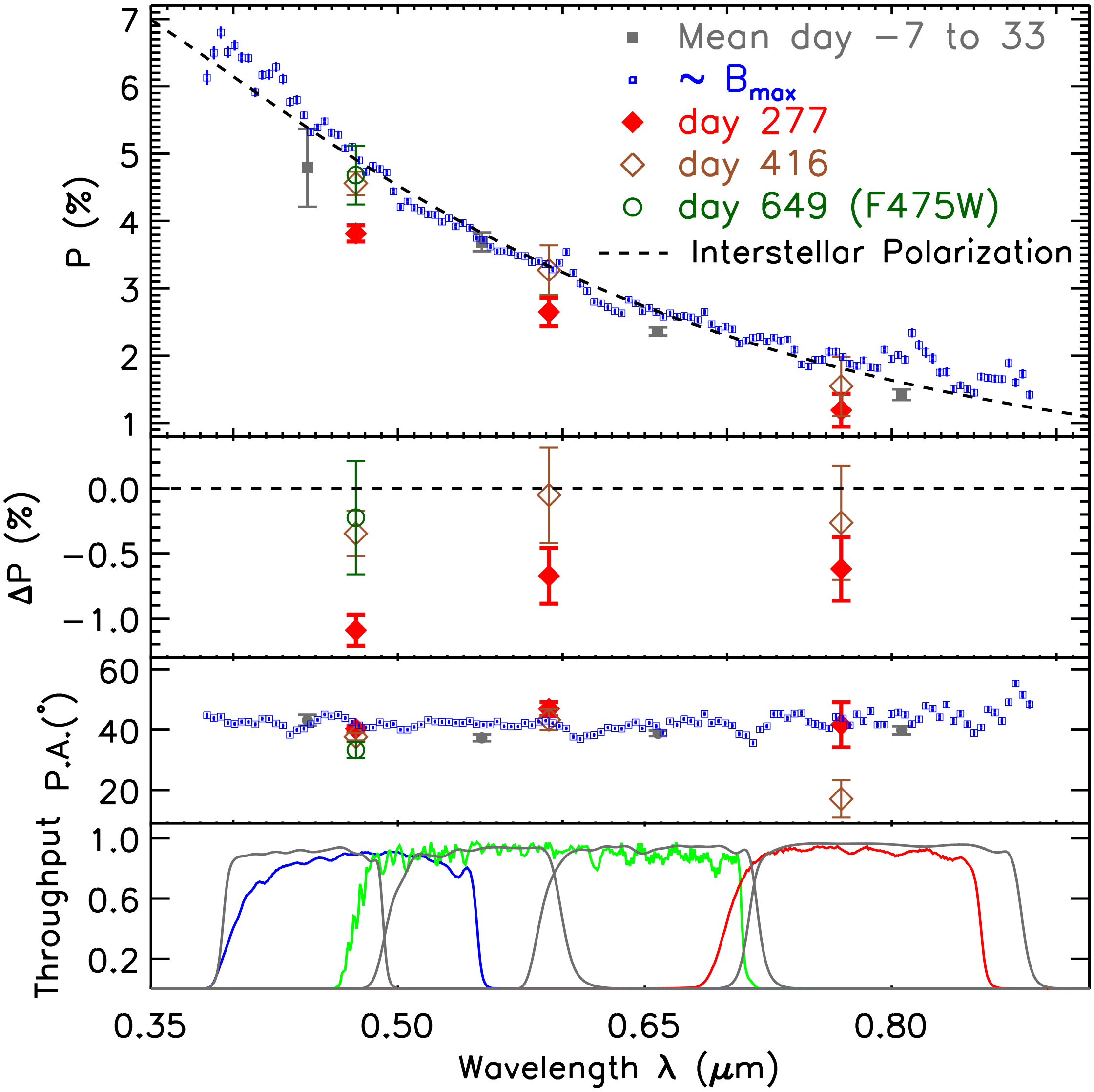

Figure 3.2 From top to bottom: the first panel presents the optical imaging polarimetry of SN 2014J taken with *HST* ACS/WFC on day 277, day 416, and day 649, compared with earlier broad-band polarization (gray, solid squares, Kawabata et al., 2014) and spectropolarimetry (blue, open squares, Patat et al., 2015). The dashed line presents the 'Serkowski law' fitting of the interstellar polarization; the second panel gives the difference between our *HST* polarimetry and the interstellar polarization; the third panel displays the corresponding polarization position angles; the bottom panel illustrates the filters transmission curve for the broad-band polarimetry (Kawabata et al., 2014) (gray lines), and the *HST* $F475W$ (blue line), broad $F606W$ (green line), and $F775W$ (red line) filter band measurements. The data around optical maximum exhibit little evolution with time and the polarization are consistent to within 0.2%. The *HST* data on day 277 shows dipicts a conspicuously different degree of polarization in all three filter bands compared to the other data sets. At later epochs, the polarization returns to the value of the maximum light.

In the *HST* data from day 277, the $F475W$ band degree of polarization has changed from 4.9% near maximum light to 3.8%. The $F475W$-band data have the highest S/N. The data in $F606W$ and $F775W$-band also show systematically different degrees of polarization. The data on day 416, however, are consistent with those from maximum light. Polarimetry at later epochs suffers from larger uncertainties as the SN fades. However, it is still broadly consistent with the interstellar polarization. Sparks & Axon (1999) fitted the errors of the polarization degree and the polarization position angle with the average S/N ratio and the degree of polarization:

$$\begin{aligned} \log_{10}(\sigma_p/p) &= -0.102 - 0.9898\log_{10}(p\langle \mathrm{S/N}\rangle_i) \\ \log_{10}\sigma_{P.A.} &= 1.415 - 1.068\log_{10}(p\langle \mathrm{S/N}\rangle_i) \end{aligned} \tag{3.7}$$

For example, exposures at each polarizer achieving $\langle \mathrm{S/N}\rangle_i \sim 500$ yield relative uncertainties σ_p/p = 3.3%, 4.9%, and 9.0% in the $F475W$, $F606W$, and $F775W$ bandpasses, respectively. For $\langle \mathrm{S/N}\rangle_i \sim 100$, the corresponding values are σ_p/p = 16%, 24%, and 44% in the $F475W$, $F606W$, and $F775W$ bandpasses, respectively. The exposure time in the $F475W$ band at later epochs was longer. The polarization position angles ($P.A.$) at all visits are broadly consistent with the average polarization position angle 42.2±0.3 deg derived around maximum light (Patat et al., 2015).

3.3.2 Polarimetry of light scattered from an SN

Differences in observed polarization can be explained with a non-uniform distribution of circumstellar dust in the vicinity of SN 2014J. Modeling the observed polarization in terms of dust scattering of SN light is usually an ill-defined problem due to the lack of knowledge about the geometric distribution of the dust and its absorption and scattering properties. A unique solution is usually very difficult to achieve. However, important constraints can be deduced based on simple and robust models.

The most efficient configuration for producing polarized light is given by a single dust clump near the location of the SN but offset from the SN on or close to the plane of the sky. In such a configuration, the light incident on the dust clump is scattered near 90° and can be polarized at the 50-100% level. The degree of polarization depends on the details of the geometry and optical depth of the dust clump. For simplicity, and without loss of much generality, the amount of scattered light can be written as the following equation:

$$L_{scat}(t) \ = \ \tau \frac{\delta\Omega}{4\pi} \Phi(\theta) \int L(t - t_e) K(t' - t_d) dt_e, \tag{3.8}$$

where t and t_e give the time after the SN maximum light and the time since SN explosion, respectively, τ is the optical depth of the dust clump, $\delta\Omega$ is the solid angle the clump subtends toward the SN, $L(t)$ is the luminosity of the SN as a function of time, t_d is the light travel time from the SN to the center of the dust clump, θ is the scattering angle, and $\Phi(\theta)$ is the scattering phase function. The function K is determined by the details of the dust distribution. It reduces to an infinitely narrow Dirac δ-function for an infinitely thin layer of dust lying on the surface of the light travel iso-delay surface (see Patat, 2005). For a more realistic distribution, K reduces to a broader function whose width characterizes the radial extent of the clump. The lack of a precise geometric model of the dust clump leads us to approximately describe the scattering properties of the clump with a Gaussian function of the form $K(t) \ = \ \frac{1}{\sqrt{2\pi}\sigma} \exp(-\frac{t^2}{2\sigma_t^2})$. Here $\sigma_t \times c$ characterizes the radial extent of the clump, and τ can be the average optical depth of the clump which is linearly related to the average column depth in the case of optical thin clump. The degree of polarization is then

$$p \ = \frac{L_{scat}(t)}{L(t) + L_{scat}(t)} p_0(\theta), \tag{3.9}$$

where p_0 is the polarization of light scattered with scattering angle θ. We adopt the Mie scattering (Mie, 1976) model for dust particles of radius a=0.1 μm size, comparable to that of the wavelength of the filter bands. The scattering phase functions and optical properties of dust particles were calculated using the OMLC Mie Scattering Calculator .

The expected amount of scattered light is given by Equation 3.10. The lack of knowledge of the geometric size of the clump makes it reasonable to assume that the scattering kernel is a function of the geometric width of the clump. For a single clump and a Dirac δ function kernel, we found the following constraints on the dust mass:

$$\delta M_{gr} \geq 1.41{\times}10^{-7} M_{\odot} \frac{p}{1\%} \left[\frac{L(0)/L(t_d)}{1.0E-04}\right] \left[\frac{r/(1-cos(\theta))}{1\ l.y.}\right]^2 \frac{\rho_{gr}}{2.5 g/cm^3} \frac{a}{0.1\mu m} \frac{1}{\Phi(\theta)} \frac{1}{\Theta(\theta)}, \tag{3.10}$$

where p is the observed amount of polarization evolution, $r = ct_d$ is the distance of the clump to the SN, θ is the scattering angle with respect to the line of sight, ρ_{gr} is the physical density of grains, a is the radius of the grain, $\Phi(\theta)$ and $\Theta(\theta)$ give the scattering phase function and the polarization degrees at scattering angle θ, respectively.

The above model was applied to the observed data to deduce the amount of dust needed to produce the observed polarization at day 277. The results for Mie scattering by smoothed UV astronomical silicate are shown in Figure 3.3 for all the three bands (Draine & Lee, 1984; Laor & Draine, 1993; Weingartner & Draine, 2001). Based on our measurement of $F475W$ with the highest S/N ratio, a minimum mass of silicate dust of $2.4 \times 10^{-6} M_{\odot}$ is needed to reproduce the observed polarization evolution, at a scattering angle of 114° with respect to the line of sight. We also considered the case of graphite and Milky Way dust, which yield minimal dust mass of $(3.6 \pm 0.4) \times 10^{-6} M_{\odot}$ and $(3.2 \pm 0.4) \times 10^{-5} M_{\odot}$, respectively. Table 3.3 summarizes the amount of dust inferred from the difference in the polarization degree between days 277 and 416. Figure 3.4 provides a schematic view of the single dust clump model which explains the time-dependent

---

http://omlc.org/calc/mie_calc.html

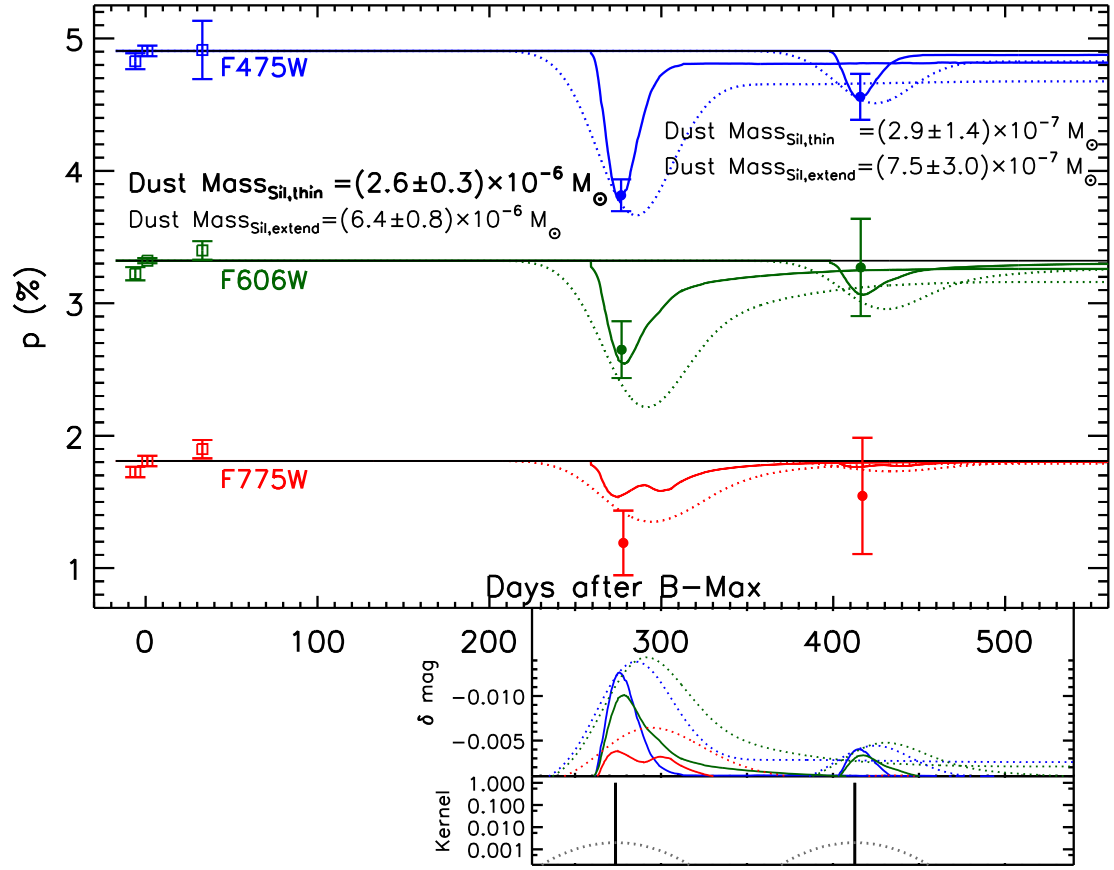

Figure 3.3 Single dust clump models of the late-time polarimetry of SN 2014J. In the upper panel, the blue, green, and red lines are for $F475W$, $F606W$, and $F775W$-band data, respectively. The solid straight lines in each color indicate the average polarimetry around optical maximum (Patat et al., 2015) in each filters. The solid lines represent the models for an infinitely-thin dust distribution, and the dashed lines illustrate the models for a radially extended dust clump approximated by a Gaussian function with $\sigma = 20$ light days. The upper inset panel shows the expected contribution to the integrated light curves by the hypothetical dust clump which can account for the observed polarization evolution. The bottom inset describes the infinitely thin (Dirac δ-function) and the Gaussian dust kernels.

polarization of SN 2014J.

Table 3.3 Dust mass constrained under strongest polarized scattering case

Epoch **(Days)**	**Dust**	θ_{max} **(°)**	**r** **(cm)**	**Mass**(θ_{max}) **($M_\odot$)**	**Mass**(θ_{90°) **($M_\odot$)**
t=277	Milky Way	100	6.1×10^{17}	$(3.2 \pm 0.4) \times 10^{-5}$	$(3.6 \pm 0.4) \times 10^{-5}$
	Silicate	114	5.1×10^{17}	$(2.5 \pm 0.3) \times 10^{-6}$	$(3.7 \pm 0.4) \times 10^{-6}$
	Graphite	92	6.9×10^{17}	$(3.6 \pm 0.4) \times 10^{-6}$	$(3.6 \pm 0.4) \times 10^{-6}$
t=416	Milky Way	100	9.2×10^{17}	$(3.7 \pm 1.9) \times 10^{-6}$	$(4.1 \pm 2.1) \times 10^{-6}$
	Silicate	114	7.7×10^{17}	$(2.9 \pm 1.4) \times 10^{-7}$	$(4.3 \pm 2.2) \times 10^{-7}$
	Graphite	92	1.0×10^{18}	$(4.1 \pm 2.1) \times 10^{-7}$	$(4.2 \pm 2.1) \times 10^{-7}$

A single dust clump close to the plane of the SN leads to the largest possible polarization. Any more complex geometric distribution of the dust will be less efficient in polarizing scattered light from the SN and therefore more dust will be needed to achieve the same degree of polarization. Nonetheless, the single dust clump model can provide useful insights even for a more complicated geometry such as a non-uniform dust distribution. In such a case, the polarization will be related to the fluctuations of the column depth of dust to the SN. In the optically thin case, the required fluctuation will be the same as the optical depth required in the case of single dust clump.

For dust distributed in a torus viewed edge-on, the amount of dust needed is $\sim 2\pi/\delta\theta$ times larger than demanded by the single dust clump model with an angular size $\delta\theta$. Figure 3.5 presents the amount of dust demanded to account for the observed change in polarization at different scattering angles. This allows the single dust clump to move along the iso-delay light surface and provides a more universal description of the implied dust mass. The minimum amount of dust that is compatible with a torus geometry is still consistent with constraints from NIR observations, i.e., $10^{-5} M_\odot$ inside a radius 1.0×10^{17} cm (Johansson et al., 2017). If we model the polarization in terms of a non-uniform spherical

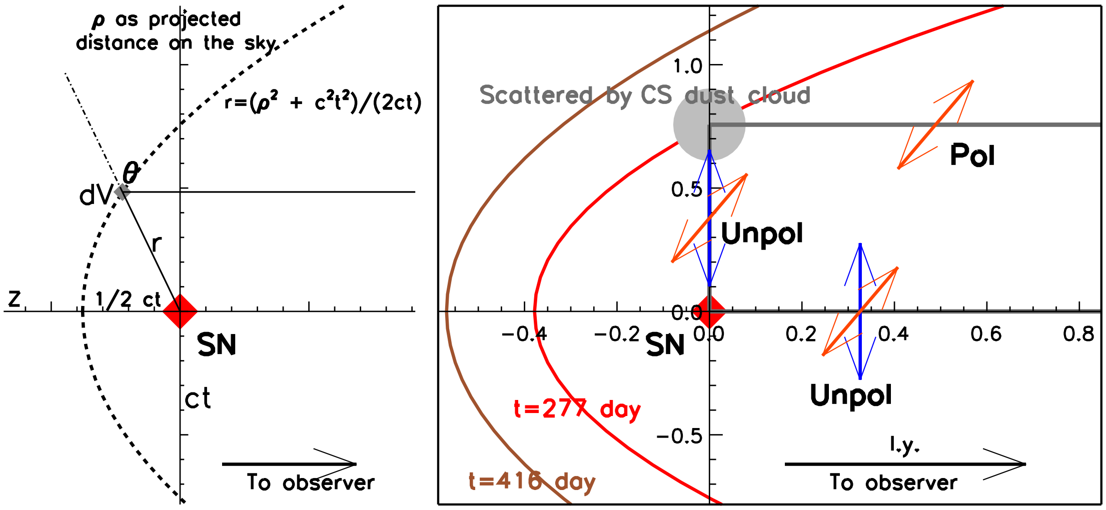

Figure 3.4 The left panel illustrates the geometrical configuration of a circumstellar light echo around a supernova. The right panel provides a schematic diagram describing the contribution from photons scattered by a circumstellar dust cloud at large angle and the time-variant polarization of the SN 2014J. Paraboloids represent the iso-delay light surfaces at different epochs (as labeled).

shell, the required mass will be larger than or of the order of $4\pi/\delta\theta^2$ times of that for a single dust clump. Such a large amount of dust is marginally inconsistent with the cited NIR observations.

3.3.3 Stability check of the *HST* polarimetry

Unfortunately, *HST* has obtained only few polarimetric observations of point sources that could be used to asses the quality of the observation of SN 2014J. To test the stability of *HST* polarimetry, we have also measured the polarization of a number of stars and nebular sources in the *HST* WFC field. The positions of these stars and nebulae are marked in Figure 3.6. The evolution of their polarization between day 277 and day 416 is visualized in Figure 3.7. The measured polarizations for three brightest reference sources are compiled in Table 3.4. This demonstrates that the polarization between the two epochs is stable to within 0.3%. Additionally, the polarization measured in different regions of the

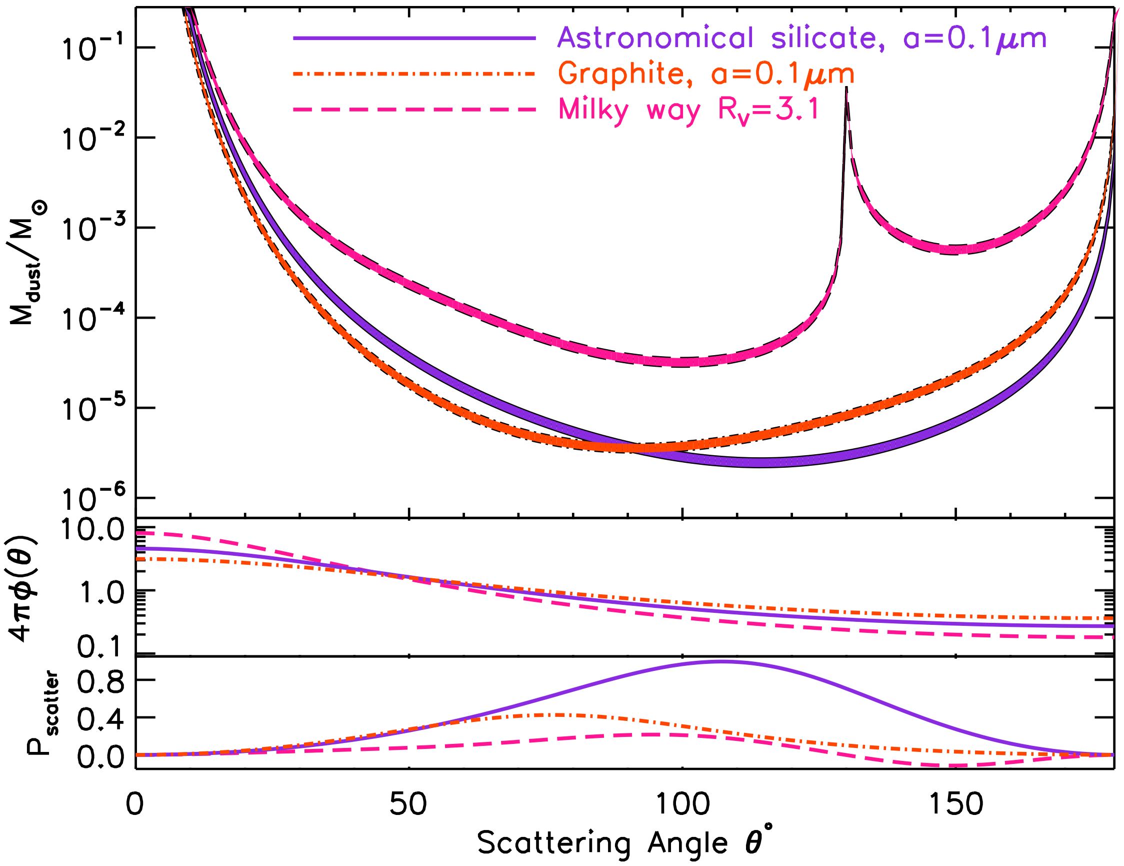

Figure 3.5 The dust mass required to produce the observed level of polarization as a function of scattering angle caused by the dust clump's position along the iso-delay surface at day 277 (when the deviant polarization was measured). In the upper panel, the cases of silicate, graphite, and Milky Way dust are represented by a solid purple, dotted-dashed orange, and dashed pink line, respectively. The scattering-angle dependency of scattering phase functions and polarization efficiencies obtained from Weingartner & Draine (2001) are overplotted in the middle and bottom panel, respectively.

Table 3.4 Measured polarizations of bright and polarized sources

	R.A.(J2000) (h:m:s)	Dec (J2000) (d:m:s)	Aperture radius ($''$)	q[1] (%)	q[2] (%)	u[1] (%)	u[2] (%)
SN 2014J	09:55:42.11	69:40:25.90	0.35	-0.61±0.08	-1.15±0.12	-3.79±0.08	-4.22±0.12
			0.40	-0.60±0.08	-1.13±0.12	-3.82±0.08	-4.24±0.12
			0.45	-0.57±0.08	-1.22±0.12	-3.82±0.08	-4.34±0.12
Source 1	09:55:47.29	69:40:48.37	0.65	0.41±0.17	0.72±0.10	-0.80±0.17	-1.18±0.10
			0.70	0.42±0.17	0.64±0.10	-1.03±0.16	-1.28±0.10
			0.75	0.46±0.16	0.55±0.09	-1.13±0.16	-1.45±0.09
Source 2	09:55:46.51	69:40:43.37	0.35	1.18±0.26	1.33±0.15	-2.64±0.26	-2.81±0.15
			0.40	1.39±0.24	1.38±0.14	-2.52±0.24	-2.85±0.13
			0.45	1.15±0.23	1.39±0.13	-2.22±0.22	-2.96±0.13
Source 3	09:55:46.97	69:40:41.73	0.65	3.55±0.06	3.60±0.03	-2.98±0.06	-3.29±0.03
			0.70	3.50±0.06	3.53±0.03	-2.95±0.06	-3.24±0.03
			0.75	3.43±0.06	3.46±0.03	-2.89±0.06	-3.23±0.03

[1] Measurement of $F475W$ from epoch 1 at t=277 days.

[2] Measurement of $F475W$ from epoch 2 at t=416 days.

CCD agrees within 0.2% (Sparks et al., 2008). Therefore, we conclude that the observed change in polarization of the SN is not an artifact of the instrument.

3.4 Discussion

Compared to the dust detected at day 277, the amount of dust at still closer distances from the SN is constrained by the absence, at the 0.2% level, of variability of the early polarization. Following Yang et al. (2017a) and the definitions on the relations between 2-dimensional light echoes and 3-dimensional scattering dust distributions (Chevalier, 1986; Sparks, 1994; Sugerman, 2003; Tylenda, 2004; Patat, 2005), we briefly define the geometry of circumstellar light echoes used through this paper, also sketched in the left panel of Figure 3.4. The SN is placed at the origin of the sky plane, a scattering volume element dV lies at radius r from the SN, and z gives the foreground distance of the scattering volume element along the line of sight. The light echo can be very well approximated by a paraboloid, which focus coincided with the SN. Definding ρ as the projected distance of a scattering volume element to the SN perpendicular to the line of sight (the z direction),

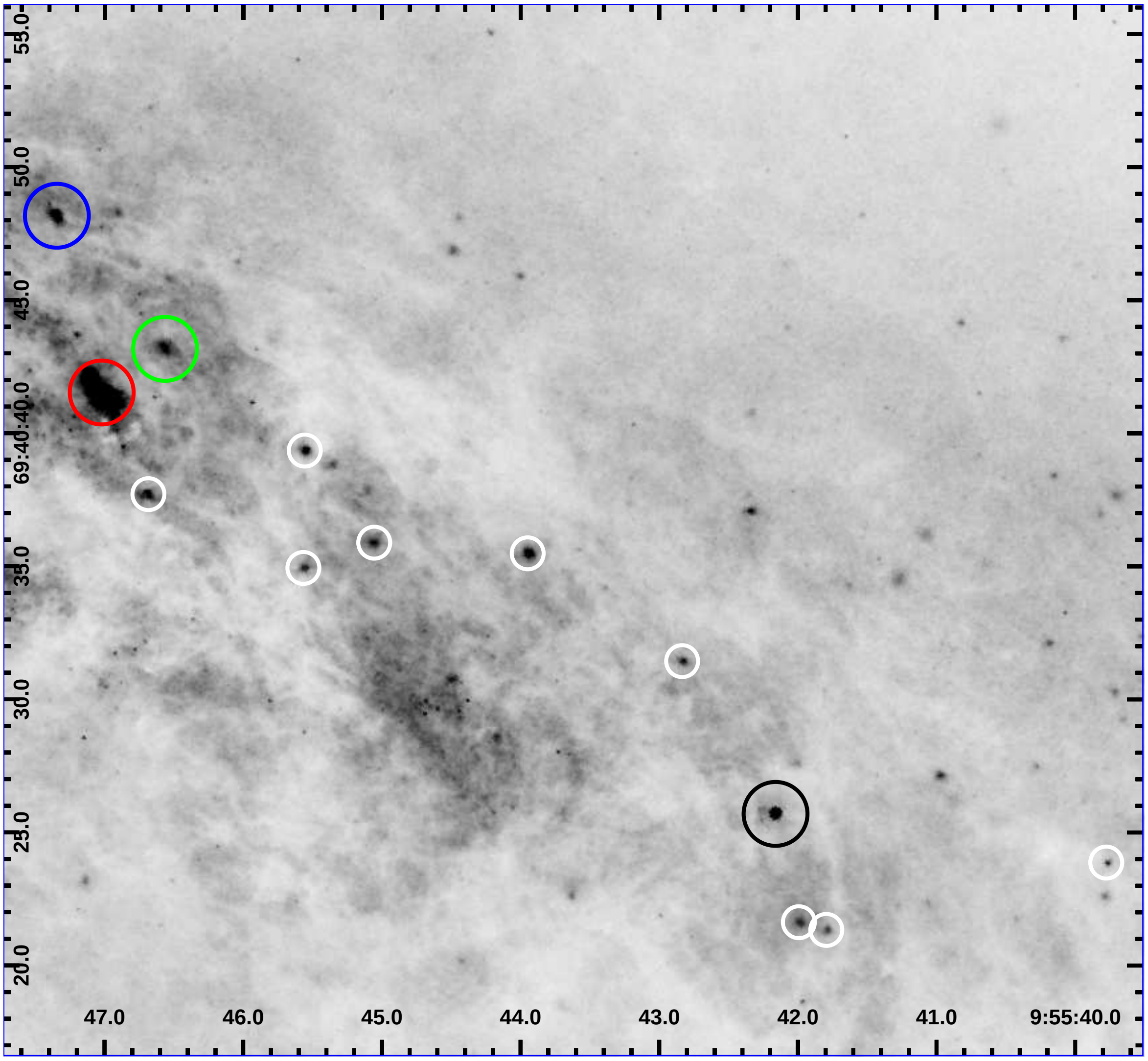

Figure 3.6 The bright sources in the *HST* images used for determining the stability of the polarization measurements. Each source has been monitored with 3 aperture sizes. The SN is circled in black. The three brightest nebular blobs are circled in large red, green, and blue, respectively. Fainter sources with larger errors are circled in white.

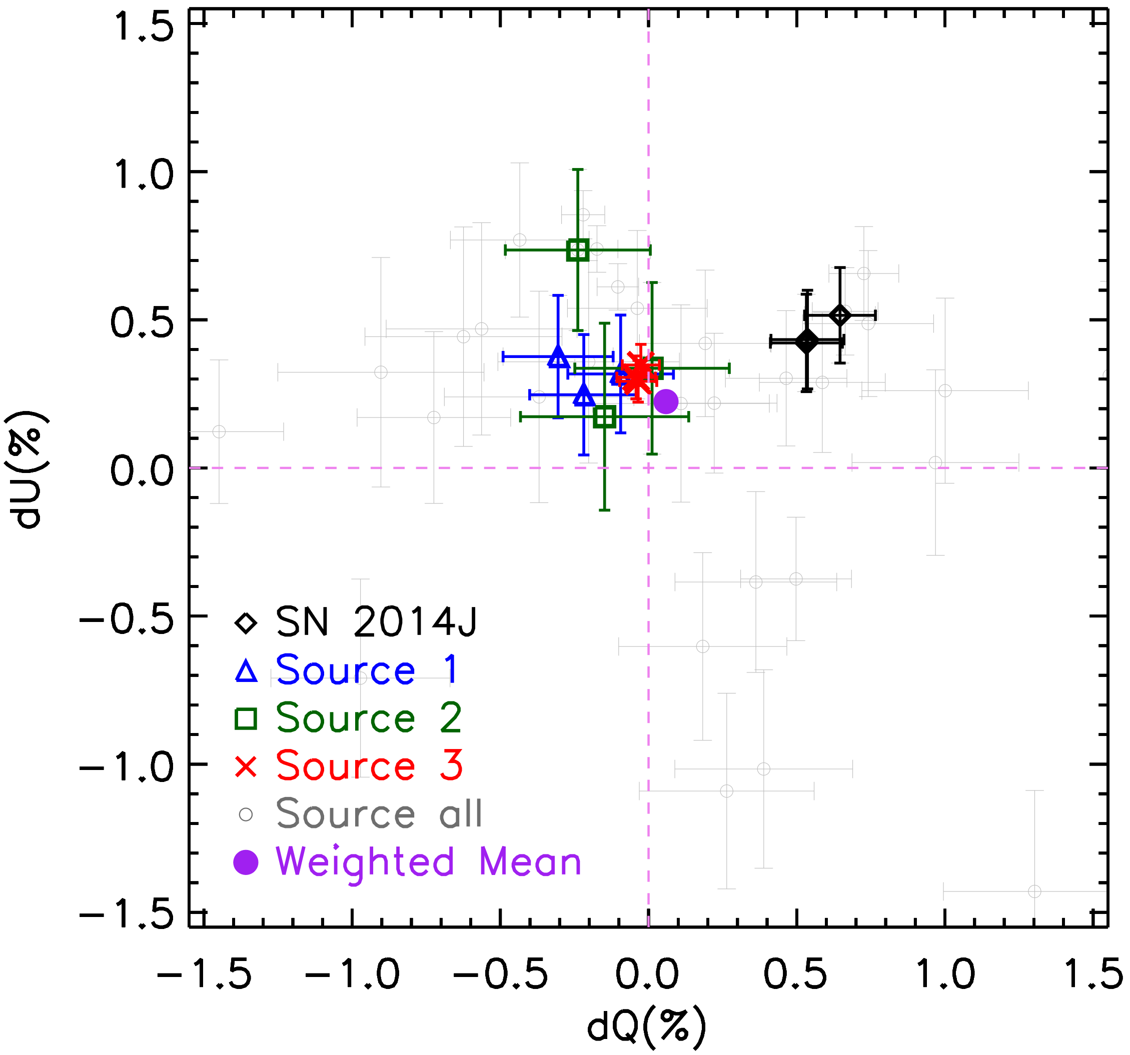

Figure 3.7 Bright sources used to check the stability of *HST* polarimetry. The horizontal and vertical axes represent the difference between the Q and U values respectively measured on days 416 and 277. SN 2014J and three brightest sources are marked with black and colored circles as in Figure 3.6. Fainter sources with larger errors are presented in light gray. The weighted mean difference of all sources is presented by the purple dot. The brightest source, manifested in red, together with the weighted mean, depict no time evolution at the 0.2% level. This comparison suggests a genuine evolution of the polarization of SN 2014J between days 277 and 416.

the distance r of the scattering volume element from the SN is:

$$r = \frac{1}{2}\left(\frac{\rho^2}{ct} + ct\right), \tag{3.11}$$

where t is the time sinece the SN radiation burst and c denotes the speed of light. The scattering angle is therefore given by:

$$\cos\theta(\rho, t) = z/(z + ct) \tag{3.12}$$

Under the single-clump hypothesis, and considering the scattering angle of $114°$ with respect to the line of sight which the minimum amount of astronomical silicate dust is required, using Equation 3.11 and 3.12, the day 33 observations imply less than 2.6$\times 10^{-7} M_\odot$ at a distance around 23.5 light days (7.3$\times 10^{16}$ cm). Similarly, the *HST* observations on day 416 constrain the mass of a single dust clump to less than 4.0$\times 10^{-7} M_\odot$ (1 σ) at a distance around 296 light days (7.7$\times 10^{17}$ cm). Approximating the radial distribution of the clump with a Gaussian function of $\sigma = 20$ light days generally increases the amount of dust by a factor of 2 to 2.5 with respect to the above assumed δ function. A single dust clump is of course an over-simplification. The lower limit it places on the mass on day 277 may be much larger if the dust is more uniformly distributed, either in a thin slab in the plane of the sky at the location of the SN 2014J or in a radially more extended volume.

Around optical maximum as well as after day 416, the measured polarizations are the same to within the errors but different from those on day 277. The interpretation of these data is highly model dependent, but the difference of polarization between these epochs and at the SN maximum dipict that there is either no dust at distances of $\sim\ 6.1 \times 10^{16}$ cm (day 33) and $\sim\ 7.7 \times 10^{17}$ cm (day 416), or the dust distribution at these distances is extremely uniform, such that on the plane of sky the opacity fluctuation is less than $\sim$0.02. From day $\sim$649 on, the errors of polarization measurements are much larger but the results are still consistent with the polarization at maximum light. Therefore, between days $\sim$416 and $\sim$1181 the light from SN 2014J did not encounter significant amounts of dust.

The distance of $\sim 5.1\times10^{17}$ cm ($\sim$197 light days) between the dust and the SN can be compared to a putative nova outburst of the progenitor prior to the SN explosion. For a typical nova ejection speed of 1,000 km/sec, this distance is consistent with an eruption 160 years ago. If the nova outburst was brief, the ejected mass is likely distributed in a thin clumpy shell. This can explain the absence of dust closer to and farther away from the SN. In some other variant of the single-degenerate model, the SN may have exploded inside a planetary nebula shell (Wang et al., 2004; Tsebrenko & Soker, 2015). Also in the context of a possible merger of two degenerate stars pre-explosion ejection of matter is possible. The above inferred distance of dust from the SN permits the time elapsed since this event to be estimated. For both a single- or double-degenerate progenitor, the distribution of the pre-explosion ejecta will not be well described by a single cloud.

The position angles at day 277 and day 416 exhibit no time evolution, except in the i-band data taken on day 416, where the degree of polarization is low and the position angle suffers larger uncertainties. A possible explanation is that the dust particles in the scattering cloud(s) are asymmetric and aligned with the foreground dust that is responsible for the extinction. It is unclear how such long-distance coordination might be physically possible, but comparable dust alignment has indeed been found in galactic ISM regions (Andersson et al., 2013). Alternatively, the magnetic field close to the SN may be highly coherent and very efficient in quickly aligning dust particles. This is qualitatively discussed in the following paragraphs.

When light from the SN is scattered by circumstellar dust grains, the E-vector will be perpendicular to the scattering plane so that the polarization PA is only related to the location of the dust, here approximated by a single clump. We also assume that the cross section of aligned dust grains is larger along their major axis, and the polarization is strongest when the grains' major axis is perpendicular to the scattering plane. For instance, needle-like grains at a right angle to the scattering plane can produce a significant amount of polarization. If a large-scale magnetic field permeates both the circumstellar dust and the line-of-sight ISM, it may align the grains in the dust clump and in the ISM to the same direction. Consequently, the E-vector of dichroically absorbed light on the direct SN-Earth line of sight is normal to that of the light scattered by circumstellar dust. Figure 3.8 gives a schematic view of the net E-vector generated by circumstellar scattering and dichroic extinction.

The scattered light will be polarized with the E-vector perpendicular to the scattering plane, whereas the transmitted light will have an E-vector preferably absorbed in this direction. If the dust grains in the foreground ISM and the circumstellar dust are both aligned by the same local interstellar magnetic field, this explains why the polarization decreases as the unresolved circumstellar light echo studied in this paper emerges. Most efficiently scattering (and polarizing) dust consists of particles aligned with the ambient magnetic field. Under this assumption, the aligned interstellar grains do not impose a rotation on the integrated polarization of the SN point source: Either the scattered light contributes only a few percent to the total received light so that the rotation is small (i.e. barely measurable) even in the more general case in which the scattering polarization in the resolved circumstellar light echoes and the direct line-of-sight interstellar polarizations are not perpendicular. Or the circumstellar light echoes are contributing more substantially to the total signal. Then, a rotation in the integrated PA with respect to the interstellar direction will happen if the polarization PA in circumstellar light echoes is not perpendicular to the local interstellar magnetic field.

This reasoning permits an independent limit to be set on the flux contribution of the

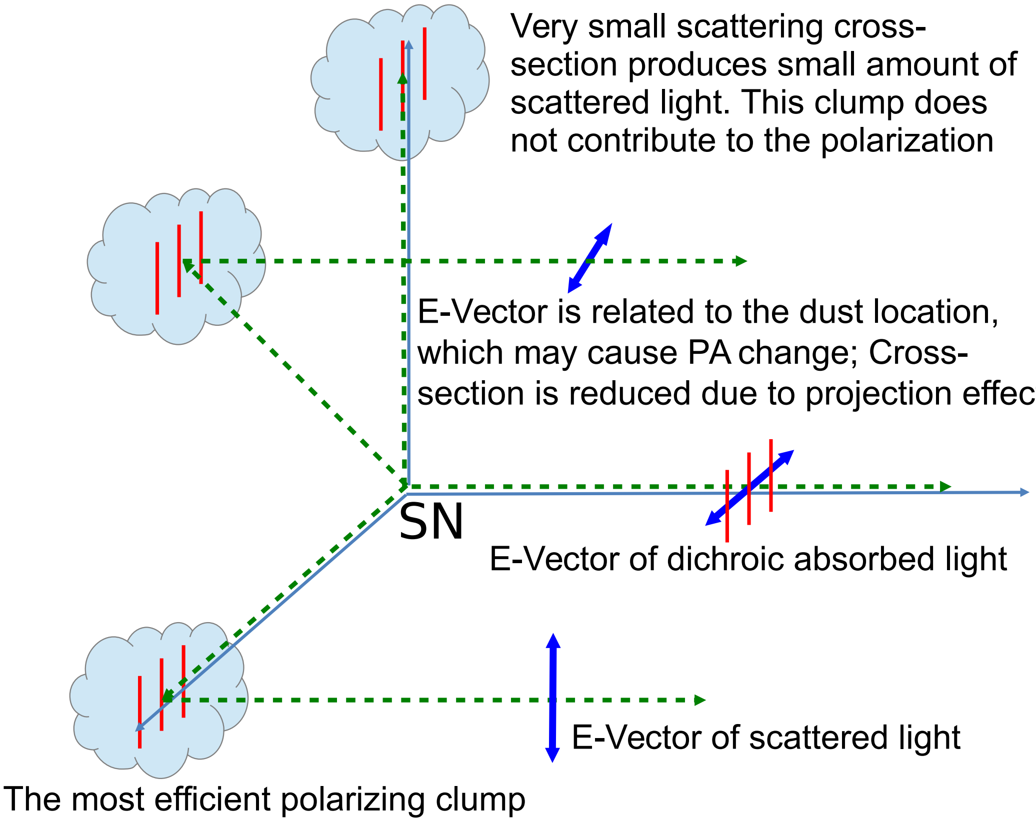

Figure 3.8 Schematic diagram explaining the consistent polarization PA if the grains in circumstellar dust clumps are aligned with the local interstellar magnetic field. Red bars illustrate dust grains aligned by an ad-hoc coherent magnetic field, green dashed lines represent light from the SN, blue arrows demonstrate the direction of E-vectors of the net polarized light. The observer is located outside the right edge of the figure.

light echo. If the maximal change in $P.A.$ is 5° and the polarization imparted by the scattering is 50%, the contribution by a light echo to the total observed flux should not exceed $\sim$ 2%. For the most efficient case of circumstellar polarization, i.e., by a single clump of astronomical silicate with $a = 0.1\ \mu m$ at ∼114° (Section 3.3.2), the polarization decrease observed on day 277 (from ∼4.9% to ∼3.8%) can be explained with a ∼2% flux contribution from the light echoes in the $F475W$-band as is also illustrated by the inset panel in Figure 3.3.

Circumstellar dust composed of needle-like grains aligned with the interstellar magnetic field has a net polarizing effect even if its spatial distribution is spherically symmetric. The reasons is that scattering in planes aligned with the grains would produce zero polarization. Therefore, it would not lead to a cancellation of the polarization produced by scattering on planes perpendicular to the dust alignment, and a net polarizatiuon arises. This further indicates that the polarization of light echoes is not necessarily an indication of the ni=on-axisymmetry of the dust cistribution.

It is also possible that the dust grains in pre-explosion ejecta are aligned neither with a magnetic field nor the radiation torque of the SN, i.e., exhibit no dominant directional preference. Instead of being elongated but randomly oriented, dust grains may alternatively have nearly spherical shape with little polarizing power because the difference between minimal and maximal extinction efficiencies is small. In all these cases, the deviant integrated degree of polarization and the invariant PA observed on day 277 require the dust to be at certain position angles relative to the SN, i.e., the scattering plane is perpendicular to the interstellar magnetic field. This would introduce an orthogonal polarization component to the integrated light. Under these circumstances, the vectorial combination of the two components only affects the degree of polarization but not the PA as observed in SN 2014J.

Polarization traces the magnetic field and enables a unique approach to the study of its interaction with asymmetric dust. Careful studies of dust grains aligned through the ‘radiative alignment torque’ (R.A.T.) are able to provide testable predictions on various properties (Lazarian & Hoang, 2007). Andersson & Potter (2010) found that dust surrounding the Herbig Ae/Be star HD 97300 does not align with the stellar wind, ruling out significant contributions to grain alignment through the stellar wind or radiation pressure of the star (the so-called Gold alignment, see, i.e., Gold, 1952). At a star-cloud distance of $\sim$0.03 pc, a weak dependence of the grain alignment efficiency on the angle between the magnetic field and the radiation field anisotropy is seen (Andersson & Potter, 2010). This confirms the grain alignment predicted by the R.A.T model. But it remains still unclear, whether an intrinsic magnetic field of the progenitor of SN 2014J or the ambient magnetic field in the ISM of M82 could align the dust grains quickly enough within the relatively short time (estimated above at $\sim$160 years) between the pre-explosion mass ejection and the SN explosion.

It is important to stress that resolved light echoes around SN 2014J caused by interstellar dust (Crotts, 2015; Yang et al., 2017a) do not compromise the inference of circumstellar dust from the evolution of not spatially resolved polarization. The scattering angle by foreground ISM is $\theta \sim \sqrt{2ct/z} \sim 4^{\circ}.5(\frac{t}{1year}\frac{100pc}{z})^{1/2}$, where t denotes the time after optical maximum and z is the foreground distance of the dust to the SN. At so small scattering angles, the polarization of resolved light echoes results from the dichroic extinction by partially aligned non-spherical paramagnetic dust grains. This interstellar polarization can be determined from the SN polarization around maximum light (Kawabata et al., 2014; Patat et al., 2015). Moreover, any such polarization signal that at the distance of M82 is unresolved by *HST* is expected to be constant with time. Therefore, it cannot explain the deviant measurement on day 277.

Spitzer mid-infrared observations have set an upper limit on the amount of dust around SN 2014J inside a radius of 1.0×10^{17} cm (Johansson et al., 2017). The value of $10^{-5} M_\odot$ is consistent with the polarimetrically inferred amount of $\sim 2 \times 10^{-6} M_\odot$ at 6×10^{17} cm from the SN (Johansson et al., 2017). In addition, variable interstellar KI lines have been observed and may form about 10 light years in front of the SN (Graham et al., 2015b). Moreover, numerous Na, Ca and K features along the SN-Earth line of sight were detected (Patat et al., 2015). Possible CSM components among them contribute at most marginally to the late-time polarization because of the small polarizing effect at small scattering angles.

3.5 Summary

Monitoring with the imaging polarimetry mode of the *HST* ACS/WFC at six epochs from 277 and 1181 days after maximum light has probed the circumstellar environment of the Type-Ia supernova 2014J. The polarization exhibited a conspicuous deviation on day 277 from all other epochs. This difference can result from light scattered by silicate dust ejecta of $\gtrsim 10^{-6} M_\odot$ located $\sim 5 \times 10^{17}$ cm ($\sim$0.5 light years) from SN 2014J. If attributed to the progenitor of SN 2014J, the distance of the dust from the SN constrains the time of ejection. It is consistent with a nova-like eruption about 160 years before the SN explosion for a typical speed of 1,000 km/sec.

The polarization at other epochs is consistent with the interstellar polarization around the optical maximum. This rules out significant circumstellar dust at distances between $\sim$1 light year and $\sim$3.3 light years to SN 2014J. The mass of the pre-explosion ejecta and the time difference between such an event and the SN explosion are also consistent with most of the double-degenerate scenarios discussed in Margutti et al. (2014) and references therein. Therefore, the polarimetry of SN 2014J contributes essential information for the understanding of the nature and pre-explosion evolution of the progenitors of Type-Ia SNe. But in the case of SN 2014J it cannot discriminate between single- and double-degenerate models.

The single-event-like time dependence of the degree of the polarization and the constancy of the polarization angle can be understood if the circumstellar dust of SN 2014J is aligned with the ambient interstellar magnetic field. However, both grains with low asymmetry and elongated grains aligned by the radiative torque by the progenitor's radiation could lead to the same effect if the dust cloud is located at a right angle to the interstellar polarization. Polarimetry of light echoes around Galactic novae can enable critical tests of the alignment mechanism of dust grains.

Acknowledgments

We greatly appreciate Dave Borncamp and the *HST* ACS team in fixing the distortion correction issues in ACS/WFC polarized images. We also thank Jian Gao, Bi-wei Jiang, Kevin Krisciunas, Armin Rest, and Nicholas Suntzeff for helpful discussions. Some of the data used in this study were obtained from the Mikulski Archive for Space Telescopes (MAST). STScI is operated by the Association of Universities for Research in Astronomy, Inc., under NASA contract NAS5-26555. Support for MAST for non-HST data is provided by the NASA Office of Space Science via grant NNX09AF08G and by other grants and contracts. The supernova research by Y. Yang, P. J. Brown, and L. Wang is supported by NSF grant AST-0708873. P. J. Brown was partially supported by a Mitchell Postdoctoral Fellowship. Y. Yang and M. Cracraft also acknowledge support from NASA/STScI through grant HST-GO-13717.001-A, grant HST-GO-13717.001-A, HST-GO-14139.001-A, and HST-GO-14663.001-A. The research of J. Maund is supported through a Royal Society University Research Fellowship. L. Wang is supported by the Strategic Priority Research Program "The Emergence of Cosmological Structures" of the Chinese Academy of Sciences, Grant No. XDB09000000. L. Wang and X. Wang are supported by the Major State Basic Research Development Program (2013CB834903), and X. Wang is also supported by the National Natural Science Foundation of China (NSFC grants 11178003 and

11325313).

4. LATE-TIME FLATTENING OF TYPE IA SUPERNOVA LIGHT CURVES: CONSTRAINTS FROM SN 2014J IN M82

4.1 Introduction

The astronomical community widely agrees that luminous hydrogen-poor Type Ia supernovae (SNe) explosions are powered by the thermonuclear runaway of ($\geqslant 1M_{\odot}$) carbon/oxygen white dwarfs (WDs Hoyle & Fowler, 1960). The accretion-induced explosion fuses ~0.1-1.0$M_{\odot}$ of radioactive ^{56}Ni. Type Ia SNe cosmology, which uses Type Ia SNe as the most accurate distance indicators at redshifts out to z ~2 (Riess et al., 1998; Perlmutter et al., 1999; Riess et al., 2016). Amazingly, this accuracy is achieved without knowing exactly the nature of various progenitors.

Prior to maximum luminosity, the light curve of Type Ia SNe is powered by the energy generated by the decay of explosion-synthesized radioactive nuclei. The reprocessing in the ejecta converts the energy to longer wavelengths. The decay chain of ^{56}Ni→^{56}Co→^{56}Fe provides the main source of energy deposition into the ejecta of Type I SNe (Arnett, 1982). During the early phases, the optically-thick ejecta trap the energy. The dominant process is Compton scattering of γ-rays produced by the decay ^{56}Ni + $e^{-} \rightarrow ^{56}$Co $+ \gamma + \nu_e$, ($t_{1/2}$ ~6.08 days), which allows energy to escape as X-ray continuum or absorbed by the material in the ejecta via the photoelectric effect (see Milne et al., 1999; Penney & Hoeflich, 2014 for comprehensive reviews). The produced ^{56}Co decays to stable ^{56}Fe, and the ^{56}Co decay process, with half-life $t_{1/2}$ ~77 days, dominates after ~200 days, when the expanding ejecta become more and more optically thin, and the column density decreases as t^{-2} (e.g., Arnett, 1979; Chan & Lingenfelter, 1993; Cappellaro et al., 1997;

Reprinted with permission from Yang et al. 2017b, Manuscript AAS05033, arXiv:1704.01431

Milne et al., 1999). The ^{56}Co decays Eighty-one percent of the ^{56}Co decays as follows: electron capture: $^{56}\text{Co} + e^- \rightarrow ^{56}\text{Fe} + \gamma\ +\ \nu_e$, and the remaining through annihilation of high energy positrons in the ejecta, $^{56}\text{Co} \rightarrow ^{56}\text{Fe} + e^+\ + \gamma\ + \nu_e$.

Observations at extremely late phases provide unique opportunities to examine various models exploring the effects of a magnetic field. As long as energy deposition is dominated by positrons being completely trapped by the magnetic field, the slope of the bolometric light curve should match the ^{56}Co decay rate. On the other hand, Milne et al. (1999) suggested a "radially combed" magnetic field, or even a magnetic-field-free situation as no magnetic field in radial directions will leads to an increasing fraction of positron escape, and the light curve should decline faster than the rate of ^{56}Co decay. The discrepancy between the "trapping scenario" with a confining magnetic field and the case without magnetic field can be as significant as 2 magnitudes in the photometric light curves from 400 - 800 days (see Figure 9 of Milne et al., 1999). Similar variations of the late-time light curves have been found by Penney & Hoeflich (2014) based on measuring positron transport effects and their dependency on the magnetic field with late-time line profiles. However, they drew different conclusions. As the SN envelope undergoes homologous expansion, the morphology of the magnetic field remains, but the Lamor radius increased linearly with time. Therefore, the fraction of escaped photons would exhibit a time-dependence due to the variations of the magnetic field. The light curve should decline faster than the rate of ^{56}Co decay.

Additonally, different effects of nucleosynthesis can be testable through the very late photometric evolution of Type Ia SNe and may be used to discriminate between different explosion models. Two of the most favorable explosion channels: a delayed detonation in a Chandrasekhar-mass white dwarf (Khokhlov, 1991) and a violent merger of two carbon-oxygen white dwarfs (Pakmor et al., 2011, 2012), will result in late-time light curves behaving differently due to different amounts of ejecta heating from ^{57}Co and ^{55}Fe (Röpke et al., 2012). Therefore, fitting the decline rate of the light curve at extremely late times provides a unique opportunity to test the enigmatic explosion mechanisms of Type Ia SNe.

Increasing evidence shows the flattening of Type Ia SN light curves around 800 to 1000 days, i.e., SN 1992A ($\sim$950 days; Cappellaro et al., 1997, Cappellaro et al., 1997), SN 2003hv ($\sim$700 days; Leloudas et al., 2009), and SN 2011fe ($\sim$930 days; Kerzendorf et al., 2014). This flattening cannot be explained even by complete trapping of the ^{56}Co positrons. Seitenzahl et al. (2009) suggested that additional heating from the Auger and internal conversion electrons, together with the associated X-ray cascade produced by the decay of ^{57}Co$\rightarrow$^{57}Fe ($t_{1/2}$ $\approx$272 days) and ^{55}Fe$\rightarrow$^{55}Mn ($t_{1/2}$ $\approx$1000 days), will significantly slow down the decline of the light curve.

Only very recently, Graur et al. (2016) carried out an analysis of the light curve of SN 2012cg as late as $\sim$ 1055 days after the explosion and excluded the scenario in which the light curve of SN 2012cg is solely powered by the radioactive decay chain ^{56}Ni$\rightarrow$^{56}Co$\rightarrow$^{56}Fe, unless there is an unresolved light echo $\sim$14 magnitudes fainter than the SN peak luminosity. Another very careful study on the late-time evolution of SN 2011fe has already extended the observing effort to an unprecedented 1622 days past the $B-$band maximum light (Shappee et al., 2016). This analysis has clearly detected the radioactive decay channel powered by ^{57}Co, with a mass ratio of log(^{57}Co/^{56}Co)= $-1.62^{+0.08}_{-0.09}$. This abundance ratio is strongly favored by double degenerate models which require a lower central density. The detection of ^{55}Fe is still unclear at these late epochs (Shappee et al., 2016). Another study based on the pseudo-bolometric light curve for the SN 2011fe has measured the mass ratio of ^{57}Co to ^{56}Co to be 1.3 – 2.5 times the solar value, which is broadly consistent with the ratios predicted for the delayed detonation models (Dimitriadis et al., 2017). Additionally, spectroscopic information of the nearby SN 2011fe has been obtained at 981 days (Graham et al., 2015a) and 1034 days (Taubenberger et al., 2015). Strong energy input from the radioactive decay of ^{57}Co is required, without which the optical spectrum would be underproduced by a factor of $\sim$4 (Fransson & Jerkstrand, 2015). The mass ratio of ^{57}Ni to ^{56}Ni produced, which gives a strong constraint on the Type Ia SN explosions, is found to be roughly 2.8 and 2 times of the solar ratio for SN 2011fe and SN 2012cg, respectively (Fransson & Jerkstrand, 2015; Graur et al., 2016).

SN 2014J was first discovered on Jan 21.805 UT by Fossey et al. (2014) in the very nearby starburst galaxy M82 (3.53$\pm$0.04 Mpc, Dalcanton et al., 2009). Later observations constrained the first light of the SN to Jan. 14.75 UT (Zheng et al., 2014; Goobar et al., 2014). This date is consistent with the early rising recorded by the 0.5-m Antarctic Survey Telescope (AST) during its test observations (Ma et al., 2014) as well as with other pre-discovery limits reported by various groups (Denisenko et al., 2014; Itagaki et al., 2014; Gerke et al., 2014). SN 2014J reached its $B-$band maximum on Feb. 2.0 UT (JD 2,456,690.5) at a magnitude of 11.85$\pm$0.02 (Foley et al., 2014). Follow-up photometric and spectroscopic observations have been made by various groups (Johansson et al., 2017; Lundqvist et al., 2015; Bonanos & Boumis, 2016; Srivastav et al., 2016). The strength of γ-ray lines (Churazov et al., 2014; Diehl et al., 2015) and an analytic model fit to the pseudo bolometric light curve (Srivastav et al., 2016) of SN 2014J suggest that $\sim$0.5-0.6 $M_\odot$ of ^{56}Ni has been synthesized in the explosion. In this paper, we present our late time *HST* photometric observations of SN 2014J and fit both the $F606W$ (broad V) band and an estimate of the pseudo-bolometric luminosity evolution with the Bateman equation considering the luminosity contributed by the decay of ^{56}Co, ^{57}Co, and ^{55}Fe. In addition to following a similar approach presented in Graur et al. (2016), we provide a careful astrometric analysis to the time-evolution of the position and profile of the SN 2014J point source at very late epochs.

Table 4.1 Log of photometric observations of SN 2014J with *HST* ACS/WFC POLV

Filter	Polarizer	Date	Exp	Phase[a]	Date	Exp	Phase[a]	Date	Exp	Phase[a]
		(UT)	(s)	Days	(UT)	(s)	(Days)	(UT)	(s)	(Days)
F475W	POL0V	2014-11-06	3×130	276.5	2015-03-25	3×400	415.6	2015-11-12	4×1040	648.5
F475W	POL120V	2014-11-06	3×130	276.5	2015-03-25	3×400	415.6	2015-11-12	4×1040	648.7
F475W	POL60V	2014-11-06	3×130	276.5	2015-03-25	3×400	415.7	2015-11-12	4×1040	648.8
F606W	POL0V	2014-11-06	2×40	276.6	2015-03-27	3×60	417.9	2015-11-12	4×311	649.0
F606W	POL120V	2014-11-06	2×40	276.6	2015-03-27	3×60	418.0	2015-11-13	4×311	649.0
F606W	POL60V	2014-11-06	2×40	276.6	2015-03-27	3×60	418.0	2015-11-13	4×311	649.1
F775W	POL0V	2014-11-06	2×30	276.6	2015-03-27	3×20	418.0	2015-11-12	4×100	648.5
F775W	POL120V	2014-11-06	1×55	276.6	2015-03-27	3×20	418.0	2015-11-12	4×100	648.7
F775W	POL60V	2014-11-06	1×55	276.6	2015-03-27	3×20	418.0	2015-11-12	4×100	648.9
F475W	POL0V	2016-04-08	4×1040	796.2	2016-10-12	4×1040	983.1			
F475W	POL120V	2016-04-08	4×1040	796.4	2016-10-12	4×1040	983.3			
F475W	POL60V	2016-04-08	4×1040	796.6	2016-10-12	4×1040	983.4			
F606W	POL0V	2016-04-08	4×311	796.8	2016-10-14	3×360	985.1			
F606W	POL120V	2016-04-08	4×311	796.8	2016-10-14	3×360	985.1			
F606W	POL60V	2016-04-08	4×311	796.9	2016-10-14	3×360	985.1			
F775W	POL0V	2016-04-08	4×100	796.2	2016-10-12	4×202	983.1			
F775W	POL120V	2016-04-08	4×100	796.4	2016-10-12	4×202	983.3			
F775W	POL60V	2016-04-08	4×100	796.6	2016-10-12	4×202	983.4			

[a] Days since B maximum on 2014 Feb. 2.0 (JD 245 6690.5).

4.2 Observations and Data Reduction

We imaged the SN 2014J with the *Hubble Space Telescope* Advanced Camera for Surveys/Wide Field Channel (*HST* ACS/WFC) during five visits (V1-V5) under multiple *HST* programs: GO-13717 (PI: Wang), GO-14139 (PI: Wang), and GO-14663 (PI: Wang), i.e., V1∼day 277, V2∼day 416, V3∼day 649, V4∼ day 796, and V5∼ day 983, relative to its $B-$band maximum at a mgnitude of 11.85±0.02 on Feb. 2.0 UT (JD 2,456,690.5, Foley et al., 2014). Figure 4.1 shows the field around SN 2014J. A log of observations is presented in Table 4.1. Exposures obtained with different ACS visual polarizers and in different filter combinations and visits have been aligned through *Tweakreg* in the *Astrodrizzle* package (Gonzaga et al., 2012).

The throughput of each ACS/WFC polarizer being used by the *Synphot* software does not match the values determined by on-orbit calibrations. We corrected the polarizers' throughput with the values deduced by on-orbit calibrations (i.e., Table 12 of Cracraft

---

http://www.stsci.edu/institute/software_hardware/stsdas/synphot

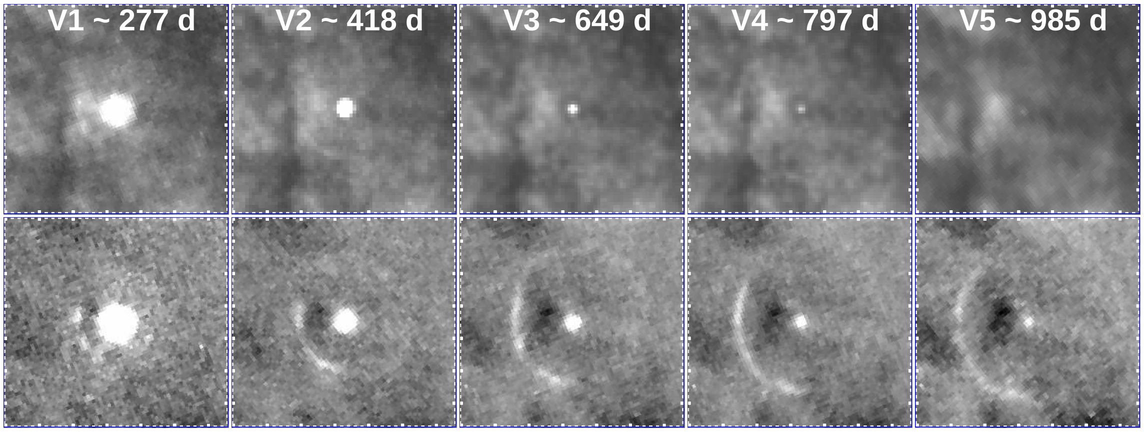

Figure 4.1 *HST* ACS/WFC $F606W$ (upper panels) and associated $F606W - F555W$ (lower panels) images of SN 2014J obtained in different visits as labeled. Each square measures $3''.2 = 54$ pc along its sides (north is up, east is left). The distance between little tick marks corresponds to $0''.1$.

& Sparks, 2007, also see Biretta et al., 2004). Following the three polarizers case described in earlier works by Sparks & Axon (1999), we deduced the Stokes vectors from the observations. In this work, we only discuss the observed flux from the SN 2014J, and the intensity maps (Stokes I) are the only required input parameter to this analysis.

$$I = \frac{2}{3}[r(POL0) + r(POL60) + r(POL120)],$$

where $r(POL0)$, etc. are the count rates in the images obtained through the three polarizers. The polarimetric properties of the SN 2014J among different late phases will be discussed in a future work.

After ∼600 days past maximum light, the SN became sufficiently dim and the count rates at the central pixels of the SN PSF became comparable to the bright part of the nebulosity close to the SN. The field shows that the SN lies at one end of a dark lane, and just west of a bright patch of nebulosity. A background subtraction procedure significantly diminishes the time-invariant signals and improves the photometry of evolving faint sources. Unfortunately, we found no pre-SN Hubble images, either with or without the polarizers, showing the same region using filters compatible with our observations. Images obtained on March 29 2006 (program #10776; PI:Mountain) with *HST* ACS/WFC in the $F435W$, $F555W$, and $F814W$ were used as background templates for our $F475W$, $F606W$, and $F775W$ exposures, respectively. For each band, the background templates have been scaled and subtracted from the intensity map. Measurements were made with a circular aperture of $0.''1$ (2 pixels in the ACS/WFC FOV) with aperture corrections according to Hartig (2009) and Sirianni et al. (2005). The photometry has been performed using the IRAF APPHOT package. The residual of the background has been estimated by the median pixel value of an annulus around the SN. Compromising between determining the local background residual with nearby pixels and excluding the contamination from resolved interstellar light echoes (Yang et al., 2017a), we choose the inner and outer radii as $1.''2$ (24 pixels) and $1.''5$ (30 pixels) for V1 and V2, and $0.''6$ (12 pixels) and $0.''8$ (16 pixels) for V3, V4, and V5. Table 4.2 presents the AB magnitude of SN 2014J at five late epochs. The photometric uncertainties include the Poisson noise of the signal, the photon noise of the background, the readout noise contribution (3.75 electrons/pixel for ACS/WFC), and the uncertainties in aperture corrections. These quantities were added in quadrature.

This photometry strategy has been carried out considering that extremely nonuniform background structures dominate the error budget in the late phases of the SN 2014J photometry, especially in V4 and V5. For the scientific consideration of this study, which is testing the models for the light curve evolution at very late phases, the major concern in the data reduction procedure is to obtain the correct decline rate of the SN light curves. Therefore, we conducted a sanity check to test the reliability of our measurement by per-

---

IRAF is distributed by the National Optical Astronomy Observatories, which is operated by the Association of Universities for Research in Astronomy, Inc., under cooperative agreement with the National Science Foundation (NSF).

Table 4.2 *HST* ACS/WFC late-time photometry of SN 2014J

Filter	$F475W$		$F606W$		$F775W$	
Visit	Phase[a]	AB Magnitude	Phase[a]	AB Magnitude	Phase[a]	AB Magnitude
1	276.5	17.363±0.002	276.6	17.429±0.002	276.6	16.742±0.002
2	415.6	19.464±0.002	418.0	19.602±0.004	418.0	18.276±0.005
3	648.7	22.363±0.006	649.0	21.962±0.008	648.7	21.427±0.009
4	796.4	23.266±0.011	796.8	22.917±0.017	796.4	22.492±0.019
5	983.3	24.169±0.027	985.1	23.936±0.047	983.3	23.294±0.027

Table 4.3. *HST* Late-time light curve decline rate of SN 2014J

Period[a]\Filter (Days)	$F475W$ (Δmag/100 days)	$F606W$ (Δmag/100 days)	$F775W$ (Δmag/100 days)
277 – 416	1.510±0.002	1.537±0.003	1.085±0.003
416 – 649	1.244±0.003	1.021±0.004	1.366±0.004
649 – 796	0.611±0.009	0.646±0.013	0.721±0.014
796 – 983	0.483±0.016	0.540±0.026	0.429±0.018

[a] Approximate days after B maximum, 2014 Feb. 2.0 (JD 245 6690.5).

forming photometry on differenced images from our observations obtained at different epochs. This directly measures the differential fluxes and therefore the light curve decline rate. The decline rates between all the epochs calculated from photometry shown in Table 4.3 and measured by this sanity check agree within ∼2% and are smaller than the photometric uncertainties.

We correct our measurements for both the interstellar dust extinction in the SN host galaxy and the Galactic extinction towards the SN 2014J. In fact, any imperfection in the extinction correction will only affect the individual magnitudes but no the decaline rates of the light curves. A peculiar extinction law R_V ∼1.4 towards the SN 2014J line of sight has been suggested by many studies (Amanullah et al., 2014; Brown et al., 2015; Foley et al., 2014; Gao et al., 2015; Goobar et al., 2014). In this study, we adopt R_V = 1.44±0.03 and A_V = 2.07±0.18 from Foley et al. (2014) for the extinction from the host galaxy and R_V = 3.1 and $E(B-V) = 0.054$ mag for the Galactic extinction following Foley et al. (2014) based on Dalcanton et al. (2009) and Schlafly & Finkbeiner (2011). Extinction in $F475W$, $F606W$, and $F775W$ has been calculated for each component using a reddening law from Cardelli et al. (1989) with the corresponding R_V value. Both components are added to account for the total extinction towards SN 2014J for each *HST* ACS bandpass.

4.3 Analysis

In this section, we will test different mechanisms powering the late-time light curve, and whether the light curve behavior is consistent with the prediction for the delayed-detonation and the violent merger progenitor scenarios following a similar procedure as Graur et al. (2016) for SN 2012cg. We assume that the ejecta do not interact with any circumstellar material. The pseudo-bolometric light curve for SN 2014J was calculated over a wavelength range from 3500 - 9000 based on our multi-band optical photometry. We briefly summarize the steps as follows:

(1) Based on the lack of significant spectral evolution of SN 2011fe compared to a spectrum at 593 days (Graham et al., 2015a), we assume the MODS/LBT spectrum of SN 2011fe at 1016 days (Taubenberger et al., 2015) represents the major spectral features of SN 2014J on V3∼day 649, V4∼day 796, and V5∼day 983. The spectrum was downloaded from the WISeREP archive .

(2) We then perform synthetic photometry from this spectrum for the $F475W$, $F606W$, and $F775W$ bands.

(3) We calculate the differences between the synthetic photometry of the SN 2011fe spectrum and our extinction-corrected, observed photometry of SN 2014J.

---

http://wiserep.weizmann.ac.il

(4) We calculate the scale factors between the observed and synthetic magnitudes in each filter.

(5a) We warp the spectrum using a 2nd order polynomial fit to the scale factors at the effective wavelength .

(5b) Alternatively, for each epoch, we fit a single wavelength-independent gray scale across all wavelengths.

(6) We iterate steps (2) - (5) until the synthetic and observed photometry match to better than 0.02 mag in each filter for (5a), or the mean difference between the synthetic and the observed photometry converges to its minimum value for (5b), which standard deviation among the three filters gives 0.11 mag.

The pseudo-bolometric luminosity for each epoch was obtained by integrating the scaled spectrum returned from (5a) or (5b) over the wavelength range from 3500 - 9000. The errors on the pseudo-bolometric light curve were computed through a Monte Carlo re-sampling approach using photometric errors. The warping in (5a) aims at iteratively producing spectra consistent with the photometry which follows a very similar procedure as described in Shappee et al. (2016), while the scaling in (5b) is less sensitive to the extrapolation of the polynomial correction to the spectrum. The pseudo-bolometric luminosities calculated from these two approaches agree within 6% at all epochs, compatible with the uncertainties of the Monte Carlo approach. Our analysis of the bolometric evolution of SN 2014J is based on the bolometric luminosity obtained with (5b). Qualitatively similar results have been obtained by duplicating the entire analysis based on (5a) as follows.

In Figure 4.2 we present the spectra with the warping procedure (left panel) and with the gray scaling (right panel). For comparison, in each upper panel, we overplotted the

---

http://pysynphot.readthedocs.io/en/latest/properties.html#pysynphot-formula-efflam

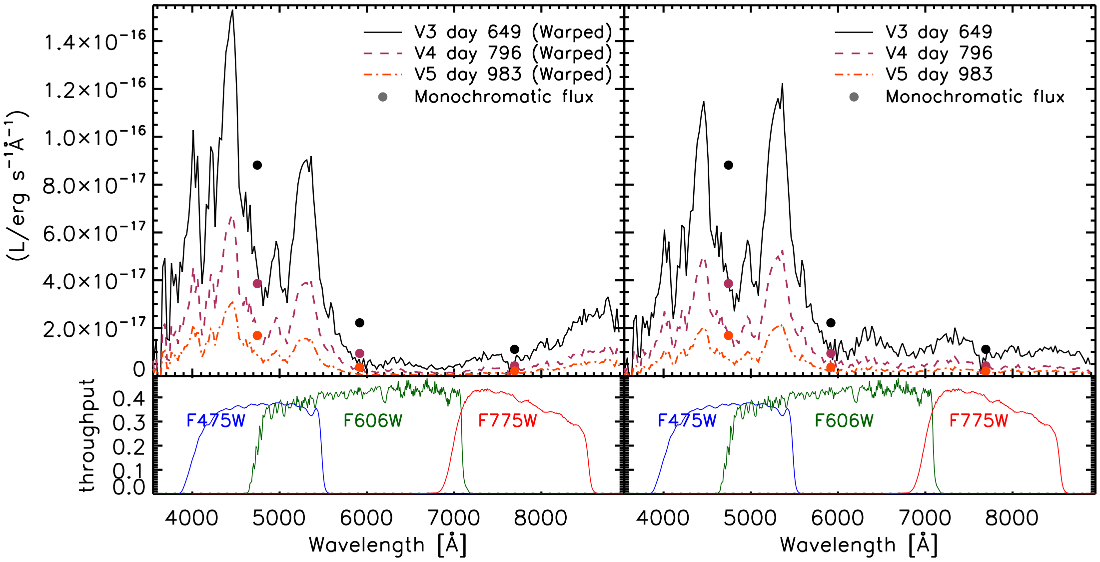

Figure 4.2 The constructed late-time SED for SN 2014J. Dots show the bandpass monochromatic flux from *HST* observations at their effective wavelengths. Solid lines show the spectra with the warping procedure (left panel) and with the gray scaling (right panel) as described in Section 3. The lower panels present the total bandpass throughput curve (*HST* + ACS) for our $F475W$, $F606W$, and $F775W$ observations, showing the spectral response corresponding to the monochromatic fluxes calculated from the observed photometry.

bandpass monochromatic flux calculated as the product Total Counts × PHOTFLAM , where PHOTFLAM is the inverse sensitivity (in erg cm^{-2} s^{-1} $^{-1}$) representing a signal of 1 electron per second. The lower panels present the total bandpass throughput curve (*HST* + ACS) for our $F475W$, $F606W$, and $F775W$ observations. The spectra on the left panel are iterated to agree quantitatively with the photometry. Visual differences between the monochromatic bandpass flux and the spectra arise because PHOTFLAM used for the SED assumes a smooth AB spectrum, which is different than the SN spectrum (see Brown et al., 2016 for a comprehensive discussion).

This can be obtained with the ACS Zeropoints Calculator at https://acszeropoints.stsci.edu/

http://www.stsci.edu/hst/acs/analysis/throughputs

In the left panels of Figure 4.3, we present the $F475W$, $F606W$, and $F775W$-band luminosity of SN 2014J after the extinction correction. In addition to fitting the pseudo-bolometric light curve after ∼500 days with the contribution from three decay chains: ^{56}Co→^{56}Fe, ^{57}Co→^{57}Fe, and ^{55}Fe→^{55}Mn (an 'all isotopes' model), we also fit the same model to our $F606W$-band observations. Here we have assumed that after ∼500 days the $F606W$-band, which is centered at wavelength 5888.8 and with a width of 2570, captures the dominant Fe features ([Fe II] around 4700 and 5300, blended [Fe II]λ7155 and [Ni II]λ7378 around 7200; Taubenberger et al., 2015) and to be proportional to the bolometric light curves as V-band observations (Milne et al., 2001).

Limited by a small number of visits, we approximate the 'all isotopes' model with two free parameters: the mass ratio $M(^{57}\mathrm{Co})/M(^{56}\mathrm{Co})$, and a scale factor to match the $F606W$ photometry (or the pseudo-bolometric luminosity) with the model-calculated values. Using the solution to the Bateman equation which describes the abundances and activities in a decay chain as a function of time (following Seitenzahl et al., 2014), and by counting the decay energy carried by charged leptons and X-rays, the luminosity contribution from a single decay chain gives:

$$L_A(t) = 2.221\frac{C}{A}\frac{\lambda_A}{\mathrm{days}^{-1}}\frac{M(A)}{M_\odot}\frac{q_A^l + q_A^X}{\mathrm{keV}}\exp(-\lambda_A t_e) \times 10^{43}\mathrm{ergs}^{-1} \tag{4.1}$$

where C is a scaling factor, A gives the corresponding atomic number, λ_A is the inverse mean lifetime which is $\lambda_A = \tau_A^{-1} = \ln(2)/t_{1/2,A}$, $M(A)$ is the total mass of a certain decaying element, q_A^l and q_A^X are the average energies per decay carried by charged leptons and X-rays, respectively, and t_e is the time since explosion. Due to the limited data points in our late-time photometry, we used a ratio of $M(^{57}Co)/M(^{55}Fe) \approx 0.8$ (model rpc32; Ohlmann et al., 2014). The values of λ_A, q_A^l and q_A^X used here are obtained from

---

where the filter throughput is larger than 0.05%

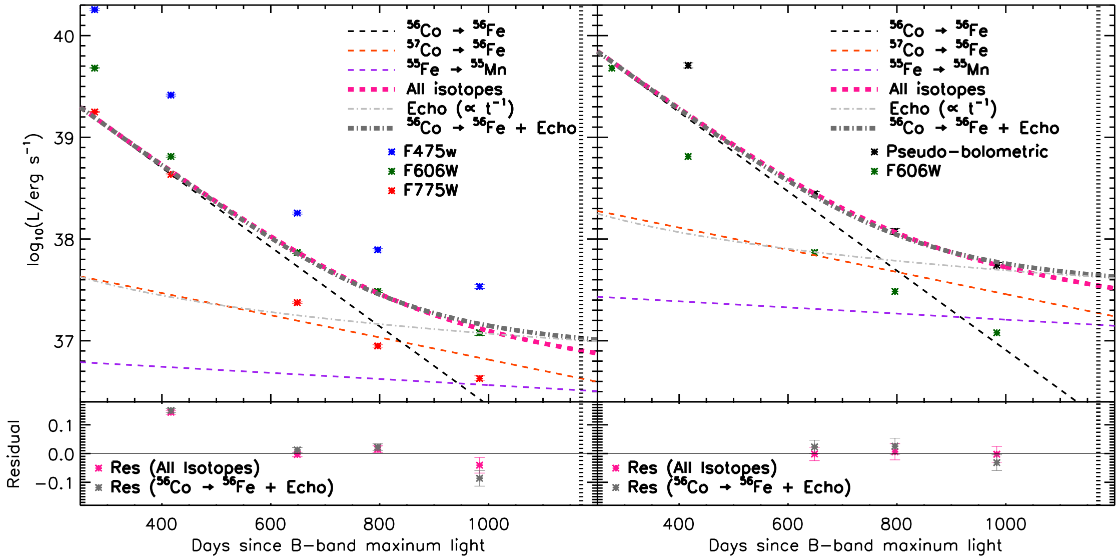

Figure 4.3 Luminousity evolution of the monochromatic fluxes from the broadband observations (left panel) and pseudo-bolometric flux (right panel) with possible mechanisms explaining the flattening of the light curves of SN 2014J. The left panel presents the fitting and residuals of V3, V4, and V5 based on $F606W$-band observations while the right panel shows a similar plot based on the constructed pseudo-bolometric luminosity. The $F475W$ and $F775W$-band observations in the left panel and the $F606W$-band observations in the right panel are shown for comparison. The $F606W$-band observations after $\sim$500 days have been assumed to be proportional to the bolometric light curves (Milne et al., 2001) and free from possible γ-ray photons. Only observations after 500 days have been fitted with models accounting for all the listed isotopes or ^{56}Co plus a faint, unresolved light echo. One more visit around day 1180 will be obtained: the scheduled date of observations is marked by vertical dotted lines.

Table 1 of Seitenzahl et al. (2009) and Table 2 of Seitenzahl et al. (2014). We justify our assumptions as follows: (1) The total deposition function is determined by both the net deposition functions for $\gamma-$rays and positrons. The $\gamma-$rays produced by the annihilation of the positrons are subject to both deposition functions. By simply assuming the radioactive source is confined to the center of a spherical distribution of ejecta yields a fraction $1 - e^{-\tau_\gamma}$ of the energy produced by $\gamma-$rays would be left behind in the ejecta (Swartz & Wheeler, 1991). The $\gamma-$ray optical depth τ_γ drops significantly as t^{-2} and we neglect contributions from γ-rays because the SN ejecta became transparent to γ-rays at $t \gtrsim$500 days (Milne et al., 2001); (2) Limited by a small number of photometric point, we begin by fitting Equation 4.1 assuming full trapping of positrons/electrons. In other words, we assume positrons, electrons, and X-rays are fully trapped, instantaneously deposited, and radiate their energy. One should also note that very recently, Dimitriadis et al. (2017) found that the late-time bolometric light curve of SN 2011fe is consistent with both models, namely positron/electron escape as well as complete trapping, that allow for positron/electron escape, and models that have complete positron/electron trapping but do allow for redistribution of flux to the mid-far IR.

The luminosity contribution from each decay channel is shown in Figure 4.3. The total luminosity given by these decay chains is represented by the pink dashed line. In the left panel, we show that a mass ratio of $M(^{57}\mathrm{Co})/M(^{56}\mathrm{Co}) = 0.076^{+0.009}_{-0.008}$ gives the best fit to the ‘all isotopes’ model based on the $F606W$-band observations after $t \sim 500$ days (V3, V4, and V5). The dot-dashed gray lines show the model including the luminosity from ^{56}Co decay and possible reflections from an unresolved t^{-1} light echo (see Graur et al., 2016). In the right panel, we show the same trend in a similar fitting based on the pseudo-bolometric light curve, which the mass ratio gives $M(^{57}\mathrm{Co})/M(^{56}\mathrm{Co}) = 0.094^{+0.017}_{-0.016}$.

If light echoes dominate the late time signal from the SN, we may expect a significant profile change or centroid drift if the circumstellar matter is distributed at sufficiently large distances from the SN. Light scattered by dust at such distances can produce measurable distortions to the image profiles if the scattered light dominates the total observed flux. At the distance of SN 2014J, 1 light year corresponds to 0.17 *HST* ACS/WFC pixels. Depending on the dust distribution, we may expect the stellar profiles to become non-point like, or the centroid of the stellar profile to drift at late time. We have checked the stellar profiles and found no significant deviations from a point source at all epochs of our observations. In the following, we provide a comprehensive check on the centroid position of the SN.

The barycenter of the stars and HII regions around SN 2014J were measured to estimate a possible change in the relative position of the light emission of the SN. The precision is limited by the scarcity of stars in the immediate vicinity of the SN, as well as the uncharacterized field distortions caused by ACS/WFC polarizers (see, i.e., Section 5.3 of Gonzaga et al., 2012). Figure 4.4 presents the apparent shift in position measured from our observations in $F475W$ and $F606W$. The RA and Dec were calculated using the image from V3, with the SN at the origin of the coordinates. The gray arrows show the vector difference of the originally measured positions of the star on two different epochs. The black arrow shows the same vector after a 2-D linear regression to remove the dependence on RA and Dec, which may be caused by residual errors of astrometric calibrations. The linear regression was found to be able to reduce the shift significantly in all cases. The reference objects for astrometric comparisons were selected within a radius of 500 pixels of the position of the SN. The FWHM of the objects was restricted to be less than 8 pixels. Only a small number objects in the earliest V1 satisfy these criteria due to the relatively short exposure time.

In Figure 4.4, the upper panels present the measurements based on the highest S/N $F475W$-band exposures, and the lower panels present the same figures for $F606W$. For instance, the upper-left panel presents the comparison between V3 and V1. The SN ex-

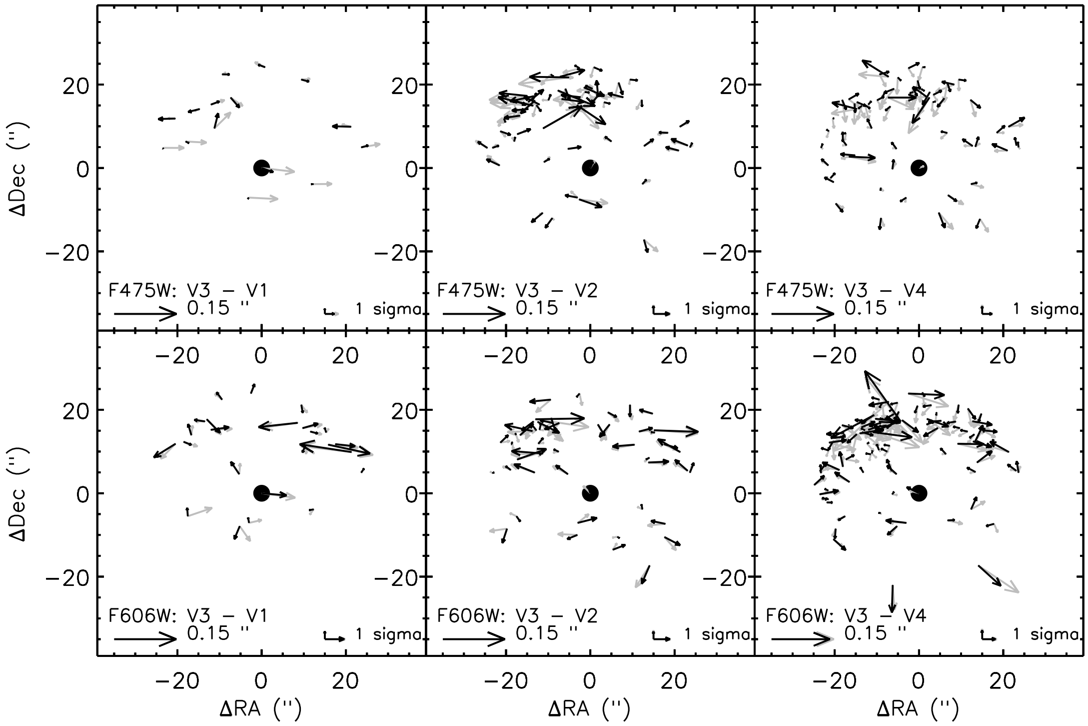

Figure 4.4 Astrometric comparisons of different visits. The x and y-axis are the position of bright sources relative to SN 2014J, most of which are HII regions in M82. The gray and black arrows are the relative motion between different visits prior to and after a linear regression with the RA and Dec. A 1-σ displacement calculated based on all the presented sources and scales are provided at the bottom right of each panel. No significant positional drift of the SN is found among all the cases, suggesting the absence of any circumstellar light echoes around 1 light year from the SN on the plane of the sky.

hibits an apparent motion of $0''.050$; after linear regression with the RA and Dec, this reduces to $0''.021$. This is in agreement with all the other objects in the field, which show an average distance shift of $0''.015$ and an RMS of $0''.013$. The upper-middle panel presents the comparison between V3 and V2. The SN exhibits an apparent drift in position of $0''.019$; after linear regression this reduces to $0''.005$. The field objects exhibit an average drift of $0''.013$ and an RMS of $0''.009$. This also implies that there is no apparent position drift of the SN with an upper limit of $0''.014$. The upper-right panel presents the comparison between V3 and V4. The original images exhibit a position shift of $0''.009$ for the SN. This is already too small to be a significant drift. After linear regression with RA and Dec, using the stars around the SN, the drift changes to $0''.010$. The mean drift of objects in the field is $0''.012$ with an RMS of $0''.007$. An upper bound on the centroid position drift of the SN between V3 and V4 is thus observed to be $0''.017$. Similar results were obtained for $F606W$-band exposures. In all cases, we have not observed a significant position drift of the SN. The absence of such drift sets a strong constraint on the nature of the late time emission from SN 2014J. If the significant flattening in $F606W$ is due to light echoes, the dust must be lie within $0''.017$ of the SN.

4.4 Discussion and Summary

Table 4.3 shows the decline rate of the light curves at different epochs. Before t ~600 days, the SN dims more rapidly than the light curve powered solely by the ^{56}Co decay. The γ-ray energy deposition becomes no longer significant after ~200 days, therefore, a substantial fraction of the flux may be shifting out of the optical bands into the infrared. Similar behavior has been discussed in the case of SN 2011fe (Kerzendorf et al., 2014) and SN 2003hv (Leloudas et al., 2009). After t ~600 days, a slower decay can be identified in all the $F475W$, $F606W$, and $F775W$-bandpasses.

Some observations of nearby Type Ia SNe show that their bolometric light curves at late phases follow the ^{56}Co decay channel (Cappellaro et al., 1997; Sollerman et al., 2004; Lair et al., 2006; Stritzinger & Sollerman, 2007; Leloudas et al., 2009). These observations suggest that a turbulent, confining magnetic field traps the positrons, resulting in local energy deposition (see Chan & Lingenfelter, 1993; Milne et al., 1999, 2001; Penney & Hoeflich, 2014). In contrast, ^{56}Co positron escape has been suggested in some cases (Milne et al., 1999, 2001). As the ejecta expand over time, the pre-configured magnetic field weakens to the point that the Larmor radius exceeds the size of the turbulence (see Penney & Hoeflich, 2014).

We fit both the $F606W$-band and a 'pseudo-bolometric' light curve using Bateman's equation for the luminosity contribution of the ^{56}Co, ^{57}Co, and ^{55}Fe decay channels. The best fit to the pseudo-bolometric light curve and the $F606W$-band light curve give a mass ratio $M(^{57}\mathrm{Co})/M(^{56}\mathrm{Co}) = 0.094^{+0.017}_{-0.016}$ and $0.076^{+0.009}_{-0.008}$, respectively. Assuming the same mass ratio yields for isotopes of the same iron-group elements (see Graur et al., 2016, based on Truran et al., 1967 and Woosley et al., 1973), our measurements correspond to $\sim$3.5 times the $M(^{57}\mathrm{Fe})/M(^{56}\mathrm{Fe})$ ratio of the Sun (i.e., $\sim$0.0217, see Table 3 of Asplund et al., 2009). This is higher than the solar ratio $\sim$1.8 predicted for the W7 model (calculated from Table 3 of Iwamoto et al., 1999), and the solar ratio $\sim$1.7 predicted for the near-Chandrasekhar-mass three-dimensional delayed-detonation model N1600 (calculated from Table 2 of Seitenzahl et al., 2013). The $M(^{57}\mathrm{Fe})/M(^{56}\mathrm{Fe})$ ratio in our measurements is also higher compare to the ratios $\sim$2 and $\sim$1.1 suggested by the late-time quasi-bolometric light curve analysis on SN 2012cg (Graur et al., 2016) and SN 2011fe (Shappee et al., 2016). A higher metallicity progenitor could decrease the production of ^{56}Ni and result in a higher $M(^{57}\mathrm{Ni})/M(^{56}\mathrm{Ni})$ ratio (Seitenzahl et al., 2013). An enhancement of neutron excess due to electron captures in the deflagration wave could lead to the same effect.

It has been suggested that beyond $\sim$500 days in the ejecta, energy is shifted from the optical and near-infrared to the mid- and far-infrared (referred as the infrared catastrophe, Axelrod, 1980, and see Fransson et al., 1996; Fransson & Jerkstrand, 2015). The V or optical luminosity may not represent the actual behavior of the bolometric light curves. This has never been observed so far in any Type Ia SNe (e.g., Sollerman et al., 2004; Leloudas et al., 2009; McCully et al., 2014; Kerzendorf et al., 2014; Graur et al., 2016; Shappee et al., 2016). However, Dimitriadis et al. (2017) suggested that the evolution of SN 2011fe, around 550 to 650 days, is consistent with both a model that allows for position/electron escape and a model allowing for a redistribution of flux from optical to the mid-far infrared. In our study, we fitted the $F606W$-band and optical bolometric luminosity after $\sim$650 days and do not consider the infrared catastrophe. Future studies based on a larger sample will be able to help distinguish these two possible scenarios.

In summary, our multi-band photometry of SN 2014J out to 985 days past the $B-$band maximum light clearly detected the flattening due to extra luminosity contributions other than the decay of ^{56}Co. We conclude that the high $M(^{57}\mathrm{Ni})/M(^{56}\mathrm{Ni})$ ratio estimated from the late-time luminosity evolution of SN 2014J favors a near-Chandrasekhar mass explosion model such as W7 of Iwamoto et al. (1999). Any significant circumstellar light echoes beyond 0.3 pc on the plane of the sky can be excluded by our astrometric analysis. The observations strongly suggest additional heating from internal conversion and Auger electrons of $^{57}\mathrm{Co}\rightarrow^{57}\mathrm{Fe}$; however, one should be cautious on the high mass ratio of ^{57}Ni to ^{56}Ni. Systematical uncertainties from the SED construction procedure, especially the missing information from NIR observations and the interpolation of the SED based on limited bandpass coverage should not be ignored (i.e., see Brown et al., 2016). Additionally, the reliability of approximating the bolometric luminosity evolution after t $\sim$500 days with the $F606W$-band emission requires more careful justification. Time for one more visit at $\sim$1180 days past the $B-$band maximum has already been allocated. This will provide another chance to better characterize the luminosity evolution of SN 2014J.

Acknowledgments

The authors are grateful to Dave Borncamp and the *HST* ACS team in fixing the distortion correction issues in ACS/WFC polarized images. Some of the data used in this study were obtained from the Mikulski Archive for Space Telescopes (MAST). STScI is operated by the Association of Universities for Research in Astronomy, Inc., under NASA contract NAS5-26555. Support for MAST for non-HST data is provided by the NASA Office of Space Science via grant NNX09AF08G and by other grants and contracts. This work also made use of the Weizmann interactive supernova data repository (WISeREP). The supernova research by Y. Yang, P. J. Brown, and L. Wang is supported by NSF grant AST-0708873. P. J. Brown was partially supported by a Mitchell Postdoctoral Fellowship. Y. Yang and M. Cracraft also acknowledge support from NASA/STScI through grant HST-GO-13717.001-A, grant HST-GO-13717.001-A, HST-GO-14139.001-A, and HST-GO-14663.001-A. The research of J. Maund is supported through a Royal Society University Research Fellowship. L. Wang is supported by the Strategic Priority Research Program "The Emergence of Cosmological Structures" of the Chinese Academy of Sciences, Grant No. XDB09000000. L. Wang and X. Wang are supported by the Major State Basic Research Development Program (2013CB834903), and X. Wang is also supported by the National Natural Science Foundation of China (NSFC grants 11178003 and 11325313).

5. OPTICAL SKY BRIGHTNESS AND TRANSPARENCY DURING THE WINTER SEASON AT DOME A ANTARCTICA FROM THE GATTINI-ALLSKY CAMERA

5.1 Introduction

Over the past centuries, people's growing demand for large astronomical facilities keeps pushing forward the progress of astronomical site selections. Some of the most major considerations for ground-based optical and IR astronomy include the seeing, atmospheric transparency and cloud coverage, number of clear nights, wind speed, precipitable water vapor, and thermal backgrounds. Various site surveys in recent years have revealed the advantages of the Antarctic plateau sites. Low and stable count rates of sky backgrounds in optical bandpasses have been measured at Dome C (Kenyon & Storey, 2006), the South Pole (Nguyen et al., 1996; Ashley et al., 1996), and Dome A (Zou et al., 2010; Sims et al., 2012a). High atmospheric transmission has been inferred at Dome A (Lawrence, 2004; Yang et al., 2009) and various Antarctic sites (Lawrence, 2004). Good average optical seeing above the boundary layer can be obtained at the South Pole, i.e. $0''.37$ at $\lambda = 2000$ at 17−27 m above the ground (Marks et al., 1996), and $0''.23$ at $\lambda = 2.4\ \mu m$ (Marks, 2002). At Dome C Lawrence et al. (2004) found seeing of $0''.27$, while Agabi et al. (2006) determined $0''.36 \pm 0''.19$, Aristidi et al. (2009) found $0''.36$, and Giordano et al. (2012) found $<0''.3$ at $\sim$30 m above the ground. See also Vernin et al. (2009) and Aristidi et al. (2015). Many astronomical observations could benefit from the consecutive periods of dark time at polar latitudes. Comparisons between different astronomical sites among the Antarctic plateau are being made regarding cloud coverage,

---

Reprinted with permission from Yang et al., 2016, Manuscript AAS03391R3, arXiv:1610.10094 aurorae, thickness of the boundary layer, seeing, humidity, and temperature (Saunders et al., 2009).

The high-altitude Antarctic sites of Dome A (latitude $80°22'$ S, longitude $77°21'$ E, elevation 4093 m) offer intriguing locations for future large-scale astronomical observatories. Site testing work since 2008 has confirmed Dome A to be an excellent astronomical site. The extremely thin turbulent boundary layer measured to be 13.9 m near the ground at Dome A enables a free-of-atmosphere observing condition for a telescope on a small tower (Bonner et al., 2010). Some other advantages including the low sky brightness measured in the SDSS i band (Zou et al., 2010), the outstanding low cloud coverage compared to other astronomical sites (Zou et al., 2010), and the extremely low atmospheric water vapor content (Sims et al., 2012b). Additionally, the airglow and aurorae at Dome A in the optical and near-IR range during the 2009 winter season have been characterized by Sims et al. (2012b), and only 2% of the time during 2008 winter season (solar minimum) has shown strong auroral events in the i-band (Zou et al., 2010). Dome A also has exceptional transmission and multi-day persistent superlative observing conditions in the Terahertz regime (Yang et al., 2010).

Time-series photometry has long been an essential tool to study the stellar properties as well as other astrophysical phenomena involving time-variant celestial objects. Long-term monitoring of stars to a very high degree of precision probes a wide range of frequencies. Over the last decades, there has been rapid progress in consecutive, high-quality, and high-cadence transiting surveys. Space-based missions including the Swift Ultraviolet/Optical Telescope (Gehrels et al., 2004; Roming et al., 2005) is leading the high-energy regime, the CoRoT satellite (Baglin et al., 2006) and the Kepler satellite (Borucki et al., 2010) are searching for Earth-size planets and performing asteroseismology on the field stars. A summary of ground-based untargeted transient and variable surveys can be found in Table 1 of Rau et al. (2009).

Consecutive monitoring for as long as months is not possible at single-site mid-latitude astronomical observatories. While space-based transient surveys achieve better accuracy due to the extremely low atmospheric absorption, turbulence, and light pollution, ground-based sites offer advantages such as unlimited cadence, flexible pointing, and the feasibility of following brighter targets. Taking the advantages of the long "winter night" as well as other remarkable observation conditions at Dome A, high quality time-series observations carried out with small telescopes have already obtained, opening a window for asteroseismology at Antarctica plateau sites.

Previous works demonstrated that high photometric accuracy can be acquired by small aperture telescopes at Dome A. The first and comprehensive studies on asteroseismology and stellar physics at Dome A Antarctica have been conducted by the 14.5 cm diameter Chinese Small Telescope ARray (CSTAR, Yuan et al., 2008), which has monitored an area around the South Celestial Pole since 2008. The nature of the CSTAR wide field design (FOV of $4.5^{\circ} \times 4.5^{\circ}$ and the absence of a sidereal tracking system introduced significant systematic uncertainties into stellar photometry. Various efforts have been made to reduce the systematic errors and to push the photometric precision below a few mmag, including the modeling of the inhomogeneous effects of clouds (Wang et al., 2012), the ghost images (Meng et al., 2013), and the systematic diurnal residuals (Wang et al., 2014b). Based on the detrended light curves obtained during the 2008 winter season, comprehensive studies on exoplanet candidates (Wang et al., 2014a), stellar variability (Wang et al., 2015), eclipsing binaries (Yang et al., 2015), and stellar flares (Liang et al., 2016) have been carried out. Other independent studies include the variable sources (Wang et al., 2011, 2013; Oelkers et al., 2015), and specific studies on the pulsation modes of RR Lyrae stars (Huang et al., 2015) and δ Scuti variables (Zong et al., 2015) based on the CSTAR observations in single or multiple years from 2008 through 2010. We also note the variable stars observed during the 2012 winter season (Li et al., 2015) with a single unit of the Antarctic Survey Telescopes (AST3, Yuan et al., 2014). In addition, time-series photometry studies have also been conducted at Dome C Antarctica, for instance, careful time-series multi-color photometry to study the stellar pulsation and evolution using the Photometer AntarctIca eXtinction (PAIX, Chadid et al., 2010, 2014, 2016).

These transient surveys at Antarctic sites with ∼10 cm class and larger telescopes have measured the stars within a magnitude range of ∼8 to ∼15 with a FOV of $\lesssim 20$ square degrees. The multi-band ultra-wide FOV imaging obtained by Gattini-Dome A camera during the 2009 winter season is also a valuable dataset considering its continuous monitoring of the flux variation of the third to seventh magnitude stars. Multi-band photometric results for bright targets obtained during the 2009 winter season by the Gattini-Dome A camera will be discussed in a future paper.

In this paper, we analyze a multi-wavelength dataset collected at Dome A, Antarctica, during the 2009 winter season. We have measured and calibrated the sky brightness in three photometric bands. We estimate the transparency variations and perform aperture photometry for those targets in the V magnitude range ∼3.5 to ∼7.5. We focus on targets in the sky south of declination -50°. The organization of this paper is as follows: In Section 2 we describe the instrument and observations. Section 3 discusses data reduction pipeline. In Section 4 we give our results, and in Section 5 our conclusions.

5.2 Importance of Sky Background Measurements

When doing astronomical photometry, the ideal result is to determine the brightness of individual celestial objects. However, various sources including the scattered light from the Sun, the Moon, the aurora and airglow, will contaminate the flux from the astronomical sources. A summary of the contributions to the light of the night sky has been provided by Roach & Gordon (1973) and Kenyon & Storey (2006). Considering the case of aperture photometry, the total flux integrated over the circular aperture can be expressed as

$Flux = Source + Sky + RN^2 + Dark$. The terms on the right-hand side are the source counts enclosed by the aperture from a celestial object, the sky background, the readout noise (RN^2) , and the electron counts from the dark current, respectively. Due to the discrete nature of the electric charge, a Poisson process models the counting process of the photons, and the error is given by the square root of the total counts. By adding the noise terms in quadrature, the signal-to-noise (S/N) for object measured in aperture with a radius r can be written as: $S/N = Source/\sqrt{Source + Sky + RN^2 + Dark}$. In a sky limited case, i.e., $\sqrt{Sky} > 3RN$, $S/N \approx Source/\sqrt{Sky}$. The temporal variation of the sky background significantly influences the efficiency and detection capability of ground-based astronomical facilities, especially in the low S/N regime.

Given the critical role played by sky brightness in astronomical site selection, the measurement of the background light of the sky has been carried out for over a century using photographic plates, photomultiplier tubes, and modern digital detectors. A classic monograph on the subject is *The Light of the Night Sky* by Roach & Gordon (1973). A comprehensive summary of the published sky background statistics is given by Benn & Ellison (1998). Some useful background can also be found in papers by Walker (1988), Krisciunas (1997), Patat (2003), Krisciunas et al. (2007), and references therein.

The daily and monthly variations of the sky brightness at the high-altitude Antarctic Dome A site are expected to be different than mid-latitude sites. It can be shown that the angle of solar elevation, α, can be approximated in terms of the solar declination angle on a given date, $\delta(d)$, the hour angle of observation at a given time during the day, $h(t)$, and the observer's latitude, ϕ:

$$\alpha = \sin^{-1}\Bigg(\sin\delta(d)\sin\phi + \cos\delta(d)\cos[h(t)]\cos\phi\Bigg) \tag{5.1}$$

The Sun's declination can be approximated by:

$$\delta = 23^\circ.45 \times \sin\left[\frac{2\pi}{365} \times (d + 284)\right] \tag{5.2}$$

Where d is the day of the year with January 1^{st} as $d = 1$; given $\phi = -80^\circ 22'$ of Dome A site, on the summer solstice ($d = 172$), the Sun obtains its lowest mean altitude over a sidereal day, i.e., $h(t)$ from 0^{hr} to 24^{hr}, α ranges from $-13^\circ.8$ to $-33^\circ.1$. Therefore, even continual darkness can be expected during the winter season at Antarctic sites, however, the latitude of Dome A never allows the Sun to stay more than 18° below the horizon for an entire sidereal day. The twilight due to the scattered light from the Sun and the Moon without the additional scattering by clouds need to be modeled to better understand the scattering effect of the atmosphere at Dome A. For other sites, Krisciunas & Schaefer (1991) present a model of the V-band sky brightness when there is moonlight. Liu et al. (2003b) also present a model of the brightness of moonlight as a function of lunar phase angle and elevation above the horizon. A much more advanced moonlight model, based on spectra taken at Cerro Paranal, Chile, is presented by Jones et al. (2013).

5.3 Instrument and Observations

5.3.1 Project goals

The multi-band sky brightness at Dome A, as well as the sky brightness among a large area of the night sky, are unknown quantities. The Gattini project was created to unambiguously measure the optical sky brightness within an incredibly large $90^\circ \times 90^\circ$ Field-Of-View (FOV), as well as the cloud coverage and aurora of the winter-time sky above such a high-altitude Antarctic site. The Gattini-Dome A All-Sky Camera (GASC, Moore et al., 2008) was installed on the PLATO (PLATeau Observatory) instrument module, which is an automated self-powered astrophysical observatory deployed to Dome A

(Yang et al., 2009), as part of the Chinese-led expedition to the highest point on the Antarctic plateau in January 2008. This single automated wide-field camera contains a suite of Bessell photometric filters (B, V, R) and a long-pass red filter for the detection and monitoring of OH emission. We have in hand one complete winter-time dataset (2009) from the camera that was returned in April 2010. The extremely large FOV of the GASC allows us to monitor the night sky brightness in the B, V, and R photometric bands and the cloud cover beginning in the 2009 winter season at Dome A over a wide range of zenith angles (0° to $\sim 30^\circ$). Multi-band sky intensities measured by GASC in combination with spectra obtained with the NIGEL instrument (Sims et al., 2010) will offer more comprehensive statistics on aurora and airglow. In addition, photometry of bright target stars in the GASC FOV with an unprecedented temporal window function is permitted by months of continual darkness during the Antarctic winter. An overview of the multi-band GASC FOV is shown in Fig. 5.1.

5.3.2 Dome A camera design and assembly

The Gattini Dome A All-sky camera was a novel low-cost pathfinder that ambitiously set out to measure the multi-year sky properties of one of the most remote and desolate sites on the planet. It was assembled at Caltech during 2008, and consists of a Nikon 10.5 mm f/2.8 GED DX fisheye lens mated to an Apogee Alta U4000 2K×2K interline camera, and filter wheel with an assortment of photometric filters. The system is housed inside a heated enclosure and controlled by a rugged PC based supervisor system. The project cost, including labor for fabrication and test but excluding logistical costs, was approximately $50,000 US dollars (in 2008). The system was pointing near the SCP, without guiding or field rotation. The system gives a mean plate scale of approximately 150″ pixel^{-1}, about 147″ pixel^{-1} near the center of the FOV and $\sim 155''$ pixel^{-1} near the edges of the FOV. The entire field is about $85^\circ \times 85^\circ$.In between the lens and the camera is a 5-position filter

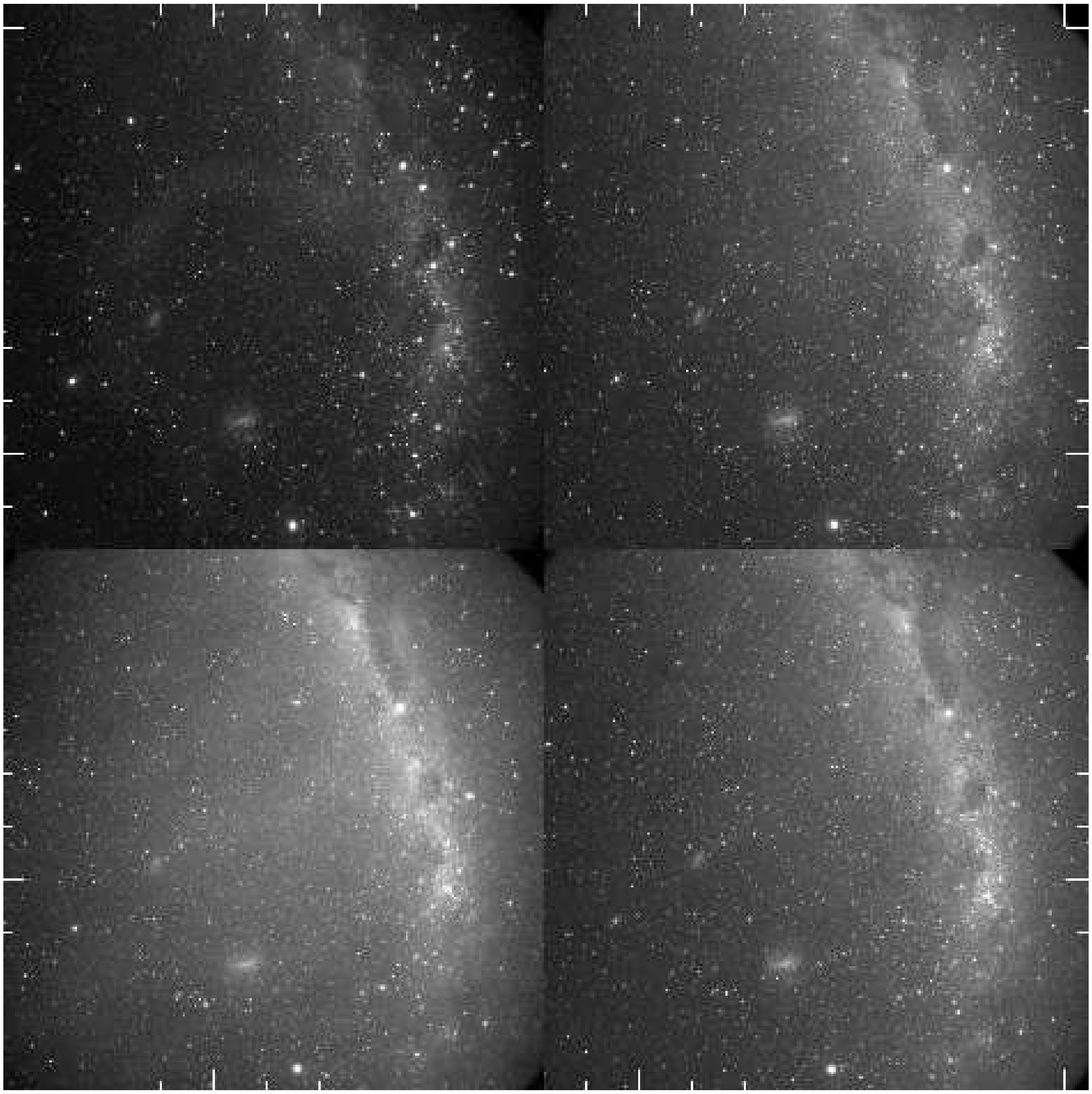

Figure 5.1 Multi-band images obtained by GASC on 21 June 2009. The upper left, upper right, lower right, and lower left panels present the in B-, V-, R-, and OH-band images, respectively. The Milky Way runs from the top middle towards the lower right in each panel, and the LMC and SMC can be identified in lower left quadrant of each panel.

wheel containing Bessell B, V, and R filters (Bessell, 1990). The remaining two slots are for a long pass red filter ($\lambda > 650$ nm) for the study of airglow (OH) emission and an opaque mask for dark current tests.

The heat permits successful operation of the off-the-shelf camera as well as preventing and eradicating ice on the window surface. A conductive indium tin oxide coating was employed on the window surface as a method of de-icing. However, it was found that when operational this was not sufficient to remove ice that was deposited in large amounts due to the surface wind. Some images showed very few sources over small uninterrupted periods of time, ranging from hours up to $\sim$3 days. It is not possible to determine whether the lack of astronomical sources was caused by ice and frost formed on the cover window, or because of the atmosphere. The internal heating was sufficient to keep the window ice-free during the rest of the winter period.

The experiment was controlled by a low-power computer in an electronics rack inside the PLATO module. The continuous observation was operationally simple and repeated this sequence: B-band (100 s and 30 s), V-band (100 s and 30 s), R-band (100 s and 30 s), OH-band as a long pass red filter (100 s and 30 s), 100 s dark, and bias frame. During periods of bright twilight at the beginning and the end of the 2009 winter season, the camera adjusted its exposure time to adapt to the sky counts, or truncated integrations to prevent over-exposure.

5.3.3 The 2009 data set

The full dataset contains approximately 160,000 images obtained from 18 April 2009 to 10 October 2009. Unfortunately, the images obtained before 19 May 2009 were affected by snow over more than one-third of the FOV. Considering the unknown transmission and reflection caused by the anisotropic snow coverage, those images were discarded. Additionally, the sky became continuously bright due to the Sun after 18 September 2009, so we excluded from the data reduction all the images obtained after that date. Images obtained prior to that date, however, with Sun's elevation angle greater than -10° and median count rate above a certain threshold, have also been excluded. Images with a 100 second exposure time have been used to inspect and calibrate the sky brightness. Approximately 11925 frames were obtained in each photometric band for each exposure time between 19 May 2009 and 18 September 2009 ($\sim$ 123 days), resulting in a total of 331.25 hours of 100 s exposures in each filter. The typical cadence for the B, V, and R band 100 s exposure sequences requires $\sim$737 s.

5.3.4 Instrumental effects

GASC was set out to measure the multi-year sky properties of one of the most remote and desolate sites on the planet. Given the nature of the wide field design, combined with an interline CCD and no sidereal tracking system, non-negligible effects needed to be modeled to process the data effectively. These effects are summarized as follows.

5.3.4.1 Absence of a sidereal tracking system

The camera was mounted in a heated enclosure, with fixed pointing in the direction of the SCP. The absence of a mechanical tracking system, together with an extremely large FOV, produces stellar images that exhibit a different Point Spread Function (PSF) at different positions throughout the FOV. Over the course of the 100 s exposures the stars produced elongated circular tracks owing to the Earth's rotation. This effect is most obvious for stars furthest from the exact location of the SCP, which was close to the center of the GASC FOV. The observed largest elongations are $\sim$6 pixels in the X direction and $\sim$6 pixels in the Y direction for each 100s exposure frames.

5.3.4.2 Angle between the optical axis and the south celestial pole

The optical axis of the camera was closely aligned with the SCP, while the horizontal axis of the cover window of the heated enclosure was fixed to be aligned with the zenith. Because stars obtain different zenith angles as a result of the rotation of the Earth, both the optical path length through the material of the cover window and the thickness of the Earth's atmosphere changes with stellar azimuths and elevation angles, introducing a periodic, asymmetrical variation of the stellar light curves, even for stars of constant brightness. Additionally, since the GASC camera was pointing near the SCP, while the cover window was pointing at the zenith, the $\sim 10^\circ$ offset between the SCP and zenith introduced transmission differences as the light passed through the cover window. A schematic of this set-up is presented in Figure 5.2.

5.3.4.3 Vignetting

In large field astronomical images, as well as photography and optics, vignetting causes a reduction of flux at the periphery compared to the image center. In the optical design of GASC, vignetting was necessary to minimize the scattered light from the Moon when it is above the horizon. However, vignetting also significantly reduces both the flux from the stars and from the sky background, especially at the edges of the GASC FOV.

5.3.4.4 Interline transfer sensor

The detector situated behind the multi-band filter wheel is a 2K$\times$2K interline transfer CCD. It has a parallel register that has been subdivided into two stripes to create opaque storage register fits between each pair of columns of pixels. These opaque masks occupy a large portion of the area of the CCD. Although micro-lenses have been annealed to the CCD that focus light from a large area down to the photo-diode, when light beams are incident at large angles, the micro-lens array will fail to direct all the photons directly down

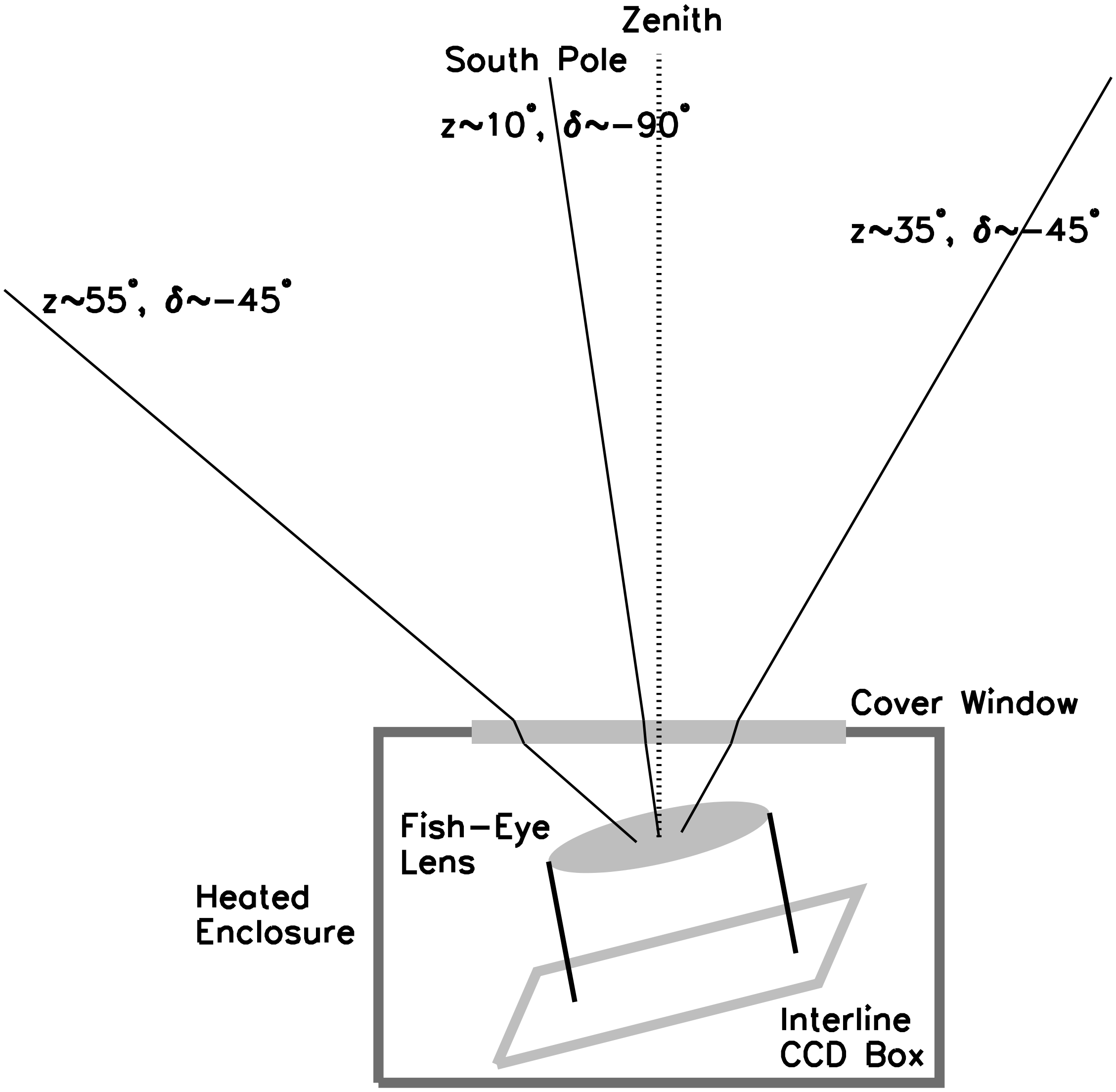

Figure 5.2 Schematic diagram showing the set-up of GASC.

to the photo-diode. For this reason, the CCD is less sensitive to some incident directions of light. As the stars move around the SCP this effect will cause periodic fluctuations in the resulting light curves. The amplitude of those variations is strongly correlated with a star's angular distance from the SCP. For the GASC optical system, this effect can reach ~ 0.2 magnitude. Further test and analysis will be presented in §5.4.4.3.

5.4 Data Reduction

GASC has a large FOV, and the absence of a mechanical system for tracking will lead to star trails on the CCD over the course of the exposures. The instrument is fixed in orientation and stars sweep out circular arcs centered on the South Pole every sidereal day. The illumination response of the GASC across the large FOV is highly variable, at times up to 30% from the center to the edge of the field, due to inherent qualities of the fish-eye lens and due to mechanical baffling introduced to minimize the scattering of light due to the Moon. In addition, there are sidereal variations on the order of 0.2 magnitudes, due to instrumental effects described in §5.3.4. A custom data reduction pipeline is comprised of a set of routines written in IDL that processes the $\sim$11925 raw sky frames for each filter band and produces calibrated sky brightness measurements. The pipeline by necessity also produces calibrated light curves of all the stars brighter than $\sim$7.5 in V. An overview of the essential steps is presented in Figure 5.3. Each step is detailed in the respective sub-section below.

5.4.1 Pre-reduction

The overscan region of each frame was subtracted to remove the consequences of any voltage variations. In each half-day period of observation, a "master bias frame" was made by combining single overscan-subtracted bias frames. For each half-day period of observation, this "master bias frame" has been subtracted from the data frames to remove the internal bias structure across the chip. The internal temperature variations within the

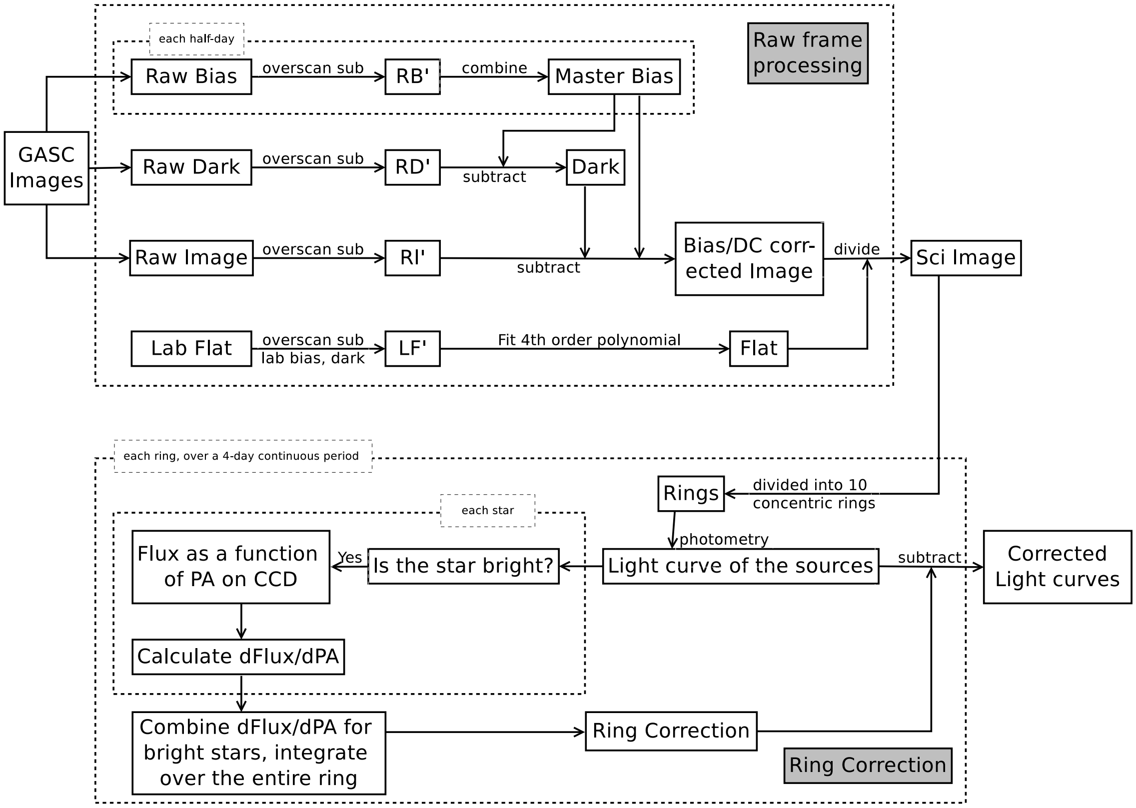

Figure 5.3 Flow chart showing the customized GASC data reduction pipeline.

heated enclosure may lead to implied (and artificial) variations of the sky brightness as well as the photometry of bright targets. We tested the possibility that the enclosure temperature and CCD temperature affect the photometric magnitudes by calculating any possible cross-correlations between the enclosure temperature, the CCD temperature, together with typical light curves for bright stars in the GASC FOV during the entire 2009 winter season. No correlations between any pairs of those factors have been identified, indicating a stable work state of GASC during the 2009 winter season and a reasonable bias subtraction technique.

Acquisition of usable sky flats for this type of system is difficult to perform on the sky, due to the non-tracking capability of the system and the sheer size of the FOV. We measured the flat field illumination properties of the GASC with a uniform illumination screen after the system was returned to Caltech from the Dome A. A multi-band lab flat shows that the optical center of the lens is, fortuitously, coincident with the SCP. For each photometric bandpass, a fourth order polynomial has been directly applied to fit the lab flat. The lab flat was used as a method to remove global transmission variations across the field, whereas, pixel-to-pixel variations were removed by compiling a sky reference flat. The pixel-to-pixel variations turn out to be negligible (less than $\sim 0.3\%$) when compared to the photometric accuracy GASC is able to achieve. However, it was not able to remove the remaining $\lesssim$0.2 mag variations that were removed by the “ring correction” technique, which will be discussed in §5.4.3.

5.4.2 Image profiles and astrometry

The DAOFIND and APPHOT packages within IRAF were used to detect and perform photometry on approximately 2600 bright stars in the GASC FOV, most of which are

---

IRAF is distributed by the National Optical Astronomy Observatories, which is operated by the Association of Universities for Research in Astronomy, Inc., under cooperative agreement with the National Science Foundation (NSF).

between 3.5 to 7.5 magnitude in V. Without tracking, stars trail along concentric rings around the SCP and present elongated, curved PSFs on each frame. Figure 5.4 presents the typical profiles of stars at different distances to the SCP.

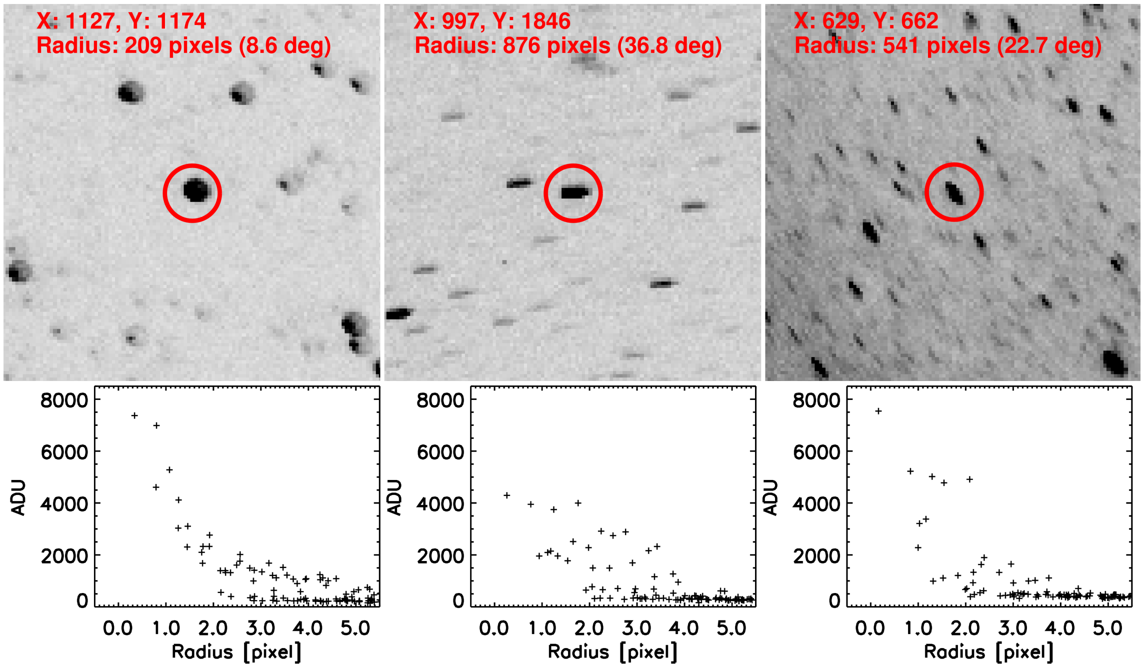

Figure 5.4 Typical profiles of stars at different distances to the SCP.

The astrometry routine adopted in the GASC data reduction pipeline makes use of the almost-polar location of the instrument. We derotated the physical coordinates of the sources in each image relative to known reference images.

To reduce the uncertainty caused by distortion and increase the accuracy of matching, as reference frames we selected 20 high quality frames equally spaced in time over one entire rotation cycle (i.e. one sidereal day). Given the time of exposure of any other frames, all stellar coordinates can be obtained by rotating those 20 templates within ±9 degrees. This provided a time economical solution for performing the astrometry required by the GASC science goals on the ∼36,000 sample images. An overview of the GASC FOV and field stars used to perform aperture photometry is shown in Fig. 5.5.

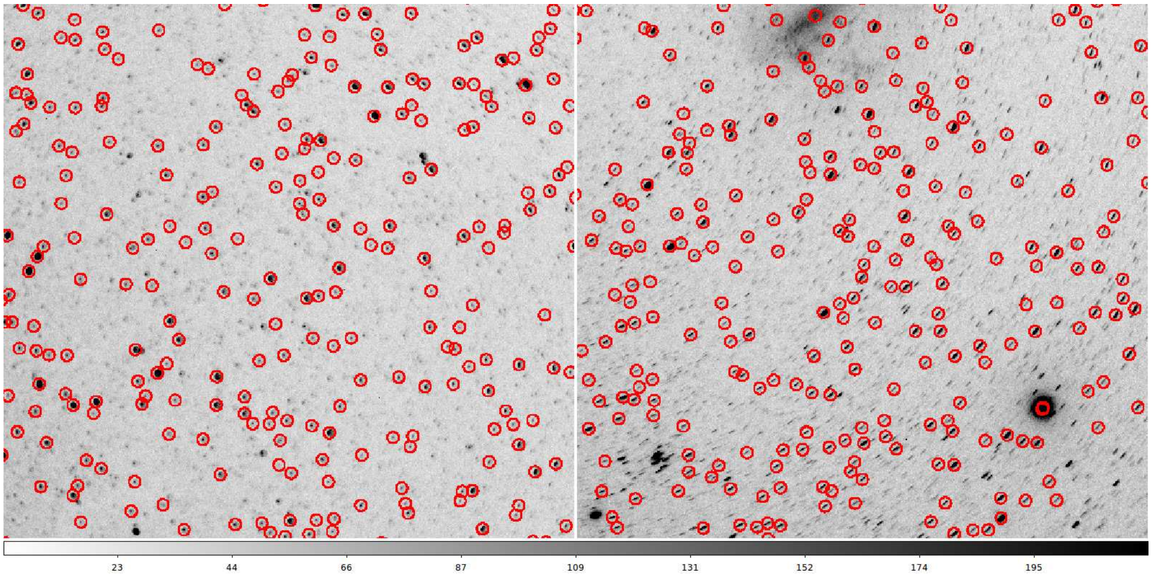

Figure 5.5 The stellar field in the GASC FOV obtained on 22 June 2009. The left panel shows the central FOV and the right panel shows one corner of the FOV. Sources chosen to perform aperture photometry have been circled by $r = 4$ pixel apertures. The images were taken in defocussed mode to account for the huge pixel scale. The right panel shows significant star tracks near the corner of the FOV due to the Earth's rotation.

5.4.3 Ring correction

Due to the combined effect of the presence of the cover window and the different response of the interline transfer CCD to different incident angles, light curves for ~ 2600 stars imaged in the GASC FOV show asymmetrical sidereal fluctuations. The amplitude of this variation grows as the distance of stars to the SCP increases. We looked at the behavior of bright, isolated stars which sweep out concentric rings in the GASC FOV. As the "standard stars" have higher S/N, a weighted combination of their light curves gives us feedback on the entire optical system. This feedback, however, also applies for all the other stars with a lower S/N.

Here we introduce a “ring correction” to remove the residual instrumental effects, to the order of ± 0.2 mag in the raw photometry. The methodology is to consider the features of the light curves for bright stars that have similar distances from the SCP, as they sweep out paths along the same ring with different hour angles but similar declination. The systematic light curve features do not change drastically at slightly different radii. The GASC FOV has been subdivided into 10 concentric rings, each with a width of 100 pixels, with an exception of 60 pixels for the outermost ring. Figure 5.6 shows the concentric rings dividing the GASC FOV. Within each ring we investigated the behavior of standard stars which are non-variable stars with $V \sim 3.5 - 5.5$, mapped the gradient of its flux variation over different position angles (PA) on the CCD chip relative to the SCP, i.e., $\mathrm{d}Flux/\mathrm{d}PA$. Then, we combined the gradients calculated from each standard star at each PA over a continuous run of observations under good weather conditions, and applied a spline interpolation to obtain a gradient map over that ring. We then integrate over the PA and convert the integrated flux into a magnitude. This produces a phase diagram of magnitude variations within each ring, representing systematic behavior of the stars as they trail along certain rings of the CCD chip.

We refer to this procedure as the “ring correction”. The light curve corrections for all the other stars can be obtained by subtracting the “ring correction” after proper time phase matching. The “ring corrections” have been built based on a 4-day continuous run of high-quality data obtained from 04:25 UT on 22 June 2009 to 03:47 UT on 26 June 2009. This has been applied successfully to the data obtained during the entire season. The “ring corrections” for typical stars within each one of the ten rings are shown in Fig. 5.7, and they work well for most of the cases. Additionally, the $\sigma -$ magnitude diagram, after applying both the pseudo-star correction and the ring corrections is shown in Fig. 5.8.

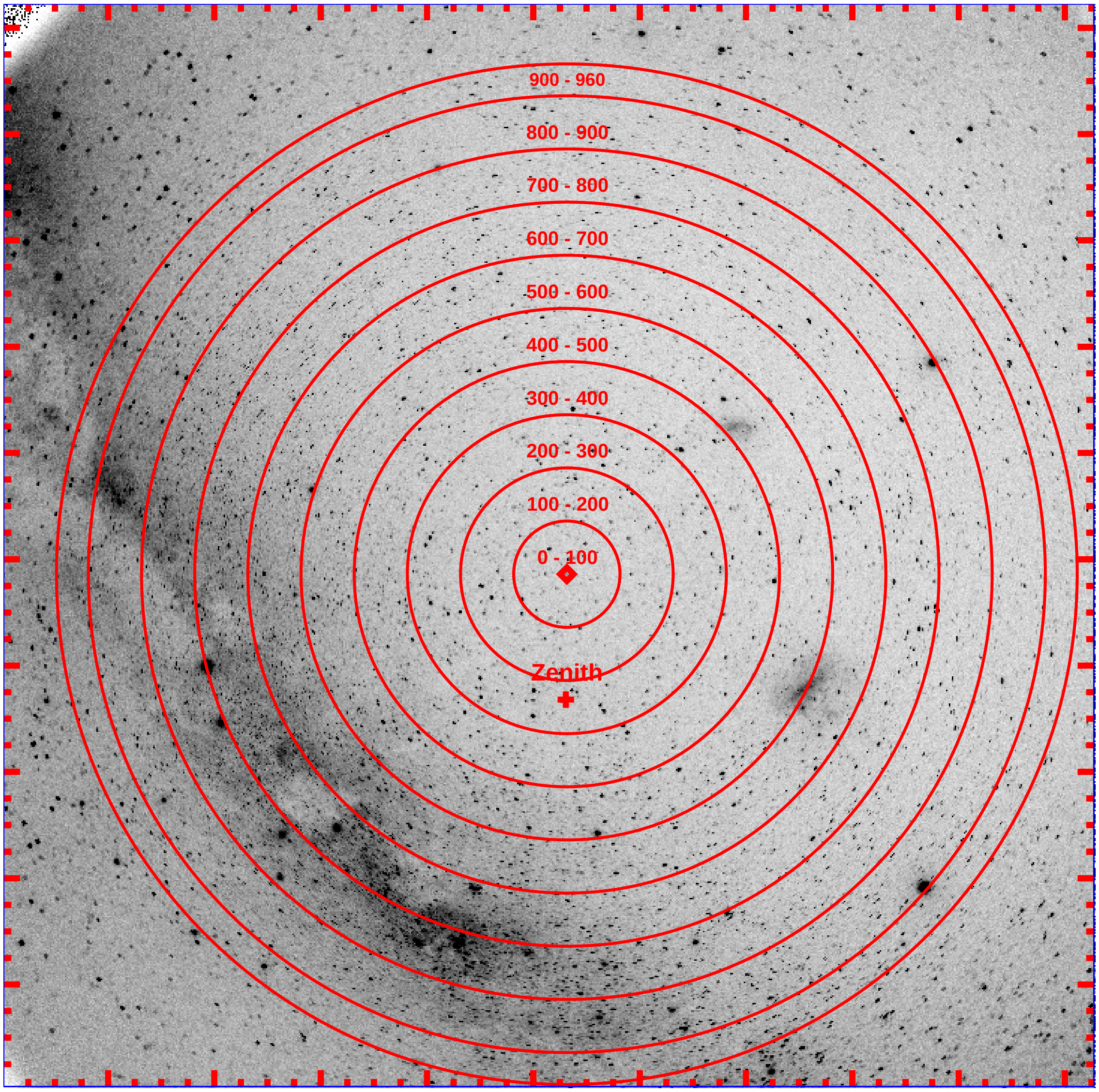

Figure 5.6 Concentric rings dividing the GASC FOV. The + marks the physical position of the zenith on the GASC FOV.

For instance, we obtained $\sim 3\%$ photometric accuracy for stars with apparent magnitude $V \approx 5.5$. In summary, with the ring correction procedure completed, the light curves have been corrected for instrumental effects that cause intensity variations across the field and as a function of time.

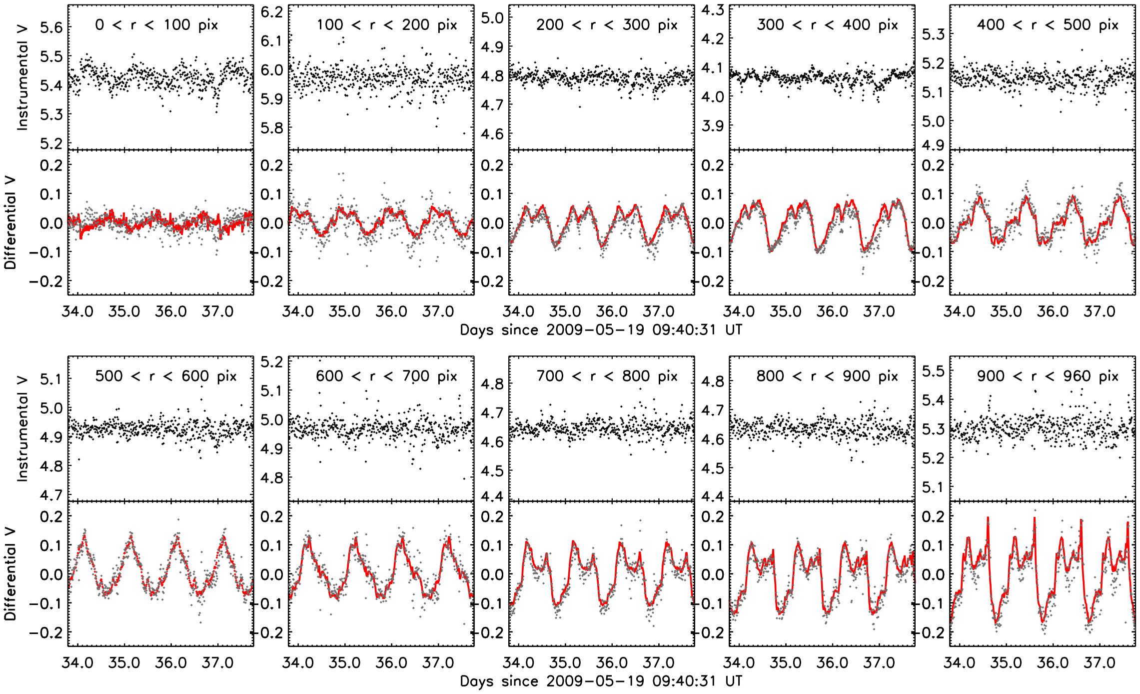

Figure 5.7 The "ring corrections" for V-band light curves for 10 different annuli are shown as 10 sub-figures. Each panel represents an annulus width of 100 pixels in radius. The upper sub-panels represent the output light curves after applying the ring corrections. In the lower sub-panels, the gray dots represent the input light curves before applying the corrections, and the red symbols represent the models of corrections within each corresponding radius range.

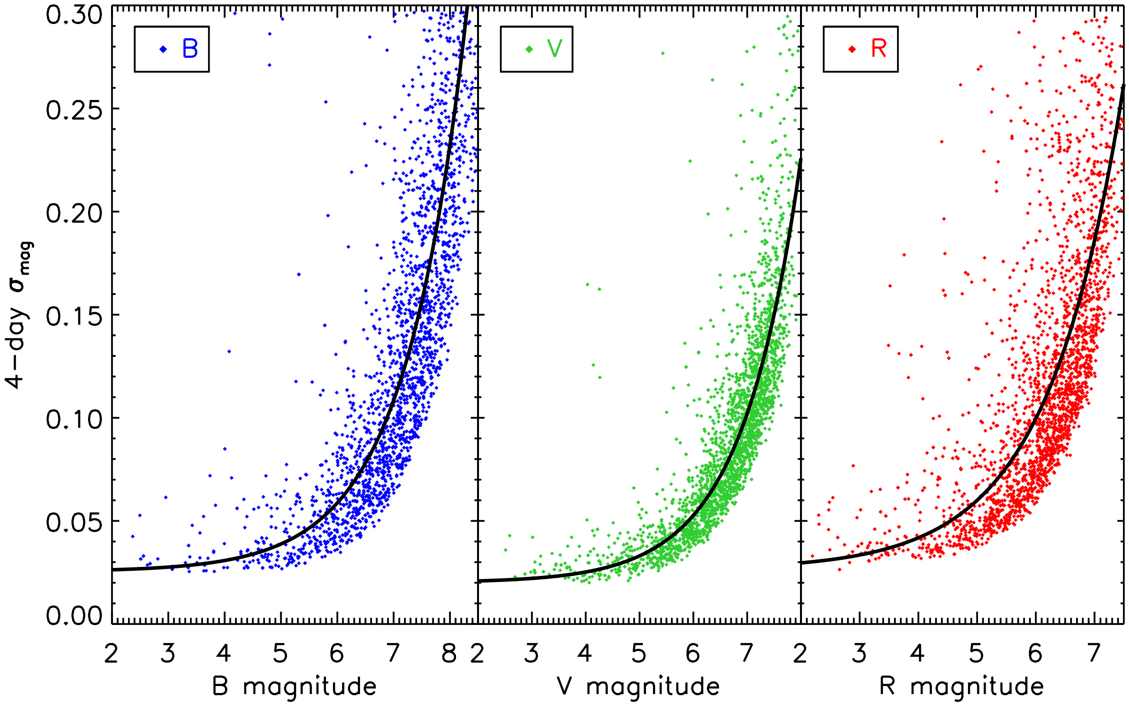

Figure 5.8 Photometric errors vs. stellar brightness. From left to right we show the photometric accuracy in the Bessell B-, V-, R-bands, respectively, after applying the “ring corrections.” The photometric uncertainties were calculated from data obtained on 4 consecutive days.

5.4.4 Calibration for sky brightness

5.4.4.1 Determination of catalog magnitude

This step of the GASC data reduction pipeline converts instrumental magnitudes to catalog magnitudes. Furthermore, the sky brightness can be determined by applying this offset to the GASC measured sky flux. If we define the "radius" of each star as its distance from the SCP (pixel coordinates X = 1063, Y = 972), we find that the amplitude of the daily fluctuation in a star's light curve depends on (1) its radius, (2) observing bandpass, as shown in Fig. 5.9, together with (3) the mean value of the difference between the standard star's catalog and instrumental magnitude. As radius increases, the more stable is the mean difference between a standard star's catalog and instrumental magnitude, and the less affected the standard star's flux is due to instrumental effects.

The upper panel in Fig. 5.9 shows a stable trend of the mean difference between standard stars' catalog and instrumental magnitudes in the V- and R-bands, which means that as stars travel around in the GASC FOV, though the distance to the SCP varies for different stars, it is still reasonable to treat the brightest magnitude in one cycle as the true instrumental magnitude of that star. Instrumental effects become more significant near the edges of the FOV. Strong geometrical distortions, as well as the large incident angle near the edges of the FOV, will cause an unexpected and non-negligible reduction of the flux transmitted through the optical system. Giving special consideration to the case of the B- and V-bands, we set a cutoff radius of 700 pixels, corresponding to $\sim 30^\circ$ from the SCP, and we use all the standard stars within this radius to calibrate the sky brightness.

We rely on the linearity of the CCD and minimize the χ^2 value of the fit using the offset between the standard stars' photometric magnitudes and their catalog magnitudes. We consider data only within 700 pixels of the SCP and weight by the area of each ring. This gives us our multi-band sky brightness measures at Dome A calibrated by the standard

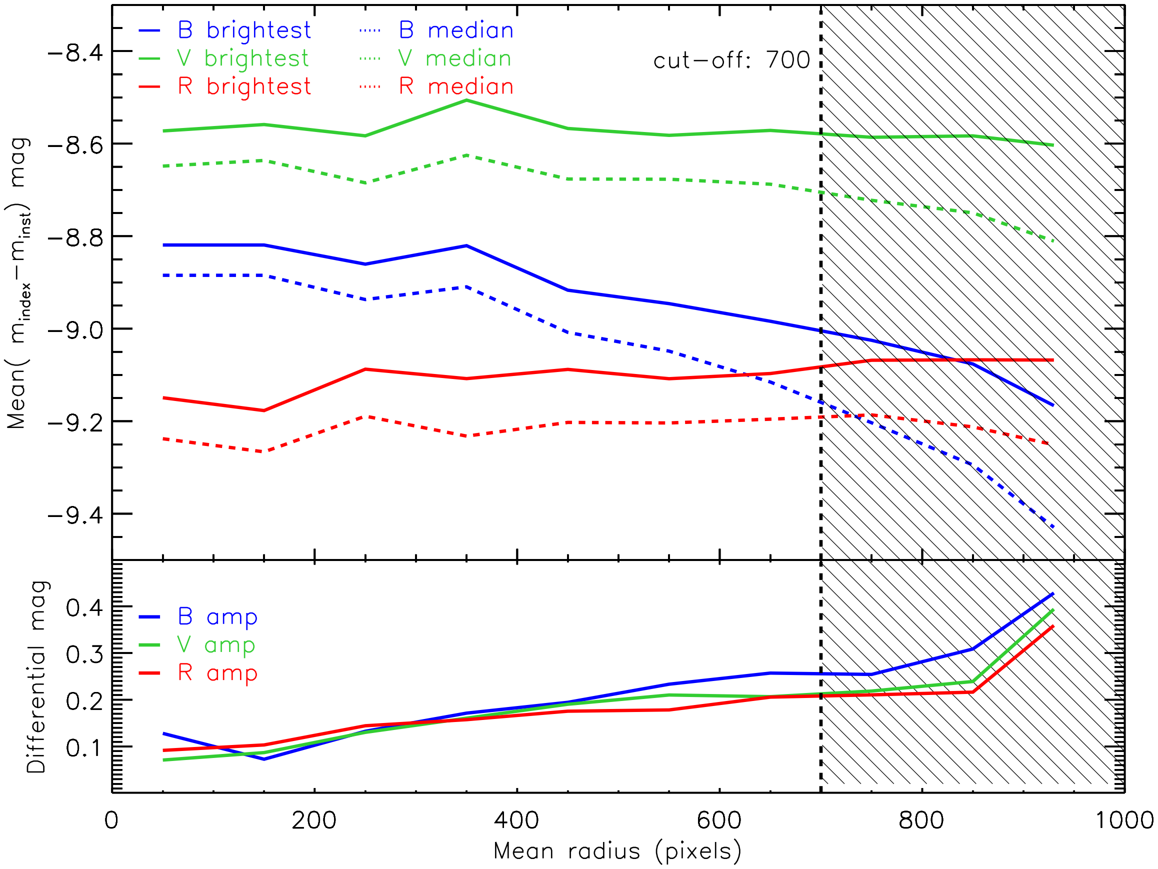

Figure 5.9 A radius-magnitude offset diagram for the “ring correction” for different radii. The offset between standard stars’ catalog magnitude and instrumental magnitude has been calculated based on two different considerations of instrumental magnitude. The results are based on the median values of all the standard stars’ brightest (represented by solid lines) and median (represented by dashed lines) magnitudes during a sidereal day. The lower panel shows radius-amplitude diagrams for the “ring correction” in different annuli. A significant increase in amplitude occurs if the radius is increased from 700 pixels to 800 pixels. A vertical dashed line and the shaded region indicate the 700 pixel radius cut-off for stars to be used for calibration.

Table 5.1. Calibration models

Band	Dome A median mag	Dome A brightest mag	Palomar
B	$\mathrm{m}_{inst} - 9.02$	$\mathrm{m}_{inst} - 8.92$	$\mathrm{m}_{inst} - 9.52$
V	$\mathrm{m}_{inst} - 8.67$	$\mathrm{m}_{inst} - 8.56$	$\mathrm{m}_{inst} - 9.00$
R	$\mathrm{m}_{inst} - 9.21$	$\mathrm{m}_{inst} - 9.10$	

stars. Once GASC was shipped back to Caltech, we performed tests at Palomar Observatory. Table 5.1 gives the BVR photometric offsets from instrumental to calibrated values. The details of the Palomar GASC test are discussed in the next section. The offset in the constant term between the Palomar and Dome A calibration model was due to the absence of the cover window in the Palomar test and the different exposure times between two observation epochs.

5.4.4.2 Determination of photometric conditions

Variations of global transparency, including weather changes, possibly snow and frost formed in front of the enclosure's cover window, will dramatically affect many quantities in measuring sky brightness, the fraction of the sky covered by cloud, as well as photometry of bright sources. This global effect can be subtracted off by introducing a "pseudo-star", with a count rate f^p and instrumental magnitude $m^p = -2.5 \times \log_{10} f^p$, which has been constructed from the observed counts of 2600 target stars in each frame according to:

$$f_i^p = \sum \frac{f_{i,j}}{(\sigma_j^{ring})^2 + (\sigma_{i,j})^2} \ , \ \ m^p = -2.5 \times \log_{10} f^p + ZP^P \tag{5.3}$$

where i is the frame number in the observing sequence and j is the star number in each frame. σ_j^{ring} gives the standard deviation of the residuals in counts for the j^{th} star after the ring correction during the 4-day continuous run of high-quality data obtained from 04:25

UT on 22 June to 03:47 UT on 26 June, $\sigma_{i,j}$ gives the measured photometric error for the j^{th} star in the i^{th} observation, ZP^P is the zero point for instrumental magnitude and assigned to be 25. We subtract m^p from the rough photometric results to remove the global variations in the entire GASC FOV. Furthermore, the variation of the pseudo-star can be an indicator of transparency variations and further used to estimate the cloud coverage. A more detailed discussion will be presented in the following sections.

5.4.4.3 GASC Test at palomar observatory

To test the quality of GASC measurements and the calibration of sky brightness, another experiment intended to measure and calibrate the sky brightness at an astronomical site was implemented at Palomar Mountain Observatory. The sky at Palomar during a moonless night is sufficiently dark to check the Dome A measurements. The Palomar Night Sky Brightness Monitor (NSBM) allows a real-time comparison between the night sky brightness measured by the two different instruments. The Palomar NSBM consists of two units deployed at Palomar Observatory. A remote photometer head and a base station receive data from the remote head via a wireless spread-spectrum transceiver pair. The remote head has two photometers that sample areas of the sky $\sim 5.6^\circ$ in diameter at two elevation angles. The photodetectors used to measure the sky brightness receive filtered light to define a spectral response centered in the visual range, with a strong cutoff in the near infrared.

One unit of the NSBM uses a 1.5-cm diameter photodetector, which measures the brightness of the sky $\sim 5.6^\circ$ in diameter at the zenith. Without rejecting stellar contaminants the mean value for this region is taken to represent the night sky brightness. The output data from the NSBM consists of the measured frequency and ambient temperature

---

http://www.sao.arizona.edu/FLWO/SBM/SBMreport_McKenna_Apr08.pdf of each sensor. The sky brightness is calculated as:

$$Zenith\,magnitude \;=\; -2.5\,\log_{10}(Zenith\,reading - 0.012) \;+\; ZP\;. \tag{5.4}$$

The detector output frequency (in Hertz) constitutes the raw data, as the NSBM uses a light to frequency converter. The dark frequency to be subtracted for the zenith is 0.012 Hz. The zero point of the NSBM system adjusted to the National Parks System from one night's data (4 July 2013), is 19.41 mag arcsec^{-2} and for a band comparable to the Johnson V-band is 18.89. Fig. 5.10 shows the time variations of the sky brightness measured by NSBM and GASC. The sky brightness measured by two different instruments, with two completely different calibration methods agrees overall to ~ 0.12 mag arcsec^{-2}.

A separate test was conducted at Palomar to show that the camera orientation, specifically the azimuth angle of the camera, results in a variation in the magnitudes of bright stars. This test used exposures taken very close to one another in time. The results of this test confirmed the variations we see in the original data.

5.5 Results and Discussion

5.5.1 Sources of sky brightness

Artificial light pollution is essentially nonexistent at Dome A, Antarctica. The main contribution to the sky background is usually from the atmospheric scattering of the light from the Sun and the Moon. At Dome A (80° 22′ S, 77° 21′ E) there is some twilight time even on the first day of the southern winter, as the Sun is roughly 13.8° below the horizon at local noontime. The closer the Sun is to the horizon at local noontime on other days of the year, the greater will be the variation of the sky brightness, even on days when the Sun does not rise and set.

Zenith readings are available at: http://www.palomar.caltech.edu:8000/maintenance/darksky/index.tcl

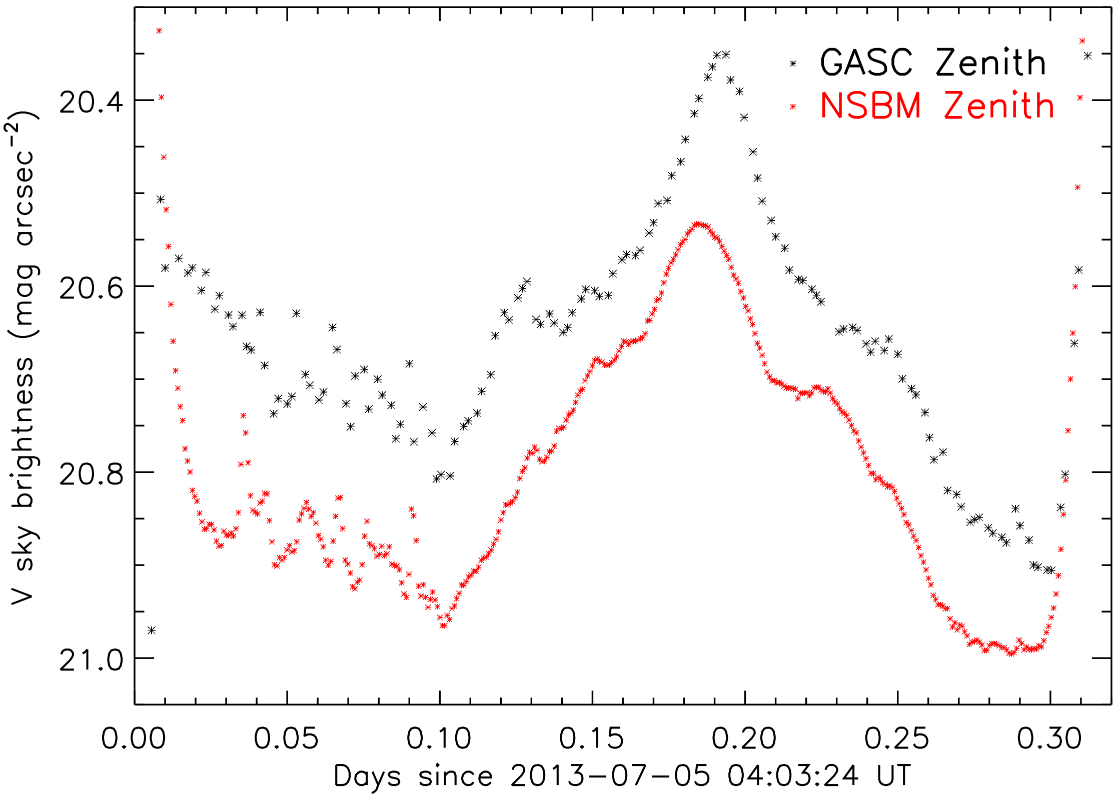

Figure 5.10 Palomar night sky brightness measured and calibrated by NSBM (red dots) and GASC (black dots) on UT 05 July 2013.

Airglow persistently provides photon emission and gives the dominant component of the optical and near-IR night sky brightness (Benn & Ellison, 1998). The Antarctic sites such as Dome A, however, are particularly prone to aurorae that can be extremely bright in the optical passbands. Broadband filters and low resolution spectrographs covering the auroral lines are sufficiently likely to be contaminated by strong emission lines from aurorae, i.e., the N_2 second positive (2P) and N_2^+ first negative (1N) bands dominating the U and B bands, the [O I] 557.7 nm emission dominating the V band, and the N_2 first positive (1P), N_2^+ Meinel (M) and O_2 atmospheric bands dominating the R and I bands (Gattinger & Jones, 1974; Jones & Gattinger, 1975). Customized filters or spectrographs with a moderately high resolving power can minimize the contamination from aurora and airglow emissions. We refer to Sims et al. (2012b) for a more comprehensive review of airglow and aurorae as dominant sources of sky brightness in Antarctica sites.

Diffuse light from the Milky Way Galaxy could also contribute to the sky brightness. The Galactic Latitude b of the SCP is $-27^\circ.4$, and part of the Galactic plane was included in the GASC FOV. The plate scale of GASC is approximately 147″ per pixel, and the sub-pixel stellar contamination needs to be calculated and removed from the measured sky brightness data. Airglow, zodiacal light, and aurorae also contribute to the sky brightness. The intensity and frequency of occurrence of aurorae depend upon the solar activity. Rayleigh (1928) and Rayleigh & Jones (1935) were the first to note a correlation between the sky brightness and the 11-year solar cycle. This is due to the airglow being brighter at solar maximum and fainter at solar minimum (Krisciunas, 1997; Krisciunas et al., 2007). The 10.7-cm radio flux of the Sun is widely used as an index of solar activity. The 2009 winter season occurred during solar minimum, so the sky at Dome A should have been as dark as other sites at solar minimum, or $B \approx 22.8$ mag arcsec^{-2} and $V \approx 21.8$ mag arcsec^{-2}. We do not expect that the Dome A measurements of 2009 are significantly affected by auroral events.

An approach to determine the sky brightness and estimate the cloud cover is given in the following subsections. Due to the extremely wide FOV and the fisheye optical design of GASC, scattered light from the edges of the optical system, as well as the reflection and refraction inside the optical system, is inevitable. The actual contribution from the Sun and the Moon cannot be well modeled when the sky becomes too bright. A rough model of the Sun and the Moon's contribution to the sky brightness will be discussed.

5.5.2 GASC measurements of sky brightness

The sky brightness is transformed from analog-to-digital units (ADU) into units of mag arcsec^{-2} for each photometric band. The GASC instrumental magnitude is defined as:

$$m_0 \; = \; 25 - 2.5 \, \log_{10}(\mathrm{ADU}) \tag{5.5}$$

The sky brightness in units of mag arcsec^{-2}, which varies from band to band, can be defined as:

$$S_\lambda \; = a \; + \; b \times [25 \; - \; 2.5 \times \log_{10}(\mathrm{ADU}/\mathrm{pix}^2)] \tag{5.6}$$

Where "pix" is the pixel scale in unit of arcsec pixel^{-1}. The constant term in the linear calibration models is a, and the coefficient scaling the instrumental magnitude is b. In a certain sky region we wish to calibrate, we draw a box and investigate the statistics of the ADU values amongst all the pixels inside. We choose the 'mode' value to best represent the sky brightness which is a more stable measurement as it is less affected by contamination from the bright sources, the wide-spread PSF of stars due to the GASC optical system, and other unexpected events such as bright local aurorae. However, even the smallest pixel scales in GASC are 147.3 arcsec pix^{-1} near the center of the FOV, corresponding to a box of 2.5$'$ $\times$ $2.5'$ on the sky. The measured sky brightness will inevitably be contaminated by the unresolved faint sources.

We looked at several small regions which lack bright sources to reduce the effect of stellar contamination. For instance, a box centered at RA = 2^h24^m, DEC = $-86°25'$ and 25×25 pixels in size ($\sim 1° \times 1°$) was inspected. The B-band and R-band magnitudes of 9550 stars in this region were obtained from the USNO-A2.0 catalog. We estimated a stellar contamination of 24.14 mag arcsec^{-2} in the B-band. Using a mean V-band contamination of 23.31 mag arcsec^{-2} and a calculated median color of $V - R$ = 0.4 mag based on the catalog from Landolt (1992), we estimated the R-band contamination to be 22.91 mag arcsec^{-2}.

Fig. 5.11 shows the sky brightness variations during the 2009 observing season. At such a southerly latitude as that of Dome A, the Moon is always fairly full when it is above the horizon from April to August, leading to a strong correlation between lunar elevation and sky brightness (Zou et al., 2010). There is a monthly variation of sky brightness which is strongly correlated with the lunar elevation angle. The GASC sensitivity did not allow data acquisition when the sky brightness was above a certain threshold. A dramatic enhancement in the sky brightness can be identified by looking at the data obtained late in the 2009 winter season. Fig. 5.12 is a zoomed in plot for four consecutive days during the midwinter of 2009. In Fig. 5.13, the Moon's contribution is negligible when it is more than 7° below the horizon. However, a variation of the sky brightness of more than 1 mag arcsec^{-2} can be identified which shows a strong correlation with the Sun's elevation angle.

5.5.3 Comparison with sky brightness at palomar

Additional tests of GASC were conducted at Palomar Observatory. The "ring correction" to light curves and the fitting of calibration models only works based on an entire cycle of the track of the stars. This allows the determination of the position within a ring where stars are least affected by instrumental effects. Though it is not feasible to find the

---

Geographical coordinates of Palomar Observatory: latitude $33° \; 21' \; 21''$ N, longitude $116° \; 51' \; 50''$ W.

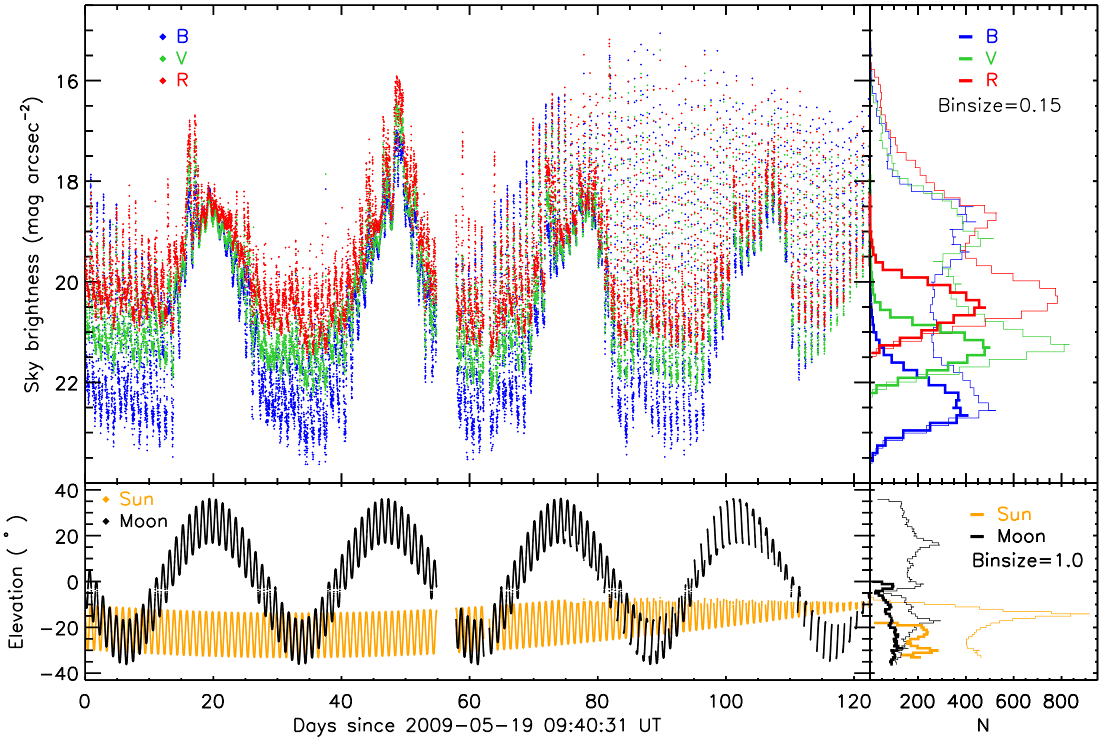

Figure 5.11 Multi-band sky brightness within a 1 square degree region near the SCP, as well as the Sun's and Moon's elevation during the 2009 winter season. The upper and lower left panels present the time series while the top and bottom right-hand panels show the histograms. The results for the Bessell B-, V-, and R-bands are represented by blue, green, and red symbols, respectively. In the right panels, the histograms with solid thick lines represent the statistics for sky brightness during dark time, when the solar elevation angle is less than $-18°$ and lunar elevation angle is less than $0°$. Stellar contamination has already been removed by subtracting the contribution of a total of 9550 stars in the inspection area. Their magnitudes were obtained from the USNO A-2.0 catalog.

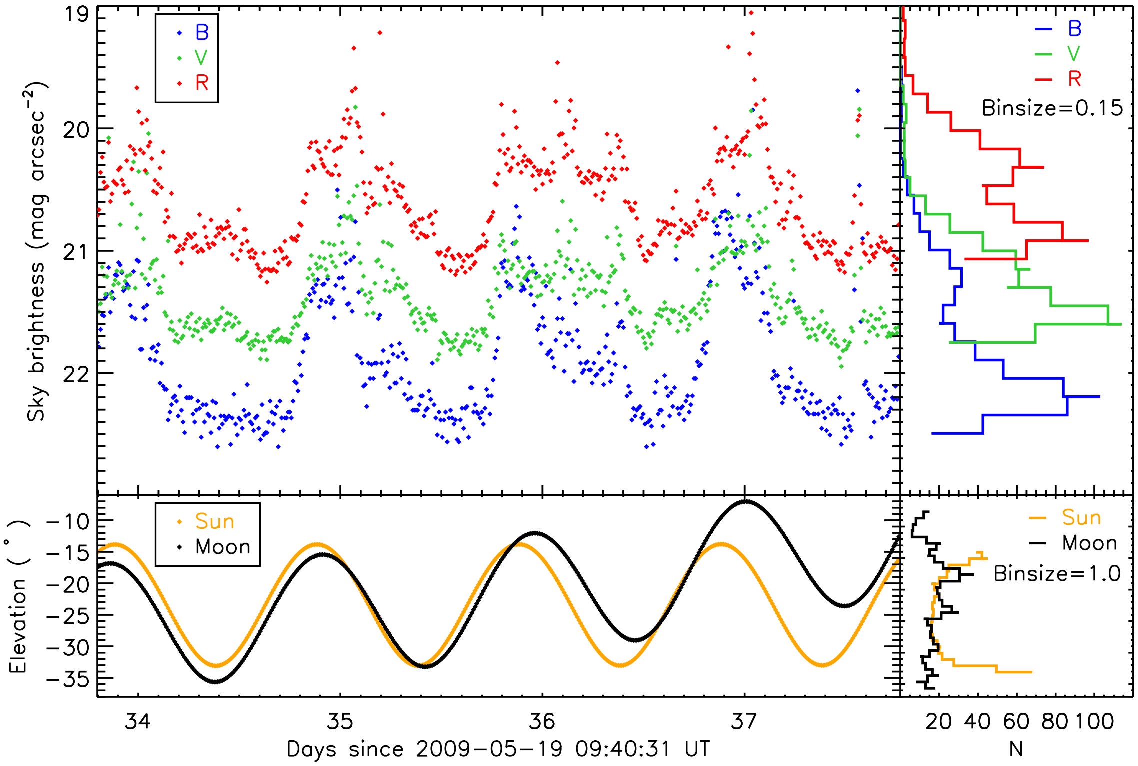

Figure 5.12 A four-day subset of data shown in Fig. 5.11, from 04:25 UT on 22 June 2009 through 03:47 UT on 26 June 2009. When the Moon is many degrees below the horizon, the daily variation of sky brightness is dominated by the elevation of the Sun.

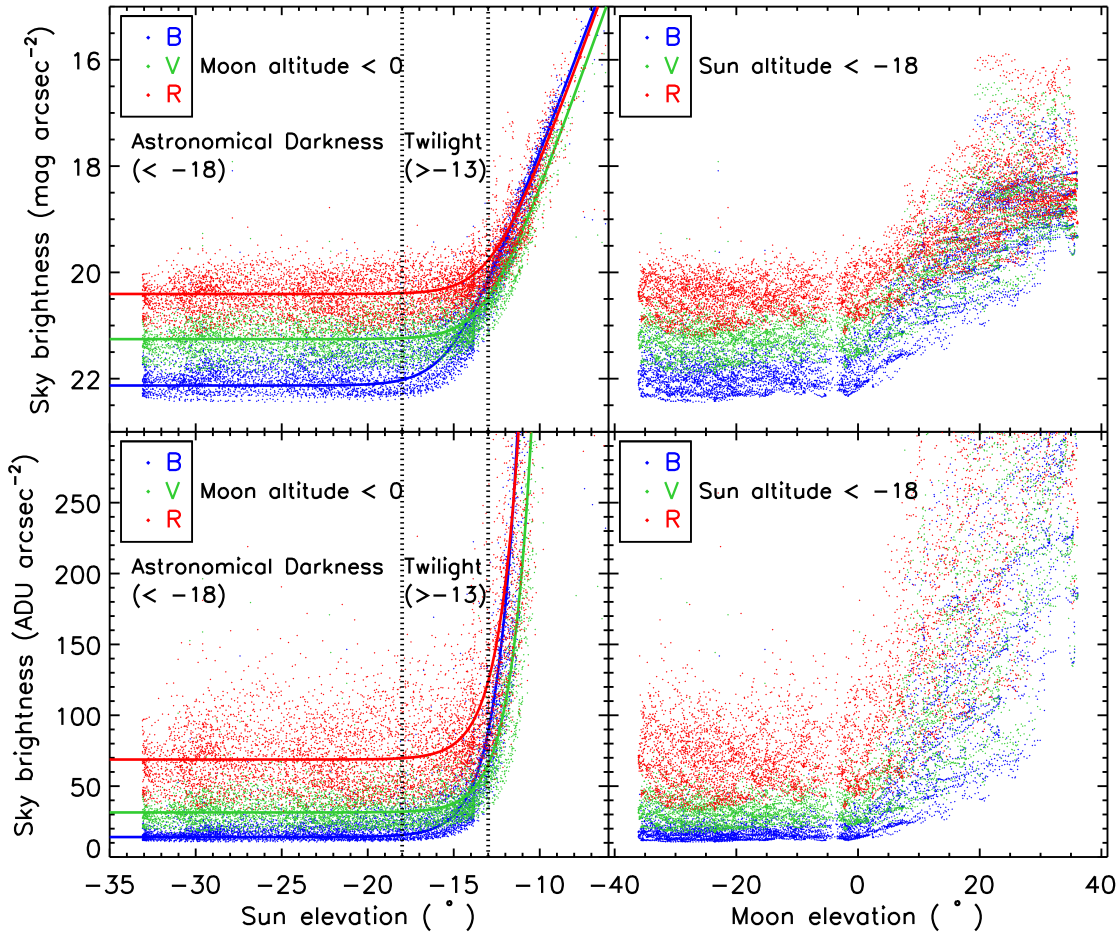

Figure 5.13 Multi-band sky brightness vs. the Sun and Moon elevation. The upper panels show the measurements in mag arcsec^{-2} while the lower panels show the data as ADU's per square arcsec. The left-hand panels show the relation between the sky brightness and the elevation angle of the Sun together with the model from Equation 5.7. Only the data with Moon elevation less than 0° have been included. The right panels show the relation between the sky brightness and the elevation of the Moon. Only the data with Sun elevation less than -18° have been included.

maximum transmission for each star cycle from tests at Palomar, we can still point GASC near the zenith and obtain different calibrations based on the instrumental magnitudes measured by GASC and the corresponding catalog magnitudes.

On 5 July 2013, GASC arrived at Palomar Observatory and was reassembled. Two tests were carried out. The first test was to compare GASC-measured sky brightness with Palomar NSBM measurements. We pointed the GASC at the zenith and set the exposure time to 50 seconds for the Bessell B, V, and R filters. The calibration was carried out based on single frames of high image quality for each bandpasses. We used the instrumental magnitudes of the standard stars in one single high-quality frame per filter taken under photometric conditions. This is different than the method used for data obtained at Dome A, where the brightest instrumental magnitudes over the course of a day were adopted as the throughput of the system.

For each star in the FOV of each single exposure, the orientation of its maximum transmit position on the CCD chip is randomly distributed. In order to compare the Palomar calibration with the calibration of Dome A data (whose calibration models have been based on the standard stars' maximum transmitted flux), we performed another calibration of Dome A data, based on the median instrumental magnitude of each standard star as it tracks during one daily cycle to simulate the calibration that use the stars' flux at random positions like the Palomar test. By treating either the brightest or the median magnitude of standard stars along complete circles in Dome A data as the instrumental magnitude, an intrinsic offset of $(-8.670) - (-8.564) = -0.11$ magnitude is obtained due to the different measures of instrumental magnitude. The difference in the V-band median sky brightness on the night of 5 July 2013 UT at Palomar Observatory, as measured by NSBM and GASC, was $(20.880 - 20.653) = 0.23$ mag arcsec^{-2}. Thus, GASC and NSBM agree

---

For the measurements at Palomar we note a roughly 0.5 mag arcsec^{-2} variation of the sky brightness over the course of the night due to the band of the Milky Way passing overhead.

within -0.11 + 0.23 = 0.12 mag arcsec^{-2}, and the “ring calibration” method gives a reasonable calibration for the GASC data.

Usually, inland astronomical sites are affected to some degree by artificial light pollution from populous cities. The sky brightness as a function of elevation angle obtained from the Tucson lab sites shows that there is a significant difference in sky brightness between the zenith and 20° elevation (McKenna, 2008). At Cerro Tololo Inter-American Observatory the V-band sky brightness deviates from the model of Garstang (1991) due to light pollution at elevation angles of $\lesssim 10^\circ$ in the direction of La Serena (Krisciunas et al., 2010). Without accounting for stellar contamination, Table 5.2 presents the median sky brightness for different regions at Dome A, Antarctica, during the 2009 winter season, both for the dark time and whole season (the values within parentheses). Five concentric circular areas, of increasing radius and centered at the SCP, were inspected. Though the regions were centered at the SCP instead of the zenith, the approximate 10° offset has been ignored. From Table 5.3, no significant increase in brightness can be identified as a function of increasing angular radius. This indicates that within 30° of the SCP there is dark sky that remains roughly constant in brightness.

5.5.4 Sun and moon model

Liu et al. (2003b) modeled the relationship between the sky brightness and the phase and elevation angle of the Moon. Independent to the scattering of light caused by reflection and refraction in the GASC optical system, the B-, V-, and R-band data should exhibit the same functional form relating to the Sun’s and Moon’s effects. We can write:

$$F_{Sun} \;=\; a10^{b\theta} \;+\; c\,, \tag{5.7}$$

where F$_{Sun}$ gives the sky flux when the Moon’s contribution is negligible, and a, b, and c are constants determined for different bandpasses, θ is the elevation angle of the Sun. The

Table 5.2. Sky brightness for different percentage of time value[a]

Band	Value[b]	80%	50%	20%	10%	5%
B	mode	21.68 (19.17)	21.99 (20.91)	22.22 (21.95)	22.31 (22.15)	22.37 (22.26)
	subtracted	22.01 (19.20)	22.45 (21.06)	22.82 (22.40)	22.98 (22.70)	23.10 (22.90)
	corrected	22.13 (19.32)	22.57 (21.18)	22.94 (22.52)	23.10 (22.83)	23.22 (23.02)
V	mode	20.93 (19.05)	21.22 (20.61)	21.48 (21.24)	21.59 (21.43)	21.67 (21.56)
	subtracted	21.07 (19.08)	21.40 (20.70)	21.72 (21.42)	21.86 (21.65)	21.96 (21.81)
	corrected	21.19 (19.20)	21.52 (20.83)	21.84 (21.54)	21.98 (21.77)	22.08 (21.93)
R	mode	20.13 (18.69)	20.44 (19.91)	20.75 (20.49)	20.90 (20.70)	20.99 (20.85)
	subtracted	20.21 (18.71)	20.56 (19.98)	20.91 (20.61)	21.68 (20.85)	21.20 (21.03)
	corrected	20.34 (18.54)	20.68 (20.10)	21.03 (20.73)	21.02 (20.97)	21.15 (21.32)

[a] Values without parentheses are for dark time. Values in parentheses are for the whole season.

[b] mode: the ‘mode’ value amongst all the pixels inside the inspected region; subtracted: the ‘mode’ value subtracted for the stellar contaminations; ‘corrected’: the ‘subtracted’ values further corrected for the offset between the GASC and Palomar NSBM.

Table 5.3. Mode of sky brightness for regions of different angular size[a]

Diameter (deg)	B	V	R
4.6	21.92 (20.41)	21.16 (20.25)	20.40 (19.65)
20	21.90 (20.40)	21.16 (20.27)	20.39 (19.66)
40	21.90 (20.41)	21.17 (20.30)	20.40 (19.69)
60	21.96 (20.46)	21.24 (20.37)	20.47 (19.77)

[a] Values without parentheses are for dark time. Values in parentheses are for the whole season.

multi-band sky brightness has been fitted with a nonlinear least-squares method using the images with good transparency and negligible contributions from the Moon.

The model for the sky surface brightness due to the Moon's contribution involves factors such as the Earth-Moon distance and the Moon's phase. Following Liu et al. (2003b), the apparent magnitude of the Moon can be approximated by this empirical formula:

$$V(R, \Phi) \; = \; 0.23 \; + \; 5 \, \log_{10} R \; - \; 2.5 \, \log_{10} P(\Phi) \; . \tag{5.8}$$

where R is the Earth-Moon distance in astronomical units, Φ is the lunar phase angle, and $P(\Phi)$ is the function of the full Moon luminance. Following Zou et al. (2010), we apply the same approach for the sky surface brightness contribution by the Moon. F_{Moon} can be expressed as a form of Equation 5.7 multiplied by the Moon phase factor $P(\Phi)$. Then,

$$F_{Moon} \; = \; AP(\Phi) 10^{B\Theta} \; + \; C \; , \tag{5.9}$$

where Θ is the elevation angle of the Moon and A, B, C are constants determined for each bandpass. For a more refined but slightly complicated sky brightness model one can consult Krisciunas & Schaefer (1991). The multi-band sky brightness has been fitted with a nonlinear least-squares method using images with good transparency and negligible contribution from the Sun. The models for the Sun's and the Moon's effect are shown in Table 5.4.

5.5.5 Astronomical twilight

When the Sun sets, civil twilight occurs, by definition, when the Sun is 12° below the horizon. Astronomical twilight ends when the Sun reaches 18° below the horizon. If the sky brightness changes when the Sun is further below the horizon, it is due to changes in the airglow contribution, aurorae, or stellar contamination. However, the definition of

Table 5.4. Sun and moon models for sky brightness

Band	Sun model	Moon model
B	$\mathrm{F_{Sun}} = 2.076 \times 10^6 \times 10^{0.342\theta} + 16.283$	$\mathrm{F_{Moon}} = 118.098 \times \mathrm{P}(\Phi)10^{0.017\Theta} - 18.544$
V	$\mathrm{F_{Sun}} = 1.596 \times 10^6 \times 10^{0.360\theta} + 35.463$	$\mathrm{F_{Moon}} = 151.629 \times \mathrm{P}(\Phi)10^{0.015\Theta} - 26.084$
R	$\mathrm{F_{Sun}} = 2.158 \times 10^6 \times 10^{0.353\theta} + 75.622$	$\mathrm{F_{Moon}} = 232.785 \times \mathrm{P}(\Phi)10^{0.013\Theta} - 31.993$

Table 5.5. Sun elevation angles corresponding to increased sky brightness

Flux increase	B	V	R
20%	-17.2°	-15.0°	-14.7°
50%	-16.0°	-13.9°	-13.6°
100%	-15.1°	-13.1°	-12.7°
200%	-14.2°	-12.2°	-11.9°

twilight depends not only on the photometric band pass, but also the atmospheric conditions at the site. Fig. 5.13 shows the relationship between the Sun and the Moon elevation on the sky brightness. The flux from the Moon, however, becomes significant only very close to the time of moonrise. Table 5.5 roughly shows the quantitative effect of the Sun's elevation below the horizon on the sky brightness.

Fig. 5.14 shows the measured sky brightness in B, V, and R (the top panel). The middle panel shows our model of the solar and lunar contributions to the sky brightness. The bottom panel shows the observed sky brightness minus the contributions of the Sun and Moon from our model. The residuals are predictably flatter because we have subtracted off the contribution of the Moon when it is above the horizon. Theoretically, the contributions of the aurora and airglow can be estimated after properly removing the solar and lunar contributions to the sky background. However, there is still a significant fraction of scattered light that cannot be well modeled within the area of study 20° in diameter, especially when the Moon has a higher elevation angle. Hence, we do not provide any quantitative estimate of aurora and airglow in our inspecting area. During the 2009 observing season there were few large enhancements of the sky brightness when the Sun and Moon had low elevation angles. We have minimal evidence of aurorae in our data.

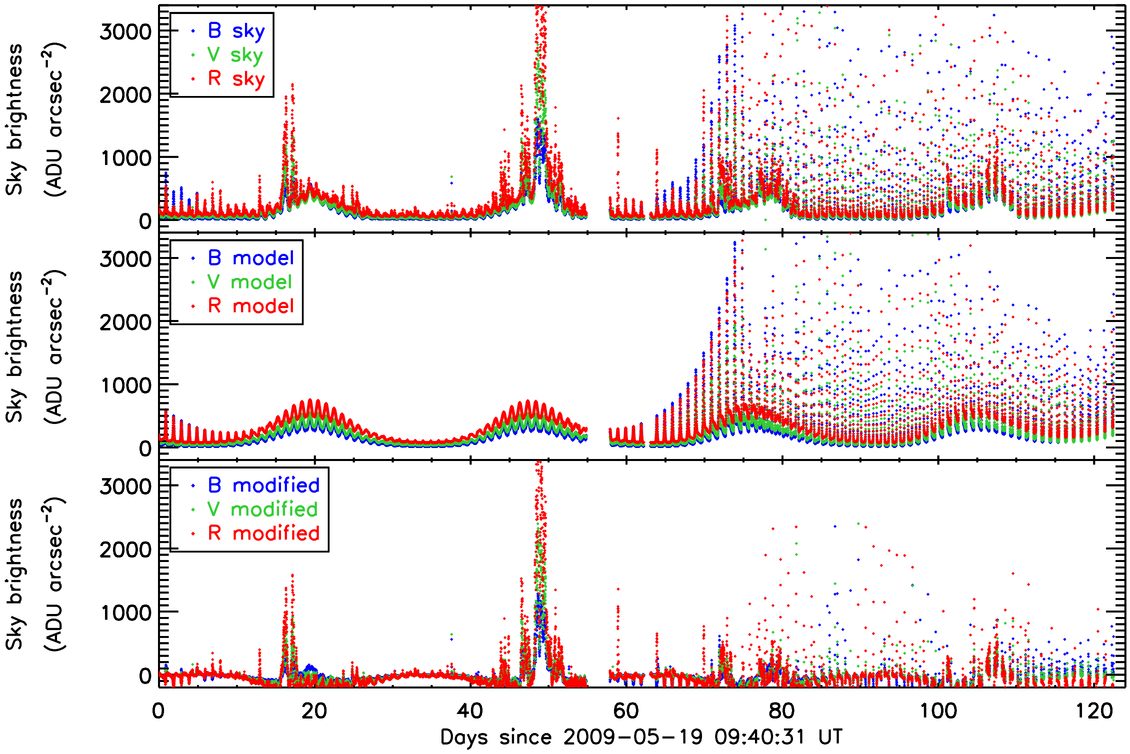

Figure 5.14 Application of the sky brightness models to correct the effects of the Sun and the Moon. Top panel: Measured sky brightness in ADU's per square arcsec. Middle panel: Our Sun and Moon model in the same units. Bottom panel: Data from the top panel minus the Sun and Moon model shown in the middle panel.

5.5.6 Extinction, transparency variations, and the estimation of cloud cover

The GASC FOV was centered near the SCP and extended to a zenith angle of 40°. The "air mass" X is the path length through the atmosphere at zenith angle z compared to the path length at the zenith, and X = sec(z). At z = 40°, X $\approx$ 1.3. At the far south latitude of Dome A any individual star within 40° of the zenith exhibits a small range of zenith angle over the course of the night. GASC observed many stars at any given time over a range of 0.3 air masses. Moreover, the measurement of atmospheric extinction with GASC data is made more complicated by vignetting, the angular response of the interline sensor, as well as the different paths of light transmission through the cover window.

Atmospheric extinction is expected to be small at Dome A. For reference, at the summit of Mauna Kea, Hawaii (which has a comparable elevation of 4205 m), the mean B- and V-band extinction values are 0.20 and 0.12 mag airmass^{-1}, respectively (Krisciunas et al., 1987). The R-band extinction would be lower, about 0.10 mag airmass^{-1}. Let Δ be the difference of the instrumental magnitudes and the catalog magnitudes of stars of known brightness. If the extinction at Dome A is comparable to that at Mauna Kea, over the GASC FOV we would expect Δ to exhibit a range vs. air mass of roughly 0.06 mag in the B-band, 0.04 mag in the V-band, and 0.03 mag in the R-band. No effect caused by the range of airmass has been detected with GASC data given its photometric accuracy, indicating a smaller atmospheric extinction coefficient at Dome A Antarctica compared to Mauna Kea.

We used the "pseudo-star" described in §5.4.4.2 as an indicator of the relative transparency variations to derive the likelihood of cloud cover at Dome A during the 2009 winter season. The reduction in transparency could be due to clouds, seasonal atmospheric variations, or even ice formed on the entrance transmission window. Some of those pairs of effects can hardly be separated, as they produce the same effect in the change of the

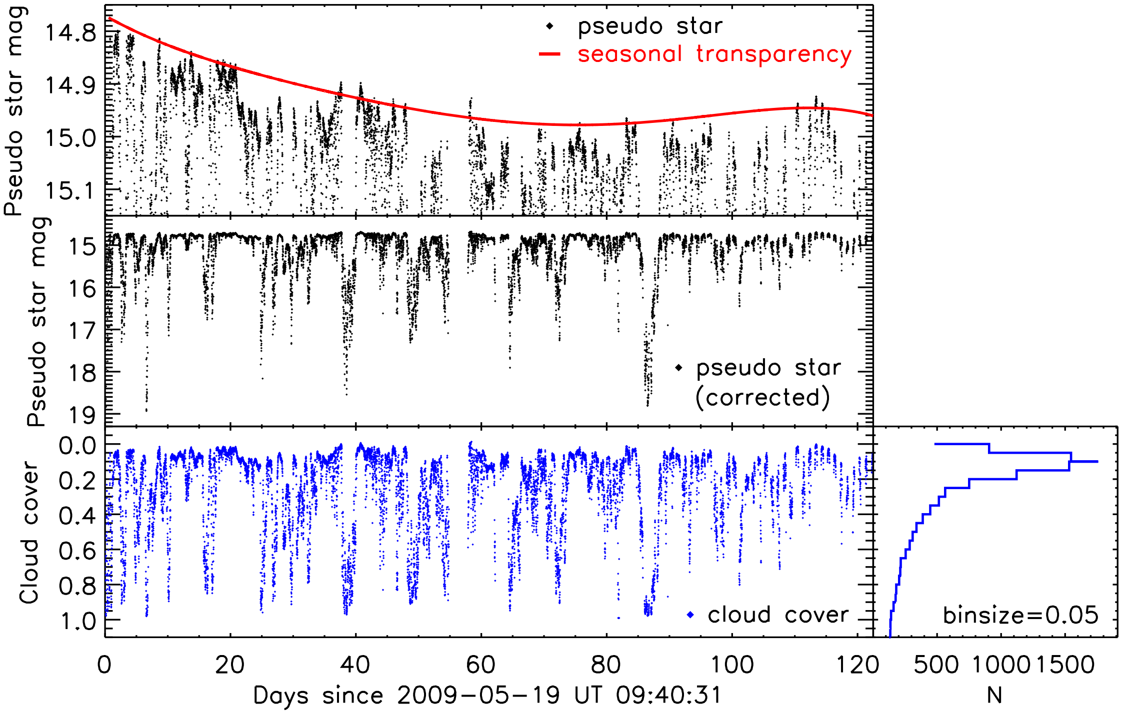

Figure 5.15 The atmospheric transparency estimated from the “pseudo-star” after correction of the long-term transparency variations. The black dots in the top panel are intentionally plotted with a small range of brightness of the pseudo-star. The red curve is a polynomial fit to the upper envelope and shows a long-term trend in the atmospheric transparency. The middle panel shows the variation of the “pseudo-star” after removing the seasonal transparency variation. The lower panel shows the time-series diagram of the implied cloud cover, with a histogram of the cloud cover data at the right. All magnitudes are uncalibrated instrumental magnitudes.

transparency. Therefore, our results represent the upper limits to the cloud cover. Fig. 5.15 shows the transparency and the estimated cloud cover during the 2009 winter season. A long-term variation in transparency inferred from the brightness of the "pseudo-star" is unlikely due to cloud coverage, but is more likely attributable to a seasonal variation of the atmosphere above Dome A. A fifth-order polynomial has been used to fit this long-term trend, and the residuals were used to calculate the upper limit of the cloud coverage. The estimation of the cloud coverage is also based on the "pseudo-star" after applying a correction to this long-term variation. The brightest values of the "pseudo-star" indicate very clear sky with cloud coverage estimated to be 0, and the reduction of the "pseudo star" magnitude, defined as Δm, was correlated with the cloud coverage as follows:

$$\Delta m = -2.5\log\frac{flux_1}{flux_2} = -2.5\log(1 - cloud\ cover)\ . \tag{5.10}$$

We find that the seasonal transparency degraded after June 2009, during which the Sun was furthest below the horizon for the year. This agrees with Zou et al. (2010) to some extent. However, the possibility that such a long-term transparency variation is due to a change in the condition of the instrument cannot be ruled out. Table 5.6 gives the cloud coverage percentages at Dome A from 19 May 2009 to 18 September 2009. A rough comparison of the cloud coverage at Mauna Kea is given in Table 5.7. This includes the cloud cover measured at the Gemini North Telescope and measurements with CSTAR in the I-band at Dome A during the 2008 winter season (Zou et al., 2010). CSTAR pointed at the SCP with a FOV of diameter $4.5°$ while the GASC FOV was $85°$. The results from 2008 and 2009 are comparable. At Dome A it is "cloudy" or worse 2% to 3.5% of the time, while at Mauna Kea this number is much higher, 30%. At Dome A there is less than 0.3 mag of extinction 62-67% of the time, while at Mauna Kea the sky is photometric only 50% of the time.

Table 5.6. Cloud cover at Dome A

Flux	Extinction (mag)	GASC2009	GASC2009[a]	Cstar2008	Description
$< 50\%$	> 0.75	17.2%	19.9%	9%	Thick
$50\% - 75\%$	$0.31 - 0.75$	19.4%	27.2%	17%	Intermediate
$75\% - 90\%$	$0.11 - 0.31$	29.1%	42.1%	23%	Thin
$> 90\%$	< 0.11	34.3%	10.8%	51%	Little or none

[a] Values obtained without correcting for the long-term transparency variation.

Table 5.7. Cloud cover compared to Mauna Kea

Description	Extinction (mag)	Mauna Kea	DomeA (GASC2009)	Dome A (GASC2009)[a]	Dome A (Cstar2008)
Any other usable	> 3	10%	1.0%	1.1%	0%
Cloudy	$2 - 3$	20%	2.5%	2.8%	2%
Patchy cloud	$0.3 - 2$	20%	34.2%	45.1%	31%
Photometric	< 0.3	50%	62.4%	51.0%	67%

[a] Values obtained without correcting for the long-term transparency variation.

A simple but effectively reliable way to check the cloud coverage estimated from the "pseudo-star" is to look at the original frames for certain fractions of cloud cover. Fig. 5.16 presents four sample images of cloud coverage of 0, 20, 70, and 95 percent obtained on 26 June 2009 at 01:16:22, 04:10:56, 18:23:18, and 20:54:41 UT. Many images estimated to have high cloud cover in GASC data did not show obvious cloudy patches. Instead, they showed a reduction in transparency over the entire FOV. It is hard to determine whether those extremely low transparency events were due to the sky or ice formation on the entrance window. However, we can look at the sky brightness and the transparency estimated by the pseudo-star to see whether the estimation of transparency has biased the sky background. Figure 5.17 shows the transparency-sky brightness diagram. The lower panel shows that the transparency is independent of the sky brightness in seasonal statistics, indicating our estimation of the cloud coverage based on the pseudo-star is not biased by the different sky background.

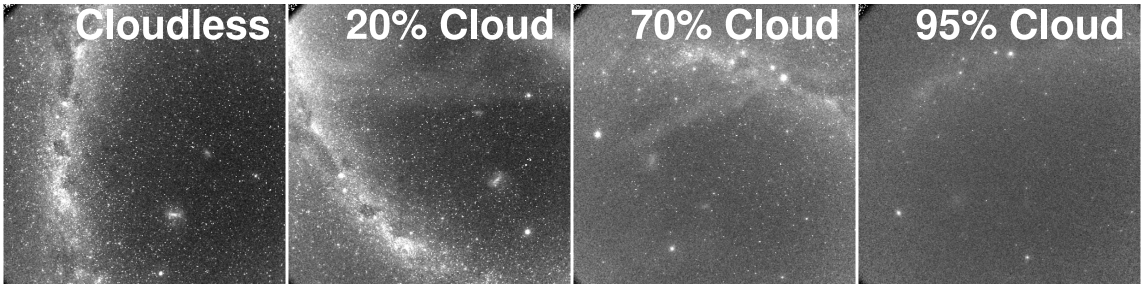

Figure 5.16 Four sample images showing cloudless sky, 20 percent cloud cover, 70 percent cloud cover and 95 percent cloud cover, from left to right, respectively.

5.5.7 Example light curves for bright stars

High-precision, high-cadence, time-series photometry serves as one of the major technical requirements for conducting asteroseismology. The search of exoplanets also benefits from high-quality photometric monitoring of stars. Stars within a magnitude range of $\sim$8 to $\sim$15 can be measured with $\sim$10 cm class and larger telescopes. However, uninterrupted monitoring of stars that are even brighter, i.e. magnitude 3 to 7, has not been feasible for previous Antarctic observations due to the very short time to reach the saturation level of a detector.

Our “ring correction” techinque allows us to obtain a dispersion level of $\sim$0.03 mag for stars around 5.5 mag in four consecutive days. This valuable long-term, multi-color, consecutive photometric dataset allows the study of eclipsing binaries, Cepheids, and other stellar variables. In Figure 5.18, we briefly present example light curves for a bright eclipsing binary ζ Phoenicis and a W Vir type Cepheid variable κ Pavonis with a short (4-day) and a long (120-day) period, respectively. More than 60 variables have been monitored by

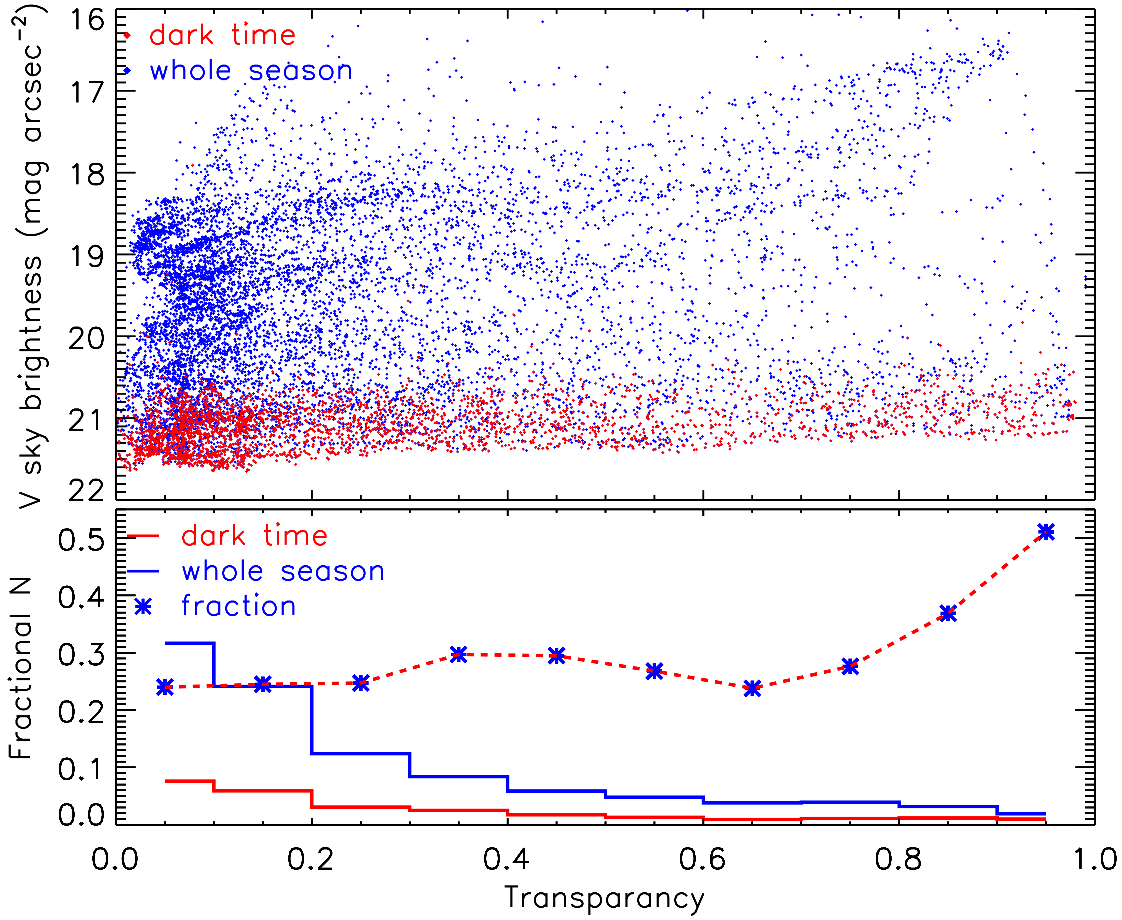

Figure 5.17 The V-band sky brightness derived from the median ADU's within a 20° circle centered at the SCP vs. the transparency (upper panel). The blue and red dots represent the sky brightness for the entire season and during the dark time, respectively. The lower panel shows the normalized histograms for the V-band sky brightness. The blue asterisks with red dashed lines show the ratio of the bin counts of the two histograms. The bottom panel shows that the transparency is independent of the sky brightness in seasonal statistics

the GASC in the B, V, and R bands. The multi-band photometric studies of these bright variables will be presented in another paper.

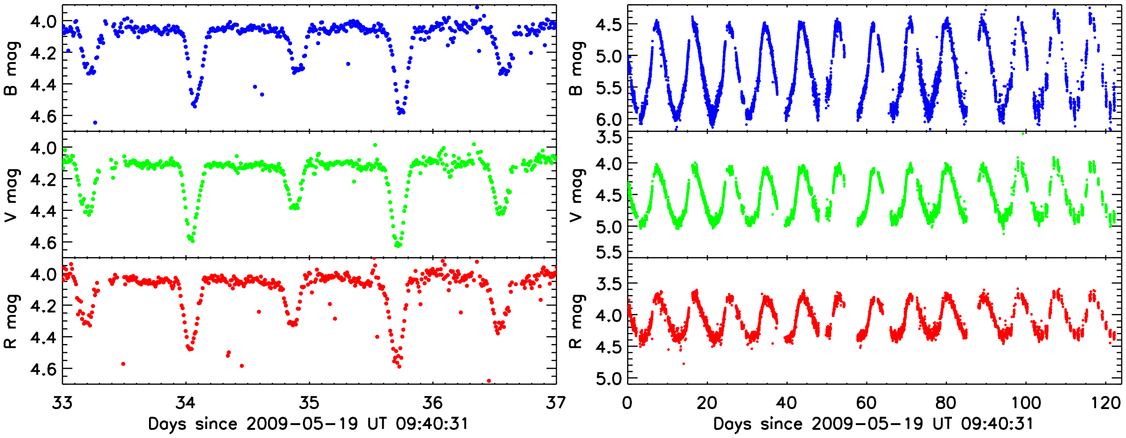

Figure 5.18 The B, V, and R band light curves for an eclipsing binary ζ Phoenicis (left panel) and a W Vir type Cepheid variable κ Pavonis (right panel).

5.6 Conclusions

In 2009 the Gattini-Dome A All-Sky Camera was deployed at Dome A in Antarctica to monitor the sky background, the variation of atmospheric transparency, and to perform photometry of bright targets in the field with an unprecedented window function. About 36,000 scientific images with 100 second exposure time, covering the Bessell B, V, and R photometric bands have been used to quantify the B-, V-, and R-band sky brightness, and to estimate the upper limit of cloud coverage. In a subsequent paper, we shall present photometry of more than 60 bright stars in our FOV that show significant variability based on GASC data after applying the method we developed to correct for the systematical error.

The median value of sky brightness when the Sun elevation is less than $-18°$ and the Moon is below the horizon is 22.45 mag arcsec^{-2} for B-band, 21.40 mag arcsec^{-2}

for the V-band, and 20.56 mag arcsec^{-2} for the R-band. If we consider a cumulative probability distribution, the darkest 10 percent of the time the B-, V-, and R-band sky brightness is 22.98, 21.86, and 21.68 mag arcsec^{-2}, respectively. These are comparable to the values obtained at solar minimum at other best astronomical sites such as Mauna Kea and the observatories in northern Chile. For future instruments operating at Dome A, customized filters or high spectral resolution designs could easily obtain better values on a more routine basis. A test carried out with GASC at Palomar Observatory indicated that the GASC "ring correction" method agrees with the Palomar NSBM within 0.12 mag arcsec^{-2}. At Dome A the sky brightness is quite constant within 30° of the SCP.

A "pseudo-star" was constructed based on all the stars over the FOV as an indicator of transparency variations. The cloud coverage during the 2009 winter season has been estimated. We found that the seasonal transparency worsened in June. The transparency changed considerably in June and July when the Sun was at its lowest below the horizon for the year. About 63% of the time there was little or thin cloud coverage, using the same criteria for the cloud coverage adopted at the Gemini North Observatory at Mauna Kea, and also the cloud coverage estimation from CSTAR (Zou et al., 2010).

Solar and lunar models for the flux contributions to the sky background have been fitted, and the different flux enhancements in the sky background for different bandpasses have been obtained. Aurora and airglow are hard to quantify with GASC observations due to limited photometric accuracy and unexpected instrumental effects. A visual inspection of the sky background after removing the solar and lunar contributions indicates a very limited effect of auroral events during the recent solar minimum.

Acknowledgments

We thank Shri Kulkarni and Caltech Optical Observatories, Gerard Van Belle and Chas Beichman for their financial contributions to this project. We are grateful to Xiaofeng Wang, Chao Wu, Ming Yang, Tianmeng Zhang, Yanping Zhang and Jilin Zhou for helpful discussions. The research is supported by the Chinese PANDA International Polar Year project and the Polar Research Institute of China. The project was funded by the following awards from the National Science Foundation Office of Polar Programs: ANT 0836571, ANT 0909664 and ANT 1043282. The project was also supported by the Strategic Priority Research Program "The Emergence of Cosmological Structures" of the Chinese Academy of Sciences, Grant No. XDB09000000. JNF acknowledges the support from the Joint Fund of Astronomy of National Natural Science Foundation of China (NSFC) and Chinese Academy of Sciences through the grant U1231202, the NSFC grant 11673003, the National Basic Research Program of China (973 Program 2014CB845700 and 2013CB834900), and the LAMOST FELLOWSHIP supported by Special Funding for Advanced Users, budgeted and administrated by Center for Astronomical Mega-Science, Chinese Academy of Sciences (CAMS). The operation of PLATO at Dome A is supported by the Australian Research Council, the Australian Antarctic Division, and the University of New South Wales. The authors wish to thank all the members of the 2008/2009/2010 PRIC Dome A heroic expeditions.

6. SUMMARY AND CONCLUSIONS

In this dissertation, we have presented a few work towards understanding the nature of the type Ia SN cosmology. The interstellar dust properties in the SN host galaxies, the circumstellar environment of type Ia SN, and the progenitor constrains on the SN explosion mechanism, together with the future opportunities to conduct large surveys at Antarctica have been discussed.

In Section 2, we present multiple-epoch measurements of the size and surface brightness of the light echoes from supernova (SN) 2014J in the nearby starburst galaxy M82. $Hubble\ Space\ Telescope\ (HST)$ ACS/WFC images were taken ~ 277 and ~ 416 days after B-band maximum in the filters F475W, F606W, and F775W. Observations reveal the temporal evolution of at least two major light-echo components. The first one exhibits a filled ring structure with position-angle-dependent intensity. This radially extended, diffuse echo indicates the presence of an inhomogeneous interstellar dust cloud ranging from $\sim$100 pc to $\sim$500 pc in the foreground of the SN. The second echo component appears as an unresolved luminous quarter-circle arc centered on the SN. The wavelength dependence of scattering measured in different dust components suggests that the dust producing the luminous arc favors smaller grain sizes, while that causing the diffuse light echo may have sizes similar to those of the Milky Way dust. Smaller grains can produce an optical depth consistent with that along the supernova-Earth line of sight measured by previous studies around maximum light. Therefore, it is possible that the dust slab, from which the luminous arc arises, is also responsible for most of the extinction towards SN 2014J. The optical depths determined from the Milky Way-like dust in the scattering matters are lower than that produced by the dust slab.

In Section 3, we presented linear polarimetry of SN 2014J in M82 using the *HST*

ACS/WFC in the filter bands $F475W$, $F606W$, and $F775W$, in five epochs from ~277 days to ~983 days after the B-band maximum. The polarization measured at day 277 shows conspicuous deviations from other epochs, and this deviation could be due to at least $\sim 10^{-6} M_{\odot}$ of dust located at a distance of $\sim 5 \times 10^{17}$ cm away from the SN. The scattering dust revealed by these observations seem to be aligned with the dust in the interstellar medium that is responsible for the large reddening towards the supernova. The presence of this circumstellar dust may set strong constraints on the progenitor system that led to the explosion of SN 2014J.

In Section 4, we measured and modelled the extremely late-time evolution of SN 2014J. The reprocessing of electrons and X-rays emitted by the radioactive decay chain ^{57}Co$\rightarrow$^{57}Fe are needed to explain the significant flattening of both the $F606W$-band and the pseudo-bolometric light curves. The flattening confirms previous predictions that the late-time evolution of type Ia sn luminosities requires additional energy input from the decay of ^{57}Co (Seitenzahl et al., 2009). By assuming the $F606W$-band luminosity scales with the bolometric luminosity at ~500 days after the $B-$band maximum light, a mass ratio ^{57}Ni/^{56}Ni$\sim$0.076$^{+0.009}_{-0.008}$ is required. This mass ratio is roughly ~3.5 times the solar ratio and favors a progenitor white dwarf with a mass near the Chandrasekhar limit. A similar fit using the constructed pseudo-bolometric luminosity gives a mass ratio ^{57}Ni/^{56}Ni$\sim$0.094$^{+0.017}_{-0.016}$. Astrometric tests based on the multi-epoch *HST* ACS/WFC images reveal no significant circumstellar light echoes in between 0.3 pc and 100 pc (Yang et al., 2017a) from the SN 2014J.

In Section 5, We present here the measurements of sky brightness with the Gattini ultra-large field of view ($90^{\circ} \times 90^{\circ}$) in the photometric B-, V-, and R-bands, cloud cover statistics measured during the 2009 winter season, and an estimate of the sky transparency. A cumulative probability distribution indicates that the darkest 10% of the nights at Dome A have sky brightness of S$_B$ = 22.98, S$_V$ = 21.86, and S$_R$ = 21.68 mag arcsec^{-2}. These values were obtained around the year 2009 with minimum aurora, and they are comparable to the faintest sky brightness at Mauna Kea and the best sites of northern Chile. Since every filter includes strong auroral lines that effectively contaminate the sky brightness measurements, for instruments working around the auroral lines, either with custom filters or with high spectral resolution instruments, these values could be easily obtained on a more routine basis. In addition, we present example light curves for bright targets to emphasize the unprecedented observational window function available from this ground-based site.

We will apply our methods presented in this dissertation to more type Ia SNe in the future. The expected scientific results include (1) A systematic and more universal characterization of the optical properties and associated size distributions and compositions of the interstellar dust in nearby extragalactic environments; (2) constraints on the circumstellar environment around a few nearby Type Ia SNe. We will compile our new understanding of the dust into the current method of extinction correction for SN cosmology. The constraints on the CSM will further help to explore the mysterious explosion physics of type Ia SNe.

REFERENCES

Agabi, A., Aristidi, E., Azouit, M., et al. 2006, PASP, 118, 344

Amanullah, R., & Goobar, A. 2011, ApJ, 735, 20

Amanullah, R., Goobar, A., Johansson, J., et al. 2014, ApJL, 788, L21

Andersson, B.-G., & Potter, S. B. 2010, ApJ, 720, 1045

Andersson, B.-G., Piirola, V., De Buizer, J., et al. 2013, ApJ, 775, 84

Aristidi, E., Fossat, E., Agabi, A., et al. 2009, A&A, 499, 955

Aristidi, E., Vernin, J., Fossat, E., et al. 2015, MNRAS, 454, 4304

Arnett, W. D. 1979, ApJL, 230, L37

—. 1982, ApJ, 253, 785

Ashley, M. C. B., Burton, M. G., Storey, J. W. V., et al. 1996, PASP, 108, 721

Asplund, M., Grevesse, N., Sauval, A. J., & Scott, P. 2009, ARAA, 47, 481

Avila, R. *et al.*. 2017, Baltimore: STScI, Version 16.0

Axelrod, T. S. 1980, PhD thesis, California Univ., Santa Cruz.

Baglin, A., Auvergne, M., Boisnard, L., et al. 2006, in COSPAR Meeting, Vol. 36, 36th COSPAR Scientific Assembly

Barbon, R., Ciatti, F., & Rosino, L. 1973, A&A, 25, 241

Benn, C. R., & Ellison, S. L. 1998, NewAR, 42, 503

Bessell, M. S. 1990, PASP, 102, 1181

Biretta, J., Kozhurina-Platais, V., Boffi, F., Sparks, W., & Walsh, J. 2004, ACS Polarization Calibration - I. Introduction and Status Report, Tech. rep.

Bloom, J. S., Kasen, D., Shen, K. J., et al. 2012, ApJL, 744, L17

Bohlin, R. C. 2012, Flux Calibration of the ACS CCD Cameras IV. Absolute Fluxes, Instrument Science Report ACS 2012-01, Tech. rep., Baltimore: STScI

Bonanos, A. Z., & Boumis, P. 2016, A&A, 585, A19

Bond, H. E., Gilmozzi, R., Meakes, M. G., & Panagia, N. 1990, ApJL, 354, L49

Bond, H. E., Henden, A., Levay, Z. G., et al. 2003, Nature, 422, 405

Bonner, C. S., Ashley, M. C. B., Cui, X., et al. 2010, PASP, 122, 1122

Borucki, W. J., Koch, D., Basri, G., et al. 2010, Science, 327, 977

Brown, P. J., Breeveld, A., Roming, P. W. A., & Siegel, M. 2016, AJ, 152, 102

Brown, P. J., Smitka, M. T., Wang, L., et al. 2015, ApJ, 805, 74

Bulla, M., Sim, S. A., Pakmor, R., et al. 2016, MNRAS, 455, 1060

Cao, Y., Kulkarni, S. R., Howell, D. A., et al. 2015, Nature, 521, 328

Cappellaro, E., Mazzali, P. A., Benetti, S., et al. 1997, A&A, 328, 203

Cappellaro, E., Patat, F., Mazzali, P. A., et al. 2001, ApJL, 549, L215

Cardelli, J. A., Clayton, G. C., & Mathis, J. S. 1989, ApJ, 345, 245

Chadid, M., Vernin, J., Mekarnia, D., et al. 2010, A&A, 516, L15

Chadid, M., Vernin, J., Preston, G., et al. 2014, AJ, 148, 88

Chadid, M., Vernin, J., Abe, L., et al. 2016, in PROCSPIE, Vol. 9908, Society of Photo-Optical Instrumentation Engineers (SPIE) Conference Series, 99080T

Chan, K.-W., & Lingenfelter, R. E. 1993, ApJ, 405, 614

Chevalier, R. A. 1986, ApJ, 308, 225

Churazov, E., Sunyaev, R., Isern, J., et al. 2014, Nature, 512, 406

Cikota, A., Deustua, S., & Marleau, F. 2016, ApJ, 819, 152

Cracraft, M., & Sparks, W. B. 2007, ACS Polarization Calibration - Data, Throughput, and Multidrizzle Weighting Schemes, Instrument Science Report ACS 2007-10, Tech. rep.

Crotts, A. P. S. 1988, ApJL, 333, L51

—. 2015, ApJL, 804, L37

Dalcanton, J. J., Williams, B. F., Seth, A. C., et al. 2009, ApJS, 183, 67

Davidson, K., & Humphreys, R. M. 2012, Nature, 486, E1

Denisenko, D., Gorbovskoy, E., Lipunov, V., et al. 2014, The Astronomer's Telegram, 5795

Diehl, R., Siegert, T., Hillebrandt, W., et al. 2015, A&A, 574, A72

Dimitriadis, G., Sullivan, M., Kerzendorf, W., et al. 2017, ArXiv e-prints, arXiv:1701.07267

Draine, B. T. 2003a, ARAA, 41, 241

—. 2003b, ApJ, 598, 1017

Draine, B. T., & Lee, H. M. 1984, ApJ, 285, 89

Drozdov, D., Leising, M. D., Milne, P. A., et al. 2015, ApJ, 805, 71

Elias, J. H., Frogel, J. A., Hackwell, J. A., & Persson, S. E. 1981, ApJL, 251, L13

Fitzpatrick, E. L. 1999, PASP, 111, 63

Foley, R. J., Fox, O. D., McCully, C., et al. 2014, MNRAS, 443, 2887

Fossey, J., Cooke, B., Pollack, G., Wilde, M., & Wright, T. 2014, Central Bureau Electronic Telegrams, 3792, 1

Fransson, C., Houck, J., & Kozma, C. 1996, in IAU Colloq. 145: Supernovae and Supernova Remnants, ed. T. S. Kuhn, 211

Fransson, C., & Jerkstrand, A. 2015, ApJL, 814, L2

Gallagher, III, J. S., & Smith, L. J. 1999, MNRaS, 304, 540

Gao, J., Jiang, B. W., Li, A., Li, J., & Wang, X. 2015, ApJL, 807, L26

Garstang, R. H. 1991, PASP, 103, 1109

Gattinger, R. L., & Jones, A. V. 1974, Canadian Journal of Physics, 52, 2343

Gehrels, N., Chincarini, G., Giommi, P., et al. 2004, ApJ, 611, 1005

Gerke, J. R., Kochanek, C. S., & Stanek, K. Z. 2014, The Astronomer's Telegram, 5808

Giordano, C., Vernin, J., Chadid, M., et al. 2012, PASP, 124, 494

Gold, T. 1952, MNRAS, 112, 215

Gonzaga, S., Hack, W., Fruchter, A., & Mack, J. 2012, The DrizzlePac Handbook (Baltimore: STScI)

Goobar, A. 2008, ApJL, 686, L103

Goobar, A., Johansson, J., Amanullah, R., et al. 2014, ApJL, 784, L12

Goobar, A., Kromer, M., Siverd, R., et al. 2015, ApJ, 799, 106

Graham, M. L., Nugent, P. E., Sullivan, M., et al. 2015a, MNRAS, 454, 1948

Graham, M. L., Valenti, S., Fulton, B. J., et al. 2015b, ApJ, 801, 136

Graur, O., Zurek, D., Shara, M. M., et al. 2016, ApJ, 819, 31

Grefenstette, B. W., Harrison, F. A., Boggs, S. E., et al. 2014, Nature, 506, 339

Hartig, G. F. 2009, WFC3 SMOV Programs 11436/8: UVIS On-orbit PSF Evaluation, Instrument Science Report WFC3 2009-38, Tech. rep., Baltimore: STScI

Havlen, R. J. 1972, A&A, 16, 252

Henyey, L. G., & Greenstein, J. L. 1941, ApJ, 93, 70

Hoang, T. 2017, ApJ, 836, 13

Hoang, T., Lazarian, A., & Schlickeiser, R. 2015, ApJ, 806, 255

Hoyle, F., & Fowler, W. A. 1960, ApJ, 132, 565

Huang, Z., Fu, J., Zong, W., et al. 2015, AJ, 149, 25

Hutton, S., Ferreras, I., & Yershov, V. 2015, MNRAS, 452, 1412

Iben, Jr., I., & Tutukov, A. V. 1984, ApJs, 54, 335

Itagaki, K., Kaneda, H., Yamaoka, H., et al. 2014, Central Bureau Electronic Telegrams, 3792

Iwamoto, K., Brachwitz, F., Nomoto, K., et al. 1999, ApJS, 125, 439

Jack, D., Mittag, M., Schröder, K.-P., et al. 2015, MNRAS, 451, 4104

Johansson, J., Goobar, A., Kasliwal, M. M., et al. 2017, MNRAS, 466, 3442

Jones, A. V., & Gattinger, R. L. 1975, Canadian Journal of Physics, 53, 1806

Jones, D. O., Rodney, S. A., Riess, A. G., et al. 2013, ApJ, 768, 166

Kapteyn, J. C. 1901, Astronomische Nachrichten, 157, 201

Kasen, D. 2010, ApJ, 708, 1025

Kawabata, K. S., Nagae, O., Chiyonobu, S., et al. 2008, in Society of Photo-Optical Instrumentation Engineers (SPIE) Conference Series, Vol. 7014, Society of Photo-Optical Instrumentation Engineers (SPIE) Conference Series, 4

Kawabata, K. S., Akitaya, H., Yamanaka, M., et al. 2014, ApJL, 795, L4

Kenyon, S. L., & Storey, J. W. V. 2006, PASP, 118, 489

Kerzendorf, W. E., Taubenberger, S., Seitenzahl, I. R., & Ruiter, A. J. 2014, ApJL, 796, L26

Khokhlov, A. M. 1991, A&A, 245, 114

Krisciunas, K. 1997, PASP, 109, 1181

Krisciunas, K., Bogglio, H., Sanhueza, P., & Smith, M. G. 2010, PASP, 122, 373

Krisciunas, K., & Schaefer, B. E. 1991, PASP, 103, 1033

Krisciunas, K., Semler, D. R., Richards, J., et al. 2007, PASP, 119, 687

Krisciunas, K., Sinton, W., Tholen, K., et al. 1987, PASP, 99, 887

Krist, J. 1993, in Astronomical Society of the Pacific Conference Series, Vol. 52, Astronomical Data Analysis Software and Systems II, ed. R. J. Hanisch, R. J. V. Brissenden, & J. Barnes, 536

Krist, J., & Hook, R. 2008, Tiny Tim Users Manual v6.2, http://www.stsci.edu/software/tinytim/

Lair, J. C., Leising, M. D., Milne, P. A., & Williams, G. G. 2006, AJ, 132, 2024

Landolt, A. U. 1992, AJ, 104, 340

Laor, A., & Draine, B. T. 1993, ApJ, 402, 441

Lawrence, J. S. 2004, PASP, 116, 482

Lawrence, J. S., Ashley, M. C. B., Tokovinin, A., & Travouillon, T. 2004, Nature, 431, 278

Lazarian, A., & Hoang, T. 2007, MNRAS, 378, 910

Leloudas, G., Stritzinger, M. D., Sollerman, J., et al. 2009, A&A, 505, 265

Li, G., Fu, J., & Liu, X. 2015, ArXiv e-prints, arXiv:1510.06134

Liang, E.-S., Wang, S., Zhou, J.-L., et al. 2016, ArXiv e-prints, arXiv:1608.07904

Liu, J.-F., Bregman, J. N., & Seitzer, P. 2003a, ApJ, 582, 919

Liu, Y., Zhou, X., Sun, W.-H., et al. 2003b, PASP, 115, 495

Lucas, R. 2016, ACS Data Handbook, Version 8.0 (Baltimore: STScI)

Lundqvist, P., Nyholm, A., Taddia, F., et al. 2015, A&A, 577, A39

Ma, B., Wei, P., Shang, Z., Wang, L., & Wang, X. 2014, The Astronomer's Telegram, 5794

Mandel, K. S., Narayan, G., & Kirshner, R. P. 2011, ApJ, 731, 120

Margutti, R., Parrent, J., Kamble, A., et al. 2014, ApJ, 790, 52

Marks, R. D. 2002, A&A, 385, 328

Marks, R. D., Vernin, J., Azouit, M., et al. 1996, A&AS, 118, 385

Mattsson, L. 2016, ArXiv e-prints, arXiv:1606.02272

Maund, J. R., & Smartt, S. J. 2005, MNRaS, 360, 288

Maund, J. R., Spyromilio, J., Höflich, P. A., et al. 2013, MNRaS, 433, L20

McCully, C., Jha, S. W., Foley, R. J., et al. 2014, ApJ, 786, 134

McKenna, D. 2008, http://www.sao.arizona.edu/FLWO/SBM/SBMreport_McKenna_Apr08.pdf

Meikle, W. P. S., Mattila, S., Gerardy, C. L., et al. 2006, ApJ, 649, 332

Meng, Z., Zhou, X., Zhang, H., et al. 2013, PASP, 125, 1015

Mie, G. 1976, Contributions to the optics of turbid media, particularly of colloidal metal solutions, Tech. rep.

Milne, P. A., The, L.-S., & Leising, M. D. 1999, ApJS, 124, 503

—. 2001, ApJ, 559, 1019

Montier, L., Plaszczynski, S., Levrier, F., et al. 2015, A&A, 574, A135

Moore, A., Allen, G., Aristidi, E., et al. 2008, in PROCSPIE, Vol. 7012, Ground-based and Airborne Telescopes II, 701226

Nguyen, H. T., Rauscher, B. J., Severson, S. A., et al. 1996, PASP, 108, 718

Nobili, S., & Goobar, A. 2008, A&A, 487, 19

Oelkers, R. J., Macri, L. M., Wang, L., et al. 2015, AJ, 149, 50

Ohlmann, S. T., Kromer, M., Fink, M., et al. 2014, A&A, 572, A57

Olling, R. P., Mushotzky, R., Shaya, E. J., et al. 2015, Nature, 521, 332

Otsuka, M., Meixner, M., Panagia, N., et al. 2012, ApJ, 744, 26

Pakmor, R., Hachinger, S., Röpke, F. K., & Hillebrandt, W. 2011, A&A, 528, A117

Pakmor, R., Kromer, M., Taubenberger, S., et al. 2012, ApJL, 747, L10

Patat, F. 2003, A&A, 400, 1183

—. 2005, MNRAS, 357, 1161

Patat, F., Benetti, S., Cappellaro, E., & Turatto, M. 2006, MNRAS, 369, 1949

Patat, F., & Taubenberger, S. 2011, A&A, 529, A57

Patat, F., Chandra, P., Chevalier, R., et al. 2007, Science, 317, 924

Patat, F., Taubenberger, S., Cox, N. L. J., et al. 2015, A&A, 577, A53

Penney, R., & Hoeflich, P. 2014, ApJ, 795, 84

Perlmutter, S., Aldering, G., Goldhaber, G., et al. 1999, ApJ, 517, 565

Phillips, M. M. 1993, ApJL, 413, L105

Phillips, M. M., Lira, P., Suntzeff, N. B., et al. 1999, AJ, 118, 1766

Porter, A. L., Leising, M. D., Williams, G. G., et al. 2016, ApJ, 828, 24

Quinn, J. L., Garnavich, P. M., Li, W., et al. 2006, ApJ, 652, 512

Rau, A., Kulkarni, S. R., Law, N. M., et al. 2009, PASP, 121, 1334

Rayleigh, L. 1928, Proceedings of the Royal Society of London Series A, 119, 11

Rayleigh, L., & Jones, H. S. 1935, Proceedings of the Royal Society of London Series A, 151, 22

Rest, A., Matheson, T., Blondin, S., et al. 2008, ApJ, 680, 1137

Rest, A., Prieto, J. L., Walborn, N. R., et al. 2012, Nature, 482, 375

Riess, A. G., Press, W. H., & Kirshner, R. P. 1996, ApJ, 473, 588

Riess, A. G., Filippenko, A. V., Challis, P., et al. 1998, AJ, 116, 1009

Riess, A. G., Macri, L. M., Hoffmann, S. L., et al. 2016, ApJ, 826, 56

Rimoldi, A., Portegies Zwart, S., & Rossi, E. M. 2016, Computational Astrophysics and Cosmology, 3, 2

Ritchey, G. W. 1901, ApJ, 14, 293

Roach, F. E., & Gordon, J. L. 1973, The light of the night sky.

Roming, P. W. A., Kennedy, T. E., Mason, K. O., et al. 2005, Space Science Reviews, 120, 95

Röpke, F. K., Kromer, M., Seitenzahl, I. R., et al. 2012, ApJL, 750, L19

Sand, D. J., Hsiao, E. Y., Banerjee, D. P. K., et al. 2016, ApJL, 822, L16

Saunders, W., Lawrence, J. S., Storey, J. W. V., et al. 2009, PASP, 121, 976

Schlafly, E. F., & Finkbeiner, D. P. 2011, ApJ, 737, 103

Schmidt, B. P., Kirshner, R. P., Leibundgut, B., et al. 1994, ApJL, 434, L19

Seitenzahl, I. R., Taubenberger, S., & Sim, S. A. 2009, MNRaS, 400, 531

Seitenzahl, I. R., Timmes, F. X., & Magkotsios, G. 2014, ApJ, 792, 10

Seitenzahl, I. R., Ciaraldi-Schoolmann, F., Röpke, F. K., et al. 2013, MNRAS, 429, 1156

Serkowski, K. 1958, actaa, 8, 135

Serkowski, K. 1962, Advances in Astronomy and Astrophysics, 1, 289

Serkowski, K., Mathewson, D. S., & Ford, V. L. 1975, ApJ, 196, 261

Shappee, B. J., Stanek, K. Z., Kochanek, C. S., & Garnavich, P. M. 2016, ArXiv e-prints, arXiv:1608.01155

Sims, G., Ashley, M. C. B., Cui, X., et al. 2010, in PROCSPIE, Vol. 7733, Ground-based and Airborne Telescopes III, 77334M

Sims, G., Ashley, M. C. B., Cui, X., et al. 2012a, PASP, 124, 637

—. 2012b, PASP, 124, 74

Sinnott, B., Welch, D. L., Rest, A., Sutherland, P. G., & Bergmann, M. 2013, ApJ, 767, 45

Sirianni, M., Jee, M. J., Benítez, N., et al. 2005, PASP, 117, 1049

Sollerman, J., Lindahl, J., Kozma, C., et al. 2004, A&A, 428, 555

Sparks, W. B. 1994, ApJ, 433, 19

Sparks, W. B., & Axon, D. J. 1999, PASP, 111, 1298

Sparks, W. B., Macchetto, F., Panagia, N., et al. 1999, ApJ, 523, 585

Sparks, W. B., Bond, H. E., Cracraft, M., et al. 2008, AJ, 135, 605

Spyromilio, J., Malin, D. F., Allen, D. A., Steer, C. J., & Couch, W. J. 1995, MNRaS, 274, 256

Srivastav, S., Ninan, J. P., Kumar, B., et al. 2016, MNRAS, 457, 1000

Stritzinger, M., & Sollerman, J. 2007, A&A, 470, L1

Sugerman, B., & Lawrence, S. 2016, The Astronomer’s Telegram, 8890

Sugerman, B. E. K. 2003, AJ, 126, 1939

—. 2005, ApJL, 632, L17

Sugerman, B. E. K., & Crotts, A. P. S. 2002, ApJL, 581, L97

Suntzeff, N. B., Heathcote, S., Weller, W. G., Caldwell, N., & Huchra, J. P. 1988, Nature, 334, 135

Swartz, D. A., & Wheeler, J. C. 1991, ApJL, 379, L13

Swope, H. H. 1940, Harvard College Observatory Bulletin, 913, 11

Taubenberger, S., Elias-Rosa, N., Kerzendorf, W. E., et al. 2015, MNRAS, 448, L48

Truran, J. W., Arnett, W. D., & Cameron, A. G. W. 1967, Canadian Journal of Physics, 45, 2315

Tsebrenko, D., & Soker, N. 2015, MNRaS, 450, 1399

Tylenda, R. 2004, A&A, 414, 223

van de Hulst, H. C. 1957, Light scattering by small particles (Wiley:âĂŁ New York)

Van Dyk, S. D. 2013, AJ, 146, 24

Van Dyk, S. D., Li, W., & Filippenko, A. V. 2006, PASP, 118, 351

Van Dyk, S. D., Lee, J. C., Anderson, J., et al. 2015, ApJ, 806, 195

Vernin, J., Chadid, M., Aristidi, E., et al. 2009, A&A, 500, 1271

Vogt, F. P. A., Besel, M.-A., Krause, O., & Dullemond, C. P. 2012, ApJ, 750, 155

Voshchinnikov, N. V., Henning, T., Prokopjeva, M. S., & Das, H. K. 2012, A&A, 541, A52

Walker, M. F. 1988, PASP, 100, 496

Wang, L. 2005, ApJL, 635, L33

Wang, L., Baade, D., Höflich, P., et al. 2004, ApJL, 604, L53

Wang, L., & Wheeler, J. C. 1996, ApJL, 462, L27

—. 2008, ARAA, 46, 433

Wang, L., Macri, L. M., Krisciunas, K., et al. 2011, AJ, 142, 155

Wang, L., Macri, L. M., Wang, L., et al. 2013, AJ, 146, 139

Wang, S., Zhou, X., Zhang, H., et al. 2012, PASP, 124, 1167

Wang, S., Zhang, H., Zhou, J.-L., et al. 2014a, ApJS, 211, 26

Wang, S., Zhang, H., Zhou, X., et al. 2015, ApJS, 218, 20

Wang, S.-H., Zhou, X., Zhang, H., et al. 2014b, Research in Astronomy and Astrophysics, 14, 345

Wang, X., Li, W., Filippenko, A. V., et al. 2008, ApJ, 677, 1060

Webbink, R. F. 1984, ApJ, 277, 355

Weingartner, J. C., & Draine, B. T. 2001, ApJ, 548, 296

Welch, D. L., Clayton, G. C., Campbell, A., et al. 2007, ApJ, 669, 525

Whittet, D. C. B., Martin, P. G., Hough, J. H., et al. 1992, ApJ, 386, 562

Wood, K., Bjorkman, J. E., Whitney, B. A., & Code, A. D. 1996, ApJ, 461, 828

Woosley, S. E., Arnett, W. D., & Clayton, D. D. 1973, ApJS, 26, 231

Xu, J., Crotts, A. P. S., & Kunkel, W. E. 1994, ApJ, 435, 274

Yang, H., Allen, G., Ashley, M. C. B., et al. 2009, PASP, 121, 174

Yang, H., Kulesa, C. A., Walker, C. K., et al. 2010, PASP, 122, 490

Yang, M., Zhang, H., Wang, S., et al. 2015, ApJS, 217, 28

Yang, Y., Moore, A. M., Krisciunas, K., et al. 2016, ArXiv e-prints, arXiv:1610.10094

Yang, Y., Wang, L., Baade, D., et al. 2017a, ApJ, 834, 60

—. 2017b, ArXiv e-prints, arXiv:1704.01431

Yuan, X., Cui, X., Liu, G., et al. 2008, in PROCSPIE, Vol. 7012, Ground-based and Airborne Telescopes II, 70124G

Yuan, X., Cui, X., Gu, B., et al. 2014, in PROCSPIE, Vol. 9145, Ground-based and Airborne Telescopes V, 91450F

Zheng, W., Shivvers, I., Filippenko, A. V., et al. 2014, ApJL, 783, L24

Zong, W., Fu, J.-N., Niu, J.-S., et al. 2015, AJ, 149, 84

Zou, H., Zhou, X., Jiang, Z., et al. 2010, AJ, 140, 602